

Continuous Production of Stable Polymeric Nanoparticles for Oral Drug Delivery

BY

HAO SHEN

B.S., South China University of Technology, 2008

THESIS

Submitted as partial fulfillment of the requirements
for the degree of Doctor of Philosophy in Chemical Engineering
in the Graduate College of the
University of Illinois at Chicago, 2013

Chicago, Illinois

Defense Committee:

Ying Liu, Chair and Advisor

Sohail Murad

Lewis E. Wedgewood

Seungpyo Hong, Department of Biopharmaceutical Sciences

Ursula Perez-Salas, Department of Physics

ACKNOWLEDGEMENTS

I would like to thank my advisor, Dr. Ying Liu. Her critical insights and enthusiastic support encouraged me from the first day of my study. Her ability as a mentor is only exceeded by her broad scientific knowledge, which is second to none. It is my life fortune to receive her guidance. What I have learned from her will certainly benefit my future career.

I would like to thank my thesis committee, Dr. Ying Liu, Dr. Sohail Murad, Dr. Lewis E. Wedgewood, Dr. Seungpyo Hong and Dr. Ursula Perez-Salas for their unwavering support and assistance. Their support and guidance in all areas helped me accomplish my research goals.

I would like to thank our collaborates, Dr. Seungpyo Hong's group, Dr. Zaijie (Jim) Wang's group, Dr. Hayat Onyuksel's group and Dr. Richard A. Gemeinhart's group at Department of Biopharmaceutical Sciences, UIC, Dr. Ursula Perez-Salas's group at Department of Physics, UIC, Dr. Alexander V Lyubimov's group at Toxicology Research Laboratory, UIC, and Dr. Yoon Yeo's group at Department of Industrial and Physical Pharmacy, Purdue University. Their help and support are extremely important for me.

I would like to thank my labmates, Vishal Sharma, Magdalena Szymusiak, Alexander Donovan, Yuan Zhang, Ross Ransom, Francine Feumba, Marzena Zarycki and Paulina Mlynarska for their support every day. The time that we spent together will stay in my memory forever.

Last, I would like to thank my family, especially my parents Guomei Sun, Huilin Shen and my wife Lisha Yao. Their love and belief are the best fortune I had in my life.

The funding comes from National Cancer Institute, Department of Health and Human Services (contract number N01-CN-43306) and Department of Defense (contract number WQ81XWH-11-2-0021).

Hao Shen

TABLE OF CONTENTS

ACKNOWLEDGEMENTS	I
TABLE OF CONTENTS	II
LIST OF TABLES	V
LIST OF FIGURES	VI
LIST OF ABBREVIATIONS	IX
SUMMARY	XI
CHAPTER 1. INTRODUCTION	1
1.1 Current challenges in nano-medicine and our approach	1
1.2 Current nano- and micro-particle drug-delivery systems.....	4
1.2.1 Lipid and surfactant based drug delivery systems	4
1.2.2 Liposomes	8
1.2.3 Dendrimers	10
1.2.4 Polymeric micelles	12
CHAPTER 2. SELF-ASSEMBLING PROCESS OF FLASH NANOPRECIPITATION IN A MULTI-INLET VORTEX MIXER (MIVM) TO PRODUCE DRUG-LOADED POLYMERIC NANOPARTICLES	18
2.1 Introduction.....	18
2.2 Experimental section.....	19
2.2.1 Materials	19
2.2.2 Mixing and flow pattern visualization.....	20
2.2.3 Nanoparticle preparation and characterization	21
2.2.4 CMC measurements	23
2.3 Nanoparticle size and size distribution	25
2.3.1 Effect of flow field and Reynolds number: Starting the competitive kinetics simultaneously	25
2.3.2 Effects of supersaturation rate and nature of polymers.....	31
2.3.3 Effect of drug loading rates	35
2.4 Nanoparticle drug loading.....	36
2.5 Conclusions.....	40
CHAPTER 3. FLASH NANOPRECIPITATION INTEGRATED WITH SPRAY DRYING- DEVELOPMENT OF CONTINUOUS AND SCALABLE PROCESS	43
3.1 Introduction.....	43
3.2 Experimental section.....	46
3.2.1 Materials	46
3.2.2 Nanoparticle preparation and characterization	46

3.2.3 Freeze drying and spray drying of the nanoparticle suspensions.....	47
3.2.4 Measurements of particle growth kinetics	48
3.3 Results and discussion	48
3.3.1 Stability of Nano-suspensions	48
3.3.2 Reproduction of freeze-dried nanoparticles.....	53
3.3.3 Reproduction of spray-dried nanoparticles	55
3.4 Conclusions.....	59
CHAPTER 4. ENHANCED ORAL BIOAVAILABILITY OF A CANCER PREVENTIVE AGENT (SR13668) BY EMPLOYING POLYMERIC NANOPARTICLES WITH HIGH DRUG LOADING.....	61
4.1 Introduction.....	61
4.2 Experimental	64
4.2.1 Materials	64
4.2.2 Nanoparticle preparation and size characterization	64
4.2.3 Spray drying of the nanoparticle suspensions	64
4.2.4 In vitro release of SR13668 from PLGA–SR13668 nanoparticle suspensions	65
4.2.5 In vivo release and systemic levels of SR13668 in mice	66
4.2.6 Dog dosing and clinical observations.....	67
4.2.7 In vivo release and systemic levels of SR13668 in dog.....	68
4.2.8 Pharmacokinetic evaluation	69
4.3 Results and discussion	70
4.3.1 Particle fabrication and resuspension	70
4.3.2 In vitro release	71
4.3.3 Pharmacokinetics and bioavailability study in mice	72
4.3.4 Pharmacokinetics and bioavailability study in beagle dogs.....	73
4.4 Conclusions.....	77
CHAPTER 5. ORALLY ADMINISTERED NANO-CURCUMIN TO ATTENUATE MORPHINE TOLERANCE AND DEPENDENCE: COMPARISON BETWEEN NEGATIVELY CHARGED AND PEGYLATED NANOPARTICLES	79
5.1 Introduction.....	79
5.2 Experimental section.....	81
5.2.1 Materials	81
5.2.2 Preparation and size characterization of nanoparticle suspensions	81
5.2.3 Spray drying of the nanoparticle suspensions	82
5.2.4 Measurements of curcumin in vitro release from the nanoparticles.....	82
5.2.5 Animals	83
5.2.6 Tests for antinociception.....	83

5.2.7 <i>Acute opioid tolerance and dependence</i>	84
5.3 Results and discussion	84
5.3.1 <i>Size distribution, drug loading, and encapsulation efficiency of the nanoparticles</i>	84
5.3.2 <i>In vitro release of curcumin</i>	88
5.3.3 <i>Effects of curcumin and curcumin nanoparticles on attenuating morphine tolerance and dependence</i>	89
5.4 Conclusion	93
CHAPTER 6. CONCLUSIONS	95
REFERENCES	98
VITA	106

LIST OF TABLES

Table 1-1. The Lipid Formulations Classification System proposed by Pouton. ²³	7
Table 3-1. Re-suspension of nanoparticles in Millipore water after being freeze dried with various amounts of leucine. The nanoparticles were PEG- <i>b</i> -PCL (MW 5000- <i>b</i> -6000) encapsulating SR13668 at a polymer-to-drug ratio of 5:1 wt/wt.....	54
Table 3-2. Re-suspension of the nanoparticles in Millipore water after being freeze dried with sucrose and trehalose. The nanoparticles were PEG- <i>b</i> -PCL (MW 5000- <i>b</i> -6000) encapsulating SR13668 at a ratio of 5:1 wt/wt.	55
Table 3-3. The sizes of the resuspended nanoparticles (PLGA (MW 7000-17000) encapsulating SR13668 at ratio of 2:1) depend on the type and amount of excipients.	56
Table 3-4. The sizes of the re-suspended nanoparticles (PLGA (MW 7000-17000) encapsulating SR13668 at ratio of 2:1) depend on the inlet temperature of the spray drier. 300 times trehalose and 5 times leucine were added as excipients. 60% ethanol was also added to the inlet stream.....	58
Table 4-1. Summary of pharmacokinetic parameters in dog plasma (mean \pm standard deviation)	75
Table 4-2. Summary of pharmacokinetic parameters in dog whole blood (mean \pm standard deviation)	75
Table 5-1. Average particle diameter (before and after spray dry), drug loading, encapsulation efficiency of the three curcumin nanoformulations.	86

LIST OF FIGURES

Figure 1-1. The steps of the continuous and scalable process. Nanoparticles encapsulating SR13668 were generated by using the MIVM, followed by nanoparticle characterization, freeze/spray drying, and re-suspension.	3
Figure 1-2. Schematic drawing of different drug delivery systems.	4
Figure 2-1. Molecular structure of the polymers and the drugs.	19
Figure 2-2. Reaction scheme of iron nitrate and potassium thiocyanate.	20
Figure 2-3. Design of a multi-inlet vortex mixer (MIVM) and images of mixing and flow patterns in the MIVM. (A) Photo of the MIVM. (B) Diagram of the reaction center of the MIVM with four tangential inlet streams for flow-pattern visualization. (C) Microphotographs of mixing and flow patterns in the MIVM. Imaging area was indicated by dashed circle in (B). Mixing of $\text{Fe}(\text{NO}_3)_3$ and KSCN generated red precipitation of $\text{Fe}(\text{SCN})_x^{(3-x)+}$ ($x \sim 3$) complexes. Mixing patterns depended on Reynolds number (Re). Clockwise from the upper left image in (C), Re was increased. (Upper left: $Re=267$. Upper right: $Re=537$. Lower left: $Re=806$. Lower right: $Re=1343$).	27
Figure 2-4. The dependence of nanoparticle size on Re , and supersaturation rate. (A) Sizes of PEO- <i>b</i> -PS nanoparticles encapsulating β -carotene. (B) Sizes of PEG- <i>b</i> -PCL nanoparticles encapsulating β -carotene. (C) Size distributions of PEG- <i>b</i> -PCL micelles and nanoparticles encapsulating β -carotene. The solid diamonds for the first curve in (C) indicate the size distribution of PEG- <i>b</i> -PCL micelles. The remaining six curves show the size distributions of PEG- <i>b</i> -PCL nanoparticles encapsulating β -carotene, which correspond to the six conditions circled in (B) with the same symbol shapes. Hollow symbols in (C) denote that particles were generated at $Re=6000$, while solid symbols denote that particles were generated at $Re=500$. (D) The TEM image of β -carotene nanoparticles encapsulated in PEG- <i>b</i> -PCL generated at $Re=6000$. The scale bar represents 20nm. (E) The TEM image of β -carotene particles generated from direct precipitation without polymer protection. The scale bar represents 2 μm	29
Figure 2-5. Sizes of PEI and PEI/PEG- <i>b</i> -PAA complexes. (A) Sizes of the PEI/PEG- <i>b</i> -PAA complexes versus Re . (B) Size distributions of PEI and PEI/PEG- <i>b</i> -PAA complexes. - \bullet - PEI, - \square - PEI/PEG- <i>b</i> -PAA complexes produced at $Re=500$, and - \blacksquare - PEI/PEG- <i>b</i> -PAA complexes produced at $Re=6000$	30
Figure 2-6. Solubility of β -carotene, CMC of PEO- <i>b</i> -PS (MW 3000- <i>b</i> -1000) (measured by Johnson and Prud'homme) and CMC of PEG- <i>b</i> -PCL (MW 5000- <i>b</i> -3600). The straight line represents the operating line for adding anti-solvent to a solution initially with 20 mg/mL β -carotene and 20 mg/mL of block copolymers.	34
Figure 2-7. The dependence of nanoparticle sizes on drug loading rate. Nanoparticles of β -carotene encapsulated in PEG- <i>b</i> -PCL were produced at $Re=3225$. The ratio of THF to water was 1:9 v/v.	35
Figure 2-8. Drug loading rates of SR13668 in PEG- <i>b</i> -PCL affected by molecular weights of block copolymer, drug to polymer weight ratios, and coprecipitators. (A) Drug loading of SR13668 in PEG- <i>b</i> -PCL with the same molecular weight of the	

hydrophilic block (MW 5000) and three different molecular weights of the hydrophobic block (MW 2300, 3600, and 6000). The drug to polymer weight ratio was 1:5. The starting concentration of the block copolymers was 1 wt%. (B) Drug loading of SR13668 in PEG- <i>b</i> -PCL (MW 5000- <i>b</i> -6000) at three drug-to-polymer ratios. The starting concentration of the copolymers was kept at 1 wt%, and the drug concentration varied from 0.1 wt% to 1 wt%. (C) The dependence of drug loading of SR13668 in PEG- <i>b</i> -PCL (MW 5000- <i>b</i> -2300) on the presence of three coprecipitators. The drug-to-polymer ratio was kept 1:10 wt/wt. The β -carotene-to-drug ratio was 1:2 wt/wt. The PCL (MW 5200 and 2400)-to-drug ratio was 1:10 wt/wt. The starting concentration of PEG- <i>b</i> -PCL (MW 5000- <i>b</i> -2300) was 1 wt%.....	38
Figure 2-9. Solubility of SR13668 and CMC of PEG- <i>b</i> -PCL (MW 5000- <i>b</i> -2300 and 5000- <i>b</i> -6000) in the mixed solvent of THF and water.	39
Figure 3-1. Schematic drawing of spray drying equipment.....	45
Figure 3-2. Size distribution of PEG- <i>b</i> -PCL (MW 5000- <i>b</i> -6000) nanoparticles encapsulating SR13668 over time. (A) At neutral pH over 4 weeks. (B) At different pH over two hours.....	49
Figure 3-3. Growth kinetics of SR13668, PLGA and SR13668 with PLGA (A) in 24 hours and (B) in first 10 minutes (dashed area in Figure 3-3A). SR13668 (black): SR13668 alone; PLGA1_1 (green): SR13668 to PLGA 1:1 ratio; PLGA1_2 (blue): SR13668 to PLGA 1:2 ratio; PLGA1_3 (wine): SR13668 to PLGA 1:3 ratio; PLGA1_4 (magenta): SR13668 to PLGA 1:4 ratio; PLGA1_2_trehalose (orange): PLGA nanoparticles (SR13668 to PLGA 1:2 ratio) in an aqueous solution with 300 mg/ml trehalose; PLGA (red): PLGA alone.	51
Figure 3-4. The growth kinetics of SR13668 with and without the coprecipitators. (A) Schematic drawing of homogeneous nucleation and growth of SR13668. (B) Schematic drawing of heterogeneous nucleation and growth of SR13668 with PCL. (C) The growth kinetics of the particles of SR13668, PCL, and SR13668 with PCL. The starting concentration of SR13668 was 0.1 wt%. For the particles of SR13668 with PCL, the ratio of PCL (MW 5200) and PCL (MW 2400) to SR13668 was 1:10 wt/wt. For PCL particles, the starting concentration of PCL was 0.1wt%.	52
Figure 3-5. The size distribution of PEG- <i>b</i> -PCL (MW 5000- <i>b</i> -6000) nanoparticles encapsulating SR13668 before and after being spray dried. The drug-to-polymer weight ratio was 1:5. The inlet temperature of the spray dryer was 75 °C. 60% ethanol was added to the inlet stream.	59
Figure 4-1. (A) Molecular structure of SR13668 and PLGA. (B) Flow chart of experiments. (C) Size distributions of SR13668-PLGA nanoparticle formulations before and after spray dry.....	63
Figure 4-2. <i>In vitro</i> release of SR13668 from the PLGA nanoparticles in MTBE-aqueous two phase system.	71
Figure 4-3. Concentration of SR13668 in mice whole blood and plasma after oral administration of the formulations.....	73
Figure 4-4. Mean drug levels in dog (A) plasma and (B) blood. Dogs were dosed at drug level of 2.8 mg/kg.	74

Figure 5-1. Mice behavioral studies, including tail-flick test, and hot-plate tests and naloxone-induced withdrawal jumps.	80
Figure 5-2. (A) Size distributions of PLGA curcumin and PEG- <i>b</i> -PLA curcumin nanoparticles before and after spray dry. Trehalose and leucine were added as excipients. Ethanol (60% v/v) was also added to the inlet stream. Dash lines: before spray dry. Solid lines: after spray dry. Black: PLGA curcumin nanoparticles. Red: PEG- <i>b</i> -PLA curcumin nanoparticles. (B) Growth kinetics of curcumin and PLGA curcumin (at 1:1 weight ratio). Size change in the first half hour (dash area) is separately plotted in the right corner. Black: curcumin alone; and red: PLGA curcumin (1:1 weight ratio).	87
Figure 5-3. <i>In vitro</i> release of curcumin from nano-curcumin formulations in MTBE-aqueous two phase system. (A) Schematic drawing of the MTBE-aqueous two phase system. (B) PLGA-curcumin formulation. (C) PEG-PLA-curcumin formulation. (D) Hybrid-curcumin formulation.....	89
Figure 5-4. Effect of curcumin nanoformulations on morphine tolerance. (A) Tail-flick assay. (B) Hot plate assay. Groups of 3 mice received 500 μ L curcumin nanoformulation (20 mg/kg) or saline (MS and Saline group) orally. After 15 min, 100 mg/kg morphine or saline (Saline group) were dosed subcutaneously. Four hours later, 10 mg/kg were administrated subcutaneously to all the groups. Tail-flick assay and hot-plate assay were performed 30 minutes after that.	91
Figure 5-5. Effect of unformulated free curcumin on morphine tolerance. (A) Tail-flick assay. (B) Hot-plate assay. Groups of 3 mice received 500 μ L curcumin (20 mg/kg) or saline (MS and Saline group) orally. After 30 minutes, 100 mg/kg morphine or saline (Saline group) were dosed subcutaneous. 4 hours later, 10 mg/kg were administrated subcutaneous to all the groups. Tail-flick assay and hot-plate assay were performed 30 minutes after that.....	92
Figure 5-6. Effect of curcumin and curcumin nanoformulations on morphine dependence. Groups of 3 mice were challenged with naloxone (10mg/kg) intraperitoneally 5 hours after the administration of 100mg/kg morphine. The mice were immediately put inside glass cylinders and the number of escape jumps in 15 minutes was recorded..	93

LIST OF ABBREVIATIONS

%MPE	the percentage of maximal possible effect
CFD	computational fluid dynamics
CIJ	confined impinging jet
C _{max}	maximum plasma concentration
CMC	critical micelle concentration
DMSO	dimethyl sulfoxide
DLR	drug loading rate
DLS	dynamic light scattering
EE	encapsulation efficiency
FNP	flash nanoprecipitation
HLB	hydrophilic-lipophilic balance
HPLC	high-performance liquid chromatography
I3C	indole-3-carbinol
LFCS	Lipid Formulations Classification System
LSBDDS	lipid and surfactant based drug delivery systems
LUVs	large unilamellar liposomes
MIVM	multi-inlet vortex mixer
MLVs	multilamellar liposomes
MP	mobile phase
MPS	mononuclear phagocyte system
PBS	phosphate buffered saline
PCL	poly(caprolatone)
PEG	poly(ethylene glycol)
PEG- <i>b</i> -PAA	poly(ethylene oxide)- <i>b</i> -poly(acrylic acid)

PEG- <i>b</i> -PCL	poly(ethylene oxide)- <i>b</i> -poly(ϵ -caprolactone)
PEG- <i>b</i> -PLA	poly(ethylene glycol)- <i>b</i> -poly(lactic acid)
PEI	polyethyleneimine
PLGA	poly(lactic-co-glycolic acid)
PEO- <i>b</i> -PS	poly(ethylene oxide)- <i>b</i> -poly(styrene)
<i>Re</i>	Reynolds number
RES	reticuloendothelial system
RESOLV	rapid expansion of supercritical solutions into liquid solvents
RESS	supercritical solutions
SAS	supercritical antisolvent
SMEDDS	self micro-emulsifying drug delivery systems
SUVs	small unilamellar liposomes
THF	tetrahydrofuran
TNP	traditional nanoprecipitation

SUMMARY

Minimal bioavailability of hydrophobic compounds limits their biomedical and biological applications. In this thesis, we have developed a continuous and scalable process to generate stable polymeric nanoparticles encapsulating hydrophobic drugs (such as beta-carotene, SR13668, and curcumin), based upon our understanding of the competitive kinetics of flash nanoprecipitation and spray drying. A custom-designed multi-inlet vortex mixer (MIVM) was employed to implement the process of flash nanoprecipitation (FNP). Flow patterns in the MIVM were microscopically visualized by mixing iron nitrate and potassium thiocyanate to precipitate $\text{Fe}(\text{SCN})_x^{(3-x)+}$. Effects of physical parameters (including Reynolds number, supersaturation rate, interaction force, and drug loading rate) on size distribution of the nanoparticle suspensions were investigated. The prepared nanoparticle suspensions through FNP were then spray dried to (1) achieve particle long-term stability, (2) quickly remove organic solvents used for nanoprecipitation, and (3) be able to conveniently adjust the nanoparticle concentration prior to use. Excipients such as sucrose, trehalose and leucine were used as "spacers" to prevent permanent aggregation during the spray drying process. The optimized condition was achieved by thoughtful consideration of the glass transition temperatures of the polymers and transport processes of evaporation and particle diffusion. The nanoparticles were then re-suspended prior to animal tests. Bioavailability and bioactivity of the nanoparticles were verified in animals for two compounds when orally dosed – SR13668 (a cancer preventive agent) and curcumin (a potential agent to attenuate morphine tolerance and dependence). Enhanced bioavailability of PLGA-SR13668 nanoformulation was observed in mice and beagle dogs, compared with formulations of Labrasol[®] and neat drug in 0.5% methylcellulose. Mice behavioral studies, include tail-flick, hot plate, and precipitate withdrawal experiments, were conducted to demonstrate the effects of curcumin nanoformulation on attenuating morphine tolerance and dependence. Significant

analgesia was observed in both tail-flick and hot plate experiments, while free curcumin at same concentration showed minimal effect.

CHAPTER 1. INTRODUCTION

1.1 Current challenges in nano-medicine and our approach

Nanoparticles have recently been the focus of much attention because of their broad biomedical applications in small molecule drug delivery,¹⁻³ gene and protein delivery,⁴⁻⁶ medical imaging and diagnosis,^{7,8} and photothermal therapy.⁹ The application of nanotechnology to drug delivery systems could improve many of the pharmacological properties of conventional drugs.^{1,10} With careful design of the drug delivery systems, it is possible to (1) enhance drug solubility; (2) regulate drug release from the drug delivery system; (3) improve pharmacokinetics; (4) reduce rapid clearance; (5) increase drug concentration at desired site; (6) deliver two or multiply drugs for combination therapy; (7) visualize the site of drug delivery by combining drugs and imaging agents; (8) overcome biological barriers.^{11,12}

In our study, we focus on applying polymeric nanoparticles to increase the bioavailability of the hydrophobic drugs, which are 90% of the new developed drugs and 40% of the drugs on market.¹³⁻¹⁵ Although molecular modification and nanoformulations of the drugs have been investigated to increase the drug solubility, it needs more complicate synthesis steps and further approval from FDA for the modified molecules. Nano-scale particles dramatically increase surface to volume ratio and particle solubility, which is different from the bulk solubility of the compound. Advances in nanotechnology have shown innovative solutions for targeted drug delivery and new methods for the fabrication of drug-delivery vehicles. However, drug loading was an issue for many systems for the polymeric particles prepared by the conventional procedures above, despite the ideal hydrophobic interaction between the drug and the hydrophobic block of the copolymer. Moreover, producing polymeric nanoparticles encapsulating hydrophobic drug compounds in a scalable and reproducible manner is the key for organic nanoparticles to be practically applied as novel medicine.

We have developed a continuous and scalable process to generate stable nanoparticles with high drug loading rate (DLR) and small size with narrow size distribution. Three steps are involved in this continuous and scalable process, as shown in Figure 1-1. First of all, polymeric nanoparticles with high DLR and narrow size distribution are generated by employing flash nanoprecipitation (FNP) in a multi-inlet vortex mixer (MIVM). Secondly, spray dry or freeze dry is used to transfer the liquid suspensions to dry powders, in order to achieve long-term stability. Thirdly, the nanoformulations are re-suspended in aqueous solutions for future application.

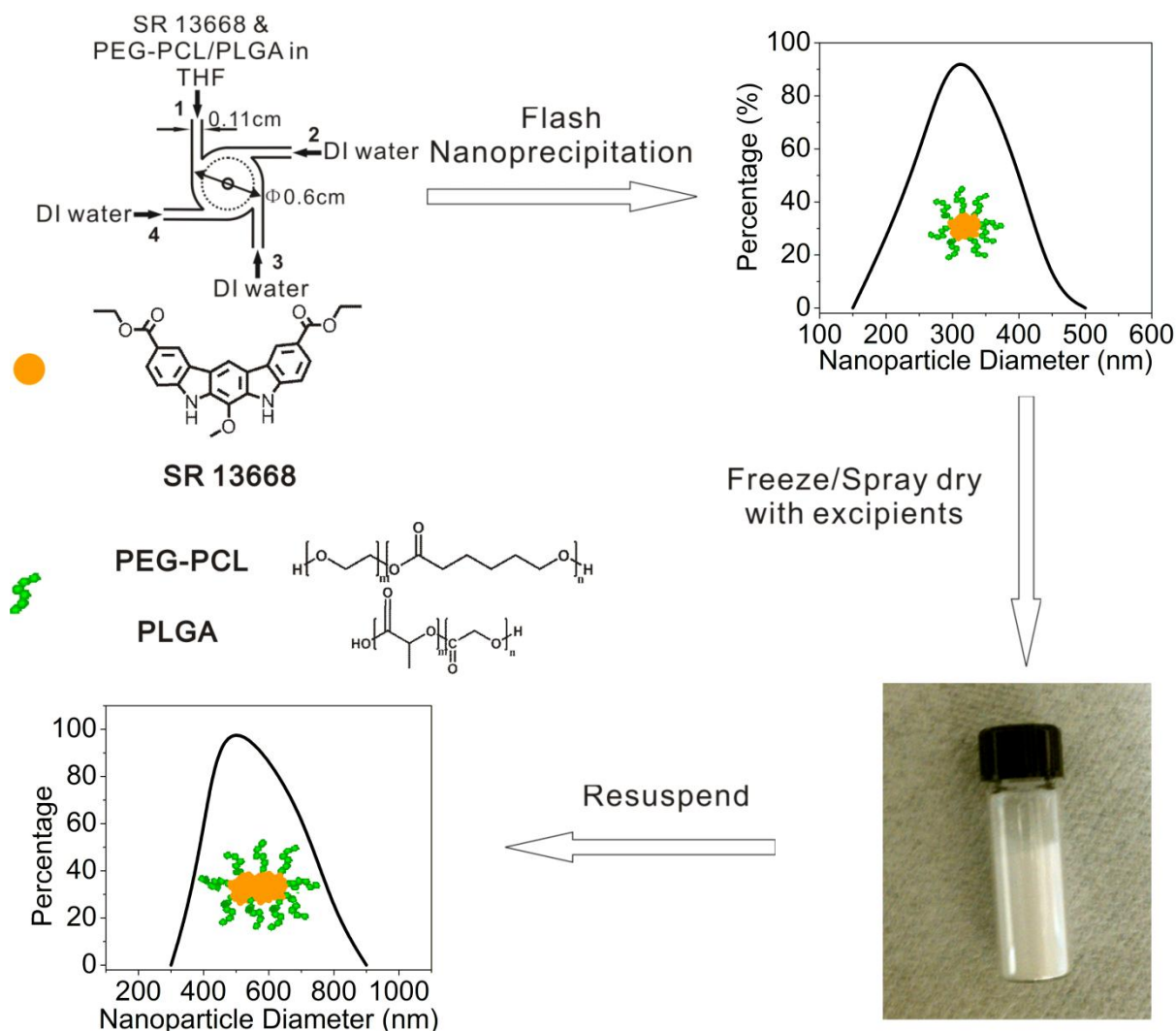


Figure 1-1. The steps of the continuous and scalable process. Nanoparticles encapsulating SR13668 were generated by using the MIVM, followed by nanoparticle characterization, freeze/spray drying, and re-suspension.

1.2 Current nano- and micro-particle drug-delivery systems.

Many drug delivery systems have been developed for different purposes, such as lipid and surfactant based drug delivery systems (LSBDDS), liposomes, dendrimers and polymeric micelles, as shown in Figure 1-2.

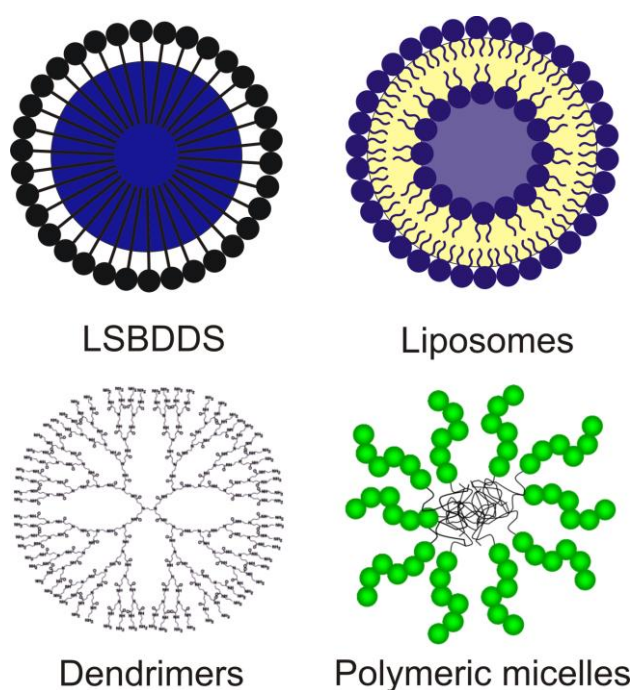


Figure 1-2. Schematic drawing of different drug delivery systems.

1.2.1 Lipid and surfactant based drug delivery systems

LSBDDS covers a broad range of different drug delivery systems, including oil solutions, emulsions and self micro-emulsifying drug delivery systems (SMEDDS).^{16,17} SMEDDS can contain up to four catalogues of components: drugs, lipids, surfactants and co-solvents. The lipid part aggregates with the hydrophobic drugs and forms the core of the particles. Surfactants are used to reduce the interfacial tension, cover the core of the particles and lead to the formation of micelles. The role of co-solvents is to facilitate the dispersion process.¹⁸

Despite there are many commercially available LSBDDS on the market, design of the LSBDDS are challenging and largely depend on empirical trial and error experiments, since the combination of lipids, surfactants and co-solvents could be infinite. A few empirical rules have been developed to facilitate the design of LSBDDS, such as (1) the hydrophilic-lipophilic balance (HLB) system;^{19,20} (2) Small's classification of lipids²¹ and (3) Pouton's Lipid Formulations Classification System (LFCS).^{22,23}

(1) HLB

The HLB system was developed to measure the degree of hydrophilic or hydrophobic of a surfactant. It was first described by Griffin²⁰ as

$$HLB = 20 \times Mh/M,$$

where Mh and M are the molecular weights of the hydrophilic and hydrophobic block, respectively. The HLB value varies from 0 to 20. A value of 0 means completely hydrophobic and a value of 20 means completely hydrophilic.

Davies later modified the calculate of HLB to be

$$HLB = 7 + m \times Hh - n \times Hl,$$

where m is the number of hydrophilic groups in the molecule, Hh is the hydrophilicity scale of the hydrophilic groups, n is the number of hydrophobic groups in the molecule and Hl is the hydrophobicity scale of the hydrophobic groups.

The advantage of Davies's method is that it takes into account the difference between strong and weak hydrophilic/hydrophobic groups.

(2) Classification of lipids

Small²¹ has developed the classification of lipids based on their physical interactions with bulk water and their behavior in the water-air interface. Lipids are classified into non-polar and polar lipids. The polar lipids are further divided into four groups, including insoluble

non-swelling (Class I), insoluble swelling (Class II) and soluble amphiphiles type A and B (Class III A and B).

Non-polar lipids are primarily made up of long-chain paraffins or unsubstituted aromatic compounds. Examples of non-polar lipids are cholesterol esters and paraffin oil. This class of compounds forms crystals or oil in water and don't spread to form monolayer on air-water interface.

Insoluble non-swelling lipids are the most hydrophobic lipids among the polar lipids, although they have at least one hydrophilic group on the molecule. They are insoluble in bulk water but could form stable monolayer on the surface of water. Examples of them are cholesterol and Vitamin A.

Insoluble swelling lipids are insoluble in water, but they could incorporate water with their polar head groups and form certain well-defined liquid crystalline structure at temperature above the phase transition temperature. Examples include phospholipids and lecithins.

Both soluble amphiphiles Type A and B could form micelles in water at relatively dilute solutions. They form unstable films on the surface of water. Both of them are capable of solubilizing other classes of lipids. Soluble amphiphiles type A differs from Type B because it forms liquid crystalline phases when small quantities of water are added to the compound. The micelle structure of the two types may also be different.²⁴ Examples of soluble amphiphiles Type A are classic detergents. Examples of soluble amphiphiles Type B are sulfated bile alcohols.

(3) LFCS

Pouton^{22,23,25} has developed the LFCS which classified LSBDDS to four different types, based on their composition and their ability to prevent drug precipitation, as shown in Table 1-1.

Table 1-1. The Lipid Formulations Classification System proposed by Pouton.²³

Excipients in formulation	Content of formulation (% w/w)				
	Type I	Type II	Type IIIA	Type IIIB	Type IV
Oils: triglycerides or mixed mono and diglycerides	100	40-80	40-80	<20	-
Water-insoluble surfactants (HLB < 12)	-	20-60	-	-	0-20
Water-soluble surfactants (HLB > 12)	-	-	20-40	20-50	30-80
Hydrophilic cosolvents (e.g. PEG, proylene glycol, transcitol)	-	-	0-40	20-50	0-50

Type I formulations consist of 100% oils, which are required to be digested. Type 1 formulations are the choice for many systems because of their simplicity and biocompatibility. However, Type I formulations have poor solvent capacity, thus they are only suitable to highly hydrophobic drugs.

Type II formulations consist of 40-80% oils and 20-60% water-insoluble surfactants. Water-insoluble surfactants improve the solvent capacity of the formulation. Self-emulsifying drug delivery systems can be formed upon gentle agitation.

Water-soluble surfactants are introduced to Type III formulations. Fine dispersions smaller than 100 nm can be formed under condition of gentle agitation.²⁶ Drug precipitation is possible when the formulation disperses. Many commercial available LSBDDS such as Cremophor RH40 and Labrasol belong to this catalog.

Type IV formulations are oil-free formulations based on surfactants and cosolvents. They are the most hydrophilic LSBDDS. They produce very fine dispersions and commonly offer high drug loading. Drug precipitation is possible when the formulation disperses.

These three classification systems facilitate the process of designing the appropriate LSBDDS. Porter²⁷ has also proposed seven guidelines for the design of LSBDDS which are

very useful. LSBDDS contributes to the improvement of oral solubility and bioavailability of hydrophobic drugs.^{28,29} However there are two major issues associated with the LSBDDS. The first one is that the undigested surfactants may not be suitable for chronic use. The second one is the possible drug precipitation when the formulations are dispersed in aqueous solutions.

1.2.2 Liposomes

Liposomes are spherical vesicles consist of single or multiple lipid bilayers with internal aqueous environment.^{30,31} Lipid bilayers are usually based on natural and synthetic phospholipids and cholesterol. Hydrophobic and hydrophilic drugs can be loaded into liposomes simultaneously. Hydrophobic drugs are trapped in the lipid bilayers and hydrophilic drugs are dissolved in internal aqueous environment. Liposomes are biocompatible and biodegradable because of their composition. They protect encapsulated drugs from degradation and can passively target organs and tissues with mononuclear phagocyte system (MPS). However, when MPS is not the target, polyethylene glycol-coated (STEALTH) liposomes need to be used to prevent the recognition by MPS.³²

Liposomes can be generally classified to multilamellar liposomes (MLVs), small unilamellar liposomes (SUVs) and large unilamellar liposomes (LUVs). MLVs contain multiple lipid bilayers which makes them a preferred candidate for encapsulating lipophilic compounds. SUVs have relatively small size (less than 50 nm) and narrow size distribution. The high surface to volume ratio of SUVs makes them a good choice for many applications. LUVs are generally larger than 50 nm. They are particularly suitable to encapsulate water-soluble compounds.

The process of liposome preparation can be divided into three stages: (1) preparation of the aqueous and lipid phases; (2) primary process (lipid hydration); (3) secondary process which is optional.³³

(1) Preparation of the aqueous and lipid phases

The aqueous solutions are used during the lipid hydration process to facilitate the liposome formation, thus the osmolarity, pH and ionic strength of the aqueous solutions need to be carefully designed. Hydrophilic compounds such as drugs and macromolecules are dissolved in aqueous solutions and encapsulated in liposomes during the primary process. Detergents are added to the aqueous solutions if the primary process involves detergent methods.

Lipids and lipophilic compounds are dissolved in suitable organic solvents either miscible (such as ethanol) or immiscible (such as diethyl ether) with water, depending on the methods to be used. Many methods require the lipid mixture to be dried. Solvent vaporization, freeze drying and spray drying can be used to remove the organic solvents.

(2) Primary process (lipid hydration)

Many methods have been developed for the lipid hydration process. The original film method developed by Bangham is probably still the simplest method.³⁴ In this method, dried lipid films are hydrated in aqueous solutions under vortexing. The drawbacks of this method are low encapsulation efficiency and heterogeneous size distribution.

Detergent solubilization method could generate liposomes in a reproducible manner and with homogeneous size distribution. Detergents are added in aqueous solutions to solubilize dried lipids or liposomes.^{35,36} Dialysis is used to slowly remove the detergents while the final structure of the liposomes is also formed during this process. Removal of residual detergents is very challenging in this process. A commercial available dialysis system called LIPOPREP (Diachema AG, Switzerland) was developed to remove detergents.³⁷

Instead of using dried lipid mixtures, many methods use lipid solutions to make liposomes, such as solvent injection and reverse phase evaporation.^{38,39} For solvent injection methods, lipid mixtures are dissolved in organic solvents either miscible or immiscible with

water. The solution is slowly injected into aqueous phase. If the solvent is miscible with water, then liposomes are immediately formed. Otherwise the removal of immiscible solvent leads to the formation of liposomes. For reverse phase evaporation methods, water in oil emulsion is formed in a two phase system containing lipids in organic phase and hydrophilic compounds in aqueous phase. The organic solvent is then removed under desired conditions. High encapsulation efficiency can be achieved by using this method.⁴⁰

(3) Secondary process

Secondary processes are used to modify the size and structure of liposomes. For example, ultrasonication and French Pressure Cell method⁴¹ can be used to convert MLVs to SUVs. Freezing and thawing method can be used to increase the size and encapsulation efficiency of SUVs and in some case convert SUVs to LUVs.⁴²

1.2.3 Dendrimers

Dendrimers are synthetic, branched polymers with precisely developed layer by layer structures.⁴³⁻⁴⁵ Commonly used dendrimers include polyamines,⁴⁶ polyaminoamines,⁴⁷ poly(aryl ethers),^{48,49} polyamides⁵⁰ and polyesters⁵¹ et al. Dendrimer structures can be divided into three parts: the core, the interior and the shell. The interior can be used to encapsulate drug molecules, while the shell has a large number of functional groups which can be used for potential bio-conjugations. The dendrimer generation is defined as the number of branch points moving outward from the core to the shell. Generation 10 dendrimers with maximum diameters of ~10 nm have been prepared,⁵² but dendrimers with even higher generation are challenge to synthesis because of steric restriction.

Dendrimers can be synthesized through two different approaches, either divergent or convergent. In the divergent approach, dendrimers are synthesized from the core to the surface.^{47,53} Polyfunctional cores react with multiple monomers so that the structure is built up generation by generation. The divergent approach can be used for the synthesis of

different kinds of dendrimers. However, its application is limited because multiple monomers have to be conjugated to a single core, which will result in the defects in the structure of dendrimers. For example, even when the desired reaction selectivity is 99.5%, only 29% of the fifth generation poly(propylene imine) dendrimer are perfect in structure.⁵⁴ In the alternative convergent approach, dendrimers are synthesized from the surface to the core.⁴⁸ The advantage of this approach is that only a small number of reactive sites are available for each step, which reduces the structural defects in dendrimers. However, the convergent approach is only suitable for the synthesis of dendrimers with low generation because steric barriers will hinder the reaction between large dendrons and small core.

The well-defined monodisperse structure of dendrimers makes it a promising candidate for drug delivery. Drugs could be either encapsulated in the core or conjugated to the surface of dendrimers. One thing that limits the application of dendrimers is their cytotoxicity, especially high generation cationic dendrimers. The attachment of poly(ethylene glycol) (PEG) to the surface of dendrimers has been widely used as a strategy to reduce the cytotoxicity of dendrimers.⁵⁵

Recently, hybrid nanoparticles have been developed by Hong's group,^{56,57} which take the advantage of both dendrimers and linear copolymers. The dendron part of the hybrid nanoparticles provides a precise control over the surface functional groups and multivalency. PEG is conjugated to the surface of the dendron which reduces the cytotoxicity of dendrons and provides long blood circulation time. Poly(caprolactone) (PCL) is conjugated to the tail of the dendron which serves as a hydrophobic core to incorporate a large number of hydrophobic drugs. Hybrid nanoparticles could self-assemble to micelles and remain stable even upon strong dilution in the blood circulation because of their low critical micelle concentration, which is 1-2 orders of magnitude lower than linear copolymers with similar HLB.⁵⁷

1.2.4 Polymeric micelles

Polymeric micelles are mainly self-assembled from amphiphilic block copolymers, when the concentration of block copolymers is higher than the critical micelle concentration (CMC). PEG is the most widely used hydrophilic block because it avoids the uptake of polymeric micelles by reticuloendothelial system (RES) and provides long blood circulation time. Polyesters, such as poly(D-lactic acid), poly(D,L-lactic acid), poly(glycolic acid), poly(ϵ -caprolactone) and poly(lactic-co-glycolic acid) are widely used as the hydrophobic block because they are biodegradable and biocompatible. Polymeric micelles have unique hydrophobic core hydrophilic shell structures. The hydrophilic shell provides steric stability and protects the drugs from external environments. The end group of the hydrophilic block can be functionalized to be hydroxyl, carboxyl and amino groups, which can be further conjugated to sugars and peptides for active targeting. The hydrophobic core incorporates with hydrophobic drugs through hydrophobic interaction and provides high drug loading capacity. The micellization kinetics of polymeric micelles also depends on the molecular weight of hydrophobic blocks. Higher molecular weight of the hydrophobic block results a lower CMC, thus the micellization kinetics is faster. Polymeric micelles are widely used for drug delivery of hydrophobic drugs^{58,59} because (1) their size distributions are narrow and their sizes are controllable, (2) their surface can be functionalized for active targeting, (3) passive targeting can be achieved through enhanced permeability and retention (EPR) effect, (4) high drug loading can be achieved, and (5) they are more stable upon strong dilution because of their lower CMC, compared to surfactant micelles. Although research in the area has undergone rapid expansion in the last decade, most polymeric micelles developed in research labs have not yet been applied in corresponding clinical treatments. One of the main reasons is the lack of control over physical properties and surface functionality during mass production of nanomaterials. Many methods have been developed for the preparation of

polymeric micelles, such as supercritical fluid process, oil-in-water emulsion method, nanoprecipitation and FNP.

(1) Supercritical fluid process

Supercritical fluids are solvents at temperature and pressure above their critical points. For practical purposes such as particle formation, supercritical fluids are typically at near critical temperature or critical pressure so that small changes in temperature or pressure result in large change in density, which facilitates particle formation. Water and carbon dioxide are the most widely used supercritical fluids because they are environmental friendly⁶⁰ and could solvate or precipitate solutes selectively. Although supercritical processing enables the production of pure drug compounds, it does not allow for control over surface properties of the particles. Two supercritical fluid processes are most widely used to form nanoparticles: rapid expansion of supercritical solutions (RESS) and supercritical antisolvent (SAS) process.

In the process of RESS, solute is first dissolved in a supercritical fluid. The supercritical fluid is then depressurized through a nozzle, which leads to supersaturation, rapid nucleation and growth, and eventually particle formation. Supercritical carbon dioxide is commonly used in RESS because it is a good solvent for many solutes.⁶¹ The advantage of this process is that it requires no organic solvent. The disadvantage is that solutes need to have fair solubility in selected supercritical fluids, and the size of particles produced by RESS is often in the micro-size range and has wide size distribution.⁶² In order to prepare nanoparticles with narrow size distribution, a modified process called rapid expansion of supercritical solutions into liquid solvents (RESOLV) was developed.⁶³ In RESOLV, the supercritical solution is expanded into a liquid instead of air, which suppresses the particle growth. Particles less than 100 nm and with narrow size distribution can be generated by using RESOLV.⁶³

SAS was developed for solutes which have poor solubility in supercritical fluids. In the process of SAS, polymer and drug are dissolved in a liquid solvent. The solution is then

sprayed into a chamber filled with supercritical fluid. As opposed to the RESS process, supercritical fluid acts as an anti-solvent to polymer and drug. Because of the rapid mass transfer between the supercritical fluid and liquid solvent, high supersaturation rate is achieved, which results in fast nucleation and growth, and eventually the formation of polymeric micelles. The advantage of this technique is that it is designed for continuous operations, which is critical for large-scale production of particles.⁶⁴ However, it is challenging to control the size, morphology and surface properties of the particles generated by using the SAS process.⁶⁵

(2) Oil-in-water emulsion method

Oil-in-water emulsion methods are widely used for the preparation of polymeric micelles. Two steps are generally involved in the process: (1) preparation of the emulsion and (2) formation of the polymeric micelles.⁶⁶ Polymer and drug are first dissolved in a water immiscible organic solvent. A large amount of water is then added together with surface active agents. The oil-in-water emulsions are formed by applying high energy emulsification techniques such as membrane emulsification and sonication.^{67,68}

After the formation of emulsion, polymeric micelles are formed when the organic solvents are removed by solvent evaporation or fast diffusion after dilution. In the process of solvent evaporation, volatile organic solvents such as dichloromethane and chloroform are used as the oil phase. The solvent is removed under reduced pressure which results the formation of polymeric micelles. In the process of fast diffusion after dilution, the emulsion is formed with a partially water-soluble organic solvent and a continuous water phase saturated with the organic solvent.⁶⁹ The subsequent addition of an excess amount of water to the system causes the diffusion of the organic solvent into the water phase, which results the formation of polymeric micelles.

The drawback of the oil-in-water emulsion method is the polydispersity of the final polymeric micelles because of the polydispersity of the original emulsion. Also, the drug loading depends on the partition coefficient of the drug into the hydrophobic core of the micelle, which means that the micelles always contain a minority of the drug compound.⁷⁰ Reported values for the concentration of drug in the final micelle are from fractions of a percent to values of no more than 20 wt%, which is too low for most therapeutic uses.^{71,72}

(3) Nanoprecipitation

The nanoprecipitation method, first described by Fessi et al.,⁷³ is a convenient, reproducible and low energy input process for the preparation of polymeric micelles. Briefly, polymer and drug are first dissolved in water miscible organic solvents such as tetrahydrofuran and acetone. Then a large amount of water is added as the non-solvent, which results the co-precipitation of polymer and drug, and eventually the formation of polymeric micelles. From the processing point of view, there are two different routes for solvent replacement, the dialysis route and the dropping route.⁷⁴ For the dialysis route, organic solvent with polymer and drug is placed in a dialysis bag and dialyzed against an excess amount of water for a long period of time. This process ensures the complete removal of organic solvent, but is comparatively time-consuming. For the dropping route, organic solvent with polymer and drug is added dropwise to a large amount of water. Following procedures to remove the organic solvent are necessary.

Compared to the oil-in-water emulsion method, surfactants, which might cause toxic effects after prolonged use, are not necessary for the nanoprecipitation procedure. The size and morphology of polymeric micelles can be controlled by varying parameters such as the concentration of polymer and drug, solvent to non-solvent ratio, polymer to drug ratio, and solvent replacement procedure et al. The drawback of the traditional nanoprecipitation method is that it is challenging to achieve fast mixing. Direct nanoprecipitation in a

traditional process results in heterogeneous mixing and polymeric micelles with polydispersed particle size and low drug loading rate. At high drug concentrations it is generally not possible to limit particle growth to smaller than 200 nm.⁷⁵

(4) FNP

FNP, first proposed by Johnson and Prud'homme,² is a scalable and reproducible process to prepare polymeric nanoparticles encapsulating hydrophobic drugs with controlled size distribution and high drug loading rate. Three time scales are essentially important in the FNP process: homogenous mixing time (τ_{mix}), polymer aggregation time (τ_{agg}), and organic solute nucleation and growth time ($\tau_{N.G.}$). The initial polymer aggregation and organic solute nucleation occur on much faster time scales than the mixing process. Therefore, the initial nanoparticle formation is mixing-limited. However, in the later stage, the kinetics of particle aggregation and growth becomes much slower, since the number concentration of the particles decreases rapidly and the hydrophilic block of the copolymer assembled on the surface of the particles provides steric stability. Eventually, as the aggregation number of the copolymer increases, the overall aggregation process is arrested and the nanoparticle is stabilized. Therefore, short mixing time ensures the solvent replacement starts homogeneously, so that the properties of the nanoparticles depend on the competitive kinetics of polymer aggregation and organic solute nucleation and growth. Rapid polymer aggregation results in the formation of dead micelles without any organic solute encapsulated inside, while rapid organic solute nucleation and growth results in undesired large particles.

A confined impinging jet (CIJ) mixer was developed for the process of FNP, provides rapid micromixing as fast as 1.5 milliseconds.⁷⁶ However, the CIJ mixer requires equal momentum of the two inlet streams, which could cause rapid particle growth via Ostwald ripening.⁷⁷ To overcome the limitation of the CIJ mixer, a MIVM (Figure 2-1A) was developed by Liu and Prud'homme.⁷⁸ Use of the MIVM provides flexibility to introduce

different compounds for formulation of nanoparticles with multiple active species, and also provides control over particle stability by allowing for the regulation of solvent/anti-solvent input ratios.⁷⁸⁻⁸⁰ Micromixing in the MIVM was characterized experimentally and numerically by using the competitive reactions of the acid-base reaction and 2,2-dimethoxypropane (DMP) hydrolysis.⁸¹ The fluid dynamics in the MIVM was investigated using microscopic particle image velocimetry (micro-PIV) and computational fluid dynamics (CFD).⁸² The micro-PIV data were used to exhibit the velocity field and to evaluate the accuracy of CFD models in simulating the flow within the MIVM.⁸² However, the physical parameters governing nanoparticle properties have not been presented by direct measurements on polymeric nanoparticles.

CHAPTER 2. SELF-ASSEMBLING PROCESS OF FLASH NANOPRECIPITATION IN A MULTI-INLET VORTEX MIXER (MIVM) TO PRODUCE DRUG-LOADED POLYMERIC NANOPARTICLES

2.1 Introduction

In this chapter, we studied the fundamental mechanisms of self-assembly to produce nanoparticles using the MIVM. An amorphous copolymer poly(ethylene oxide)-*b*-poly(styrene) (PEO-*b*-PS), a semicrystalline copolymer poly(ethylene oxide)-*b*-poly(ϵ -caprolactone) (PEG-*b*-PCL), and an ionic copolymer poly(ethylene oxide)-*b*-poly(acrylic acid) (PEG-*b*-PAA) were used to produce nanoparticles encapsulating small hydrophobic molecules (β -carotene as the model drug and SR13668), and cationic macromolecule polyethyleneimine (PEI). The molecular structures of the polymers and the drugs were shown in Figure 2-1. The dependence of nanoparticle sizes on Reynolds number (Re), supersaturation rate, nature of polymers, drug loading rate, and the type of interaction forces was studied. PEG-*b*-PCL and a hydrophobic model drug SR13668 were used to demonstrate the dependence of nanoparticle drug loading rate on sizes of each block of the copolymer, drug-to-polymer ratios, and the presence of coprecipitators. Mixing patterns in the MIVM were imaged by a light microscope.

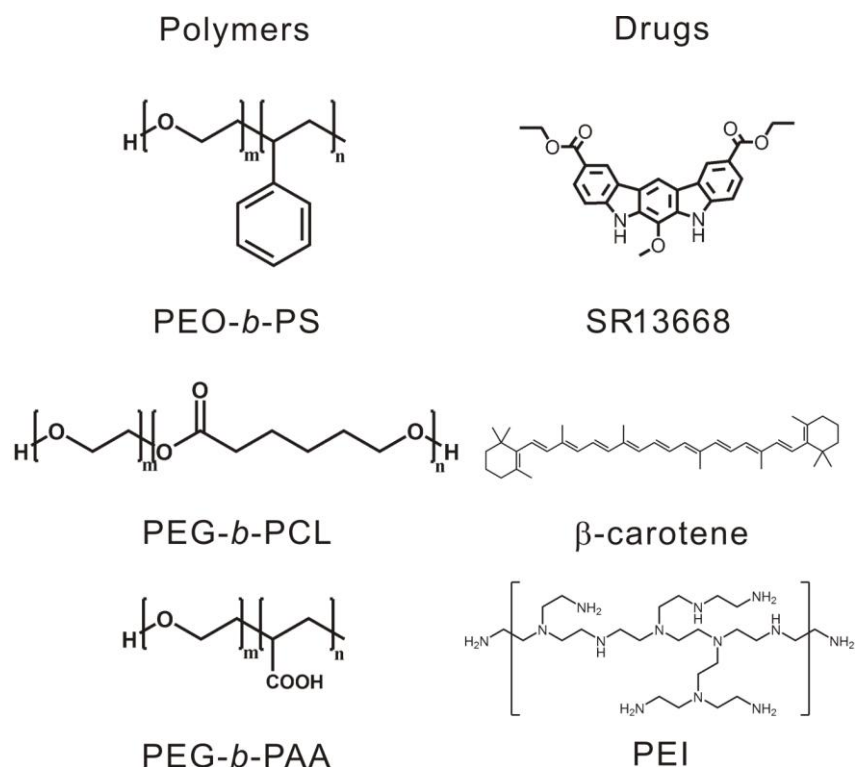


Figure 2-1. Molecular structure of the polymers and the drugs.

2.2 Experimental section

2.2.1 Materials

PEG-*b*-PCL of three different molecular weights (Mw 5000-*b*-2300, 5000-*b*-3600, and 5000-*b*-6000), PCL (MW 2400 and 5200) and PEG-*b*-PAA (Mw 6000-*b*-2000) were purchased from Polymer Source (Dorval, Canada). PEO-*b*-PS (Mw 1000-*b*-3000) was kindly provided by Goldschmidt GmbH (Essen, Germany). SR13668 was provided by National Cancer Institute (NCI) (Germantown, MD). β -carotene (95.0% purity), iodine, potassium iodide, tetrahydrofuran (THF), dimethyl sulfoxide (DMSO), potassium thiocyanate, iron (III) nitrate and branched PEI (Mw 750,000) were purchased from Sigma-Aldrich (St Louis, MO). Unless otherwise stated, all chemicals were purchased at standard grades and used as received.

2.2.2 Mixing and flow pattern visualization

Iron nitrate and potassium thiocyanate were used to image the mixing process in the MIVM. The dimensions and the imaging area of the MIVM were shown in Figure 2-3. The reactor and channel height was 1.53 mm. The inlet channel width was 1.19 mm. The reactor diameter was 6.26 mm, and the outlet diameter was 1.40 mm. To observe flow patterns in the MIVM composed of dilute solutions and suspensions as the conditions of making nanoparticle suspensions, inorganic dyes, iron nitrate and potassium thiocyanate, were used instead of organic dyes. Both of them do not have strong colors themselves, but when they are mixed together, red precipitation iron thiocyanate could be formed, which indicates the streamlines. The reaction scheme is indicated in Figure 2-2. Organic dyes were not used because they may affect the properties of aqueous solutions when dissolved at the concentrations sufficient for visualizing flow patterns in the MIVM.⁸³ Digitally controlled syringe pumps (Harvard Apparatus, PHD 2000 programmable, Holliston, MA) were integrated with the MIVM to accurately control the flow rates of the inlet streams. The solution from stream 1 and stream 3 was 1 wt% iron nitrate dissolved in DI water. The solution from stream 2 and stream 4 was 1 wt% potassium thiocyanate dissolved in DI water. Mixing of iron nitrate and potassium thiocyanate generated red precipitation of iron thiocyanate.



Figure 2-2. Reaction scheme of iron nitrate and potassium thiocyanate.

The four inlet streams had the same volumetric flow rate. Flow patterns in the center of the chamber, 6 mm in diameter, were observed under a microscope (American Scope, IN200A-P, Chino, CA) with an objective of 4x magnification and a digital microscope camera (Motic, Motacam 1000, Xiamen, China) coupled to an image analysis software (Motic images plus 2.0). The exposure time was 30 ms.

2.2.3 Nanoparticle preparation and characterization

Nanoparticles of β -carotene and SR13668 encapsulated in block copolymers, PEO-*b*-PS (Mw 3000-*b*-1000) and PEG-*b*-PCL (Mw 5000-*b*-2300, 5000-*b*-3600, and 5000-*b*-6000), were generated in the MIVM by hydrophobic interaction. For each copolymer used, stream 1 and 2 had the same volumetric flow rate. Stream 3 and 4 had the same volumetric flow rate, which was varied from 1 to 9 times the flow rate of stream 1 and 2 to obtain different supersaturation values. For nanoparticles of β -carotene encapsulated in PEO-*b*-PS (Mw 3000-*b*-1000), the solution from stream 1 was 1 wt% β -carotene dissolved in THF. The solution from stream 2 was 1 wt% PEO-*b*-PS (Mw 3000-*b*-1000) dissolved in THF. The other two streams were DI water. For nanoparticles of β -carotene encapsulated in PEG-*b*-PCL (Mw 5000-*b*-3600), the solution from stream 1 was PEG-*b*-PCL (Mw 5000-*b*-3600) with various concentrations from 1 wt% to 5 wt% and 1 wt% β -carotene dissolved in THF. For nanoparticles of SR13668 encapsulated in PEG-*b*-PCL (Mw 5000-*b*-2300, 5000-*b*-3600, and 5000-*b*-6000), the solution from stream 1 was PEG-*b*-PCL from 0.2 wt% to 2 wt%, 0.2 wt% SR13668, and the 0.02 wt% co-precipitators if any dissolved in THF. The other three streams were DI water.

Nanoparticles of branched PEI (Mw 750,000) encapsulated in PEG-*b*-PAA (Mw 6000-*b*-2000) were generated in the MIVM by electrostatic interaction. The solution from stream 1 was 1 wt% (or 2 wt%) PEG-*b*-PAA (Mw 6000-*b*-2000) dissolved in water. The solution from stream 2 was 0.43 wt% (or 0.86 wt%) PEI (Mw 750,000) dissolved in water. The

concentration was designed to have equal positive and negative charges. The other two streams were DI water. The volumetric flow rates of stream 1 and stream 2 were kept equivalent. The volumetric flow rates of stream 3 and stream 4 were kept equivalent and four times of that of stream 1 and stream 2.

Traditional nanoprecipitation (TNP) was also used to generate the PEG-PCL–SR13668 nanoparticles for comparison. 0.5mL organic solution (0.2 wt%-2 wt% PEG-*b*-PCL and 0.2 wt% SR13668 dissolved in THF) was added to 9.5mL Millipore water with the stirring of a magnetic stir bar, followed by rotating on a lab rotator (Thermo Scientific, Labquake, Waltham, MA, USA) for 10min.

Nanoparticle sizes and size distribution were measured by dynamic light scattering (DLS) (Agilent, 7030 Nicomp DLS/ZLS-size and zeta, Santa Clara, CA). The particle sizes were reported as the intensity-weighted radius a_h , where $a_h \propto \sum_{k=1}^{\max, \infty} n_k a_k^6 / \sum_{k=1}^{\max, \infty} n_k a_k^5$. a_k was the radius of particle k , and n_k was the number of particles at a given size.

The images of the particles were taken by using a transmission electron microscope (TEM) (JEOL Ltd., JEM-3010, Tokyo, Japan) operated at 300 kV. The sample of β -carotene encapsulated in PEG-*b*-PCL was prepared by placing 30 microliters of the suspension on a formvar grid. After 30 minutes, 20 microliters of 2% phosphotungstic acid (PTA) ($\text{H}_3\text{PO}_4 \cdot 12\text{WO}_3 \cdot 24\text{H}_2\text{O}$) (pH 6.9) was added to negatively stain the sample. Staining lasted for 2 minutes before PTA was removed by the filter paper. Detailed procedure of staining organic nanoparticles for TEM images can be found in the literature.⁸⁴ The sample was dried for 4 hours before taking the TEM images. The images of β -carotene particles without protection of polymers were taken as a comparison to the nanoparticles. 30 microliters of the sample was placed on a membrane-coated carbon grid and dried for 4 hours prior to imaging. For both cases, the concentration of β -carotene was 0.1 wt%.

The encapsulation efficiency (EE) and DLR of β -carotene and SR13668 in block copolymers was characterized by sequential processes of filtration, freeze-drying, re-dissolving, and UV-Vis measurements. The EE was calculated from the expression,

$$EE (\%) = \frac{\text{amount of } \beta - \text{carotene encapsulated in nanoparticles}}{\text{feeding amount of } \beta - \text{carotene}} \times 100\%$$

DLR was calculated from the expression,

$$DLR = \frac{\text{mass } \beta - \text{carotene encapsulated}}{\text{total mass of nanoparticles}} \times 100\%$$

The nanoparticles of β -carotene and SR13668 encapsulated in PEG-*b*-PCL were generated by using the MIVM and collected in a big reservoir of water (~100 times the dilution rate) to quench the reaction and prevent the fast growth of particle size due to Ostwald ripening. The nanoparticle suspensions were filtered through a 0.45 μm filter (VWR, 0.45 μm Polyethersulfone filter, West Chester, PA). β -carotene and SR13668 that was not encapsulated in the nanoparticles would form large crystals and be filtered out of the suspension. After the filtration, the nanoparticles were freeze-dried by using a freeze dryer (Labconco, FreeZone 6 liter console, Kansas City, MO) for 3 days. The nanoparticles were then re-dissolved in THF. The EE and DLR of β -carotene and SR13668 was quantified by using a UV-Vis spectrophotometer (Beckman Coulter, DU800 UV/Visible spectrophotometer, Brea, CA). The absorbance was measured at a wavelength of 310 nm.

2.2.4 CMC measurements

CMC of the diblock copolymers in water and THF mixed solvent was measured by using both the Baleux assay method⁸⁵ and the light scattering method.⁸⁶ PEG-*b*-PCL was dissolved in water and THF mixed solvent and agitated by using a vortex mixer (Boeckel, 270100 Tap Dancer-Vortex Mixer, Feasterville, PA). The concentration of PEG-*b*-PCL was much higher

than the CMC of PEG-*b*-PCL to ensure the formation of PEG-*b*-PCL micelles. Solution of PEG-*b*-PCL in mixed solvent was pipetted into 100K Molecular Weight Cut Off centrifuge tubes (Pall, 100K Nanosep Centrifugal Devices, Port Washington, NY) and centrifuged by a centrifuge (Fisher Scientific, Marathon 16KM microcentrifuge, Pittsburgh, PA) at 14000G for 15 minutes. The concentration of PEG-*b*-PCL in the mixed solvent through the membrane after centrifuge was considered as the CMC. Iodine-potassium iodide solution was made of 0.03 grams of iodine and 0.06 grams of potassium iodide in 3 milliliters of DI water. The solution was kept in a brown glass bottle no longer than 8 days. 0.05 milliliters of the iodine-potassium iodide solution was then added to 2 milliliters of PEG-*b*-PCL solution. The light absorbance was measured by a UV-Vis spectrophotometer (Shimadzu, UV-1601, Kyoto, Japan) at a wavelength of 500 nm. The Baleux assay method was only used on the samples of THF to water ratio equal to or less than 10%, because at a higher THF ratio, the light absorbance was influenced by the organic solvent. The light scattering method⁸⁶ was also used to analyze the CMC of PEG-*b*-PCL in water and THF solvent mixture. Various concentrations of PEG-*b*-PCL in solvent mixture were prepared and the CMC was identified by the jump in light scattering when micelles formed.

The solubility of SR13668 in mixed solvent of water and THF was quantified by UV-Vis spectrophotometer measurements at the absorbance wavelength of 310 nm. Millipore water was added to 10 mg/ml SR13668 in THF to make the desired solvent mixture (such as 10, 30, 40 and 50 v/v % THF). Samples were well mixed using a lab rotator (Thermo Scientific, Labquake, Waltham, MA) at room temperature for 24 hours and then filtered through a 0.02 μ m syringe filter (Whatman, Anotop 25, Maidstone, UK). The UV absorbance of the filtered solutions was measured at the wavelength of 310 nm and the solubility of SR13668 was calculated based on the calibration curve at the same wavelength.

2.3 Nanoparticle size and size distribution

2.3.1 Effect of flow field and Reynolds number: Starting the competitive kinetics simultaneously

FNP is a process of kinetic control instead of thermodynamic equilibrium which constrains the drug loading rate and causes broad size distribution and low stability as in most other processes, such as emulsion and traditional precipitation. At thermodynamic equilibrium, drug loading is driven by entropy of mixing of the drug with the hydrophobic core of the micelle. Based on Flory-Huggins theory and Chi mismatch, drug loading is disfavored.⁸⁷ The kinetic control of FNP overcomes the drug loading limit.

High Reynolds number homogenous mixing was essential to start the competitive processes of organic solute nucleation and growth as well as polymer aggregation simultaneously and uniformly, which provided control over drug loading rate and uniform particle size distribution. However, the appropriate definition of Reynolds number is not obvious for a system with multiple inlet streams of solutions with various velocities, dimensions, and viscosities like the MIVM. Regression modeling on data from previous MIVM research was used to develop an optimal formulation of Reynolds number (Re) as,⁸¹

$$Re = \left[\sum_i \left(\frac{Q_{base}}{Q_{acid}} \right) \left(\frac{Q_i}{Q_{total}} \right) Re_i^{2/3} \right]^{3/2} \quad (1),$$

where Q_{base} , Q_{acid} , Q_{total} , and Q_i represented the total volumetric flow rate of the base streams, the acid streams, the total volumetric rate of all streams, and flow rate of stream i , respectively. Re_i was the Reynolds number of the i th inlet stream calculated by the average velocity, viscosity, and dimension of the inlet stream. However, to be comparable to our previous simulation and experimental results, we kept the definition of Re in this study as,

$$Re = \sum_{i=1,N} V_i L / \nu_i \quad (2),$$

where V_i was the velocity of the i th inlet stream, L was the chamber diameter, ν_i was the kinematic viscosity of the i th inlet stream, and $N=4$ was the number of inlet streams.

Flow patterns inside an MIVM at various Re were visualized by mixing the streams of $\text{Fe}(\text{NO}_3)_3$ with KSCN to form inorganic complex $\text{Fe}(\text{SCN})_x^{(3-x)+}$ ($x \sim 3$, absorption maximum $\lambda_{\text{max}} \sim 480\text{nm}$, extinction coefficient $\varepsilon \sim 5 \times 10^3 \text{ cm}^{-1} \cdot \text{M}^{-1}$). The inorganic dye was chosen because of its Newtonian behavior. The viscosity of the solution of the complex was $1.08 \pm 0.05 \text{ mPa} \cdot \text{s}$ at the imaging concentration ($< 0.067 \text{ M}$).⁸³ The viscosity of the two colorless streams of $\text{Fe}(\text{NO}_3)_3$ ($< 0.067 \text{ M}$) and KSCN ($< 0.2 \text{ M}$) was $1.00 \pm 0.05 \text{ mPa} \cdot \text{s}$.⁸³ At the mixing front, the red precipitation of iron complex $\text{Fe}(\text{SCN})_x^{(3-x)+}$ indicated the streamlines. With higher Re , flow had more circulation and streamlines were closer. Eventually diffusion across the streamlines was fast enough to make the mixing in the MIVM homogeneous. At low Re , the mixing time, τ_{mix} , was given by,

$$\tau_{\text{mix}} = l^2 / 2D \quad (3),$$

where D (m^2/s) was the diffusion constant and l was the striation length, the distance over which mixing could occur by diffusion. For a molecule with a diffusion constant of $D=10^{-9} \text{ m}^2/\text{s}$, reducing l from $100 \text{ }\mu\text{m}$ to $1 \text{ }\mu\text{m}$ decreases τ_{mix} from 5 s to 0.5 ms . The images showed that increasing Re enhanced mixing by reducing the striation length. At Re over 1400 , the red precipitation of $\text{Fe}(\text{SCN})_x^{(3-x)+}$ is homogenous in the mixer under the microscope. Our previous results from numerical simulation and experimental analysis using competitive reactions revealed that adequate micromixing was obtained with Re over 1600 .⁷⁸

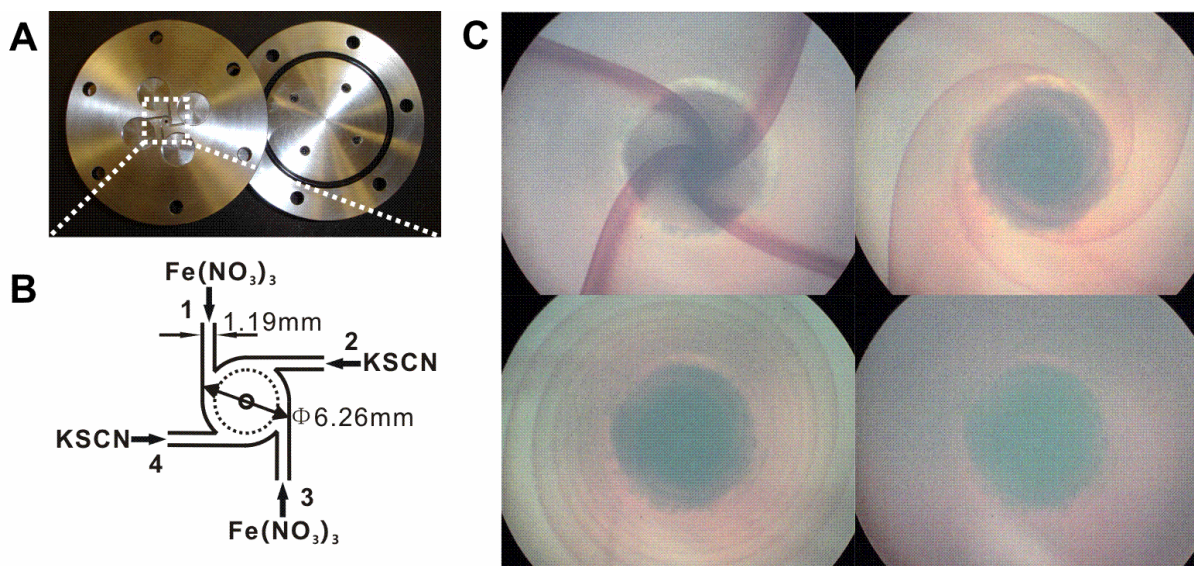


Figure 2-3. Design of a multi-inlet vortex mixer (MIVM) and images of mixing and flow patterns in the MIVM. (A) Photo of the MIVM. (B) Diagram of the reaction center of the MIVM with four tangential inlet streams for flow-pattern visualization. (C) Microphotographs of mixing and flow patterns in the MIVM. Imaging area was indicated by dashed circle in (B). Mixing of $\text{Fe}(\text{NO}_3)_3$ and KSCN generated red precipitation of $\text{Fe}(\text{SCN})_x^{(3-x)+}$ ($x \sim 3$) complexes. Mixing patterns depended on Reynolds number (Re). Clockwise from the upper left image in (C), Re was increased. (Upper left: $Re=267$. Upper right: $Re=537$. Lower left: $Re=806$. Lower right: $Re=1343$.)

The nanoparticle size dependence on Re is shown in Figure 2-4 and Figure 2-5. Similarly to our previous results from numerical simulation,⁷⁸ the transition happened at Re near 2000. With higher Re , the mixing was more homogeneous and effective. Over the critical Re (~ 2000), the flow was fully developed turbulence and the resulting particle sizes were not sensitive to the flow field. At low Re ($Re < 2000$), in Figure 2-4A and 2-4B, nanoparticle sizes increased with the decrease of Re , while in Figure 2-5A, nanoparticle sizes decreased with the decrease of Re . This opposite transition was because of the different interaction forces

between the encapsulated model drugs and diblock copolymers. The interaction between β -carotene and PEO-*b*-PS or PEG-*b*-PCL was hydrophobic interaction. The nanoparticle sizes depended on the competitive kinetics of polymer aggregation and β -carotene nucleation and growth. At lower Re , β -carotene and polymers were not homogeneously mixed, so that locally there were not sufficient polymers nearby to terminate the growth of β -carotene. Therefore the nanoparticle sizes were larger compared to the nanoparticles formed at higher Re . The interaction between positive charged PEI and negative charged PAA block of PEG-*b*-PAA is electrostatic interaction. At low Re , negative charged PEG-*b*-PAA had less chance to interact with positive charged PEI and nanoparticles were smaller compared to those generated at higher Re . At high Re ($Re > 2000$), the MIVM provided adequate micromixing. Nanoparticle sizes no longer depended on Re or the flow field.

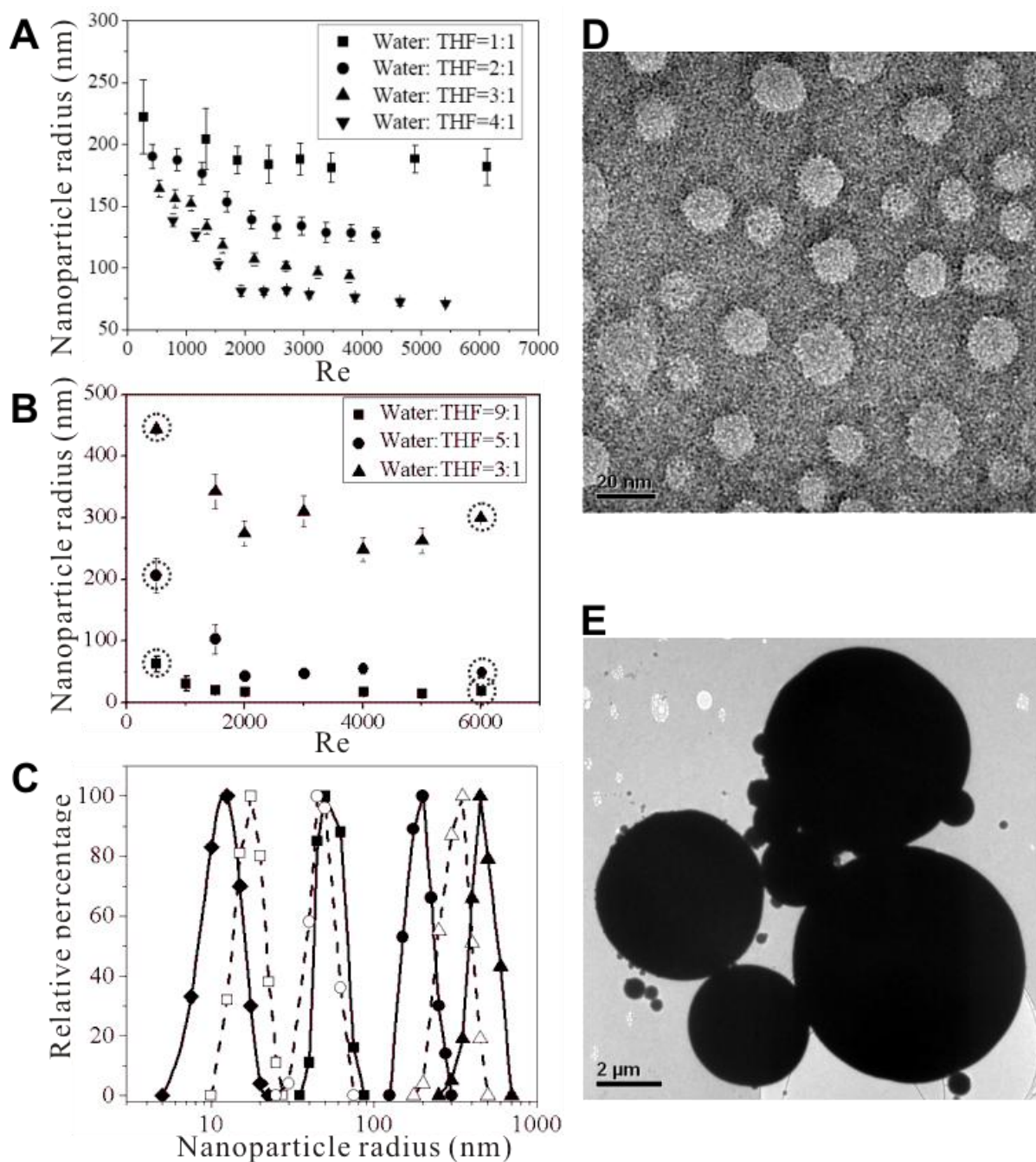


Figure 2-4. The dependence of nanoparticle size on Re , and supersaturation rate. (A) Sizes of PEO-*b*-PS nanoparticles encapsulating β -carotene. (B) Sizes of PEG-*b*-PCL nanoparticles encapsulating β -carotene. (C) Size distributions of PEG-*b*-PCL micelles and nanoparticles encapsulating β -carotene. The solid diamonds for the first curve in (C) indicate the size distribution of PEG-*b*-PCL micelles. The remaining six curves show the size distributions of PEG-*b*-PCL nanoparticles encapsulating β -carotene, which correspond to the six conditions

circled in (B) with the same symbol shapes. Hollow symbols in (C) denote that particles were generated at $Re=6000$, while solid symbols denote that particles were generated at $Re=500$. (D) The TEM image of β -carotene nanoparticles encapsulated in PEG-*b*-PCL generated at $Re=6000$. The scale bar represents 20nm. (E) The TEM image of β -carotene particles generated from direct precipitation without polymer protection. The scale bar represents 2 μ m.

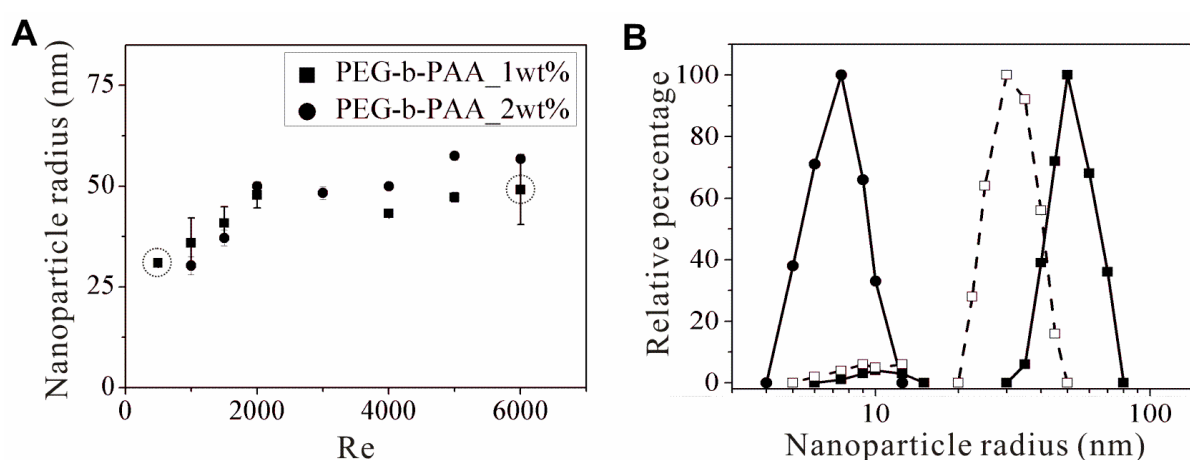


Figure 2-5. Sizes of PEI and PEI/PEG-*b*-PAA complexes. (A) Sizes of the PEI/PEG-*b*-PAA complexes versus Re . (B) Size distributions of PEI and PEI/PEG-*b*-PAA complexes. -●- PEI, -□- PEI/PEG-*b*-PAA complexes produced at $Re=500$, and -■- PEI/PEG-*b*-PAA complexes produced at $Re=6000$.

High Re homogeneous mixing was also critical for obtaining high DLR. The limited drug encapsulation from thermodynamic equilibrium could be discerned from the curves of solubility boundaries for organic solute and polymers as a function of anti-solvent addition (Figure 2-6). Figure 2-6 displays the solubility of β -carotene as a model hydrophobic drug

and CMC of two diblock copolymers, PEO-*b*-PS and PEG-*b*-PCL, as a function of THF content at room temperature. Gradual anti-solvent addition involved traversing the operating line from the initially pure solvent condition to the intersection first with the solubility curve of β -carotene and then with the CMC curves of the diblock polymers as the stabilizer. At the point when the operating line crossed the solubility curve of β -carotene, β -carotene would begin to precipitate as unprotected crystals until more anti-solvent was added and polymers started aggregation. However, when the operating line intersected with the CMC curves of polymers, more than 70% of β -carotene had precipitated and grew to be large crystals, which would be filtered out of the suspension. Not only this was a waste of the active compound, but DLR in the nanoparticles was also low. In the process of FNP, homogenous mixing could be reached in milliseconds to produce high levels of supersaturation for β -carotene as well as polymers at final solvent composition. The composition of the resulting nanoparticles was decided by the stoichiometry of the feeds instead of the partition coefficient of the drug with polymers. Therefore, polymeric nanoparticles with higher DLR were possible. When nanoparticles were generated at high Re in the MIVM, the EE of β -carotene in block copolymers was higher than 85%.

2.3.2 Effects of supersaturation rate and nature of polymers

Supersaturation rate directly affected the nucleation and growth time of the organic solute and polymer aggregation time. The rate of nucleation, J , was estimated by the primary homogeneous nucleation rate,⁸⁸

$$J \propto \exp \left[-\frac{16\pi\gamma^3\nu^2}{3k_B^3T^3(\ln S)^2} \right] \quad (4),$$

where γ was solid-liquid interfacial tension and ν was molar volume of the solute. S was the supersaturation ratio defined as,

$$S = c(r)/c^* \quad (5),$$

where $c(r)$ denoted the solubility of a particle with radius r and c^* was the equilibrium solubility. The rate for primary homogenous nucleation was derived by assuming that, for supersaturated solutions, solute molecules combined to produce embryos. Quasi-equilibrium developed between molecules and embryos, with a corresponding distribution of free energy due to the formation of a new volume and new surfaces. The nucleation rate calculated from equation 4 could be orders of magnitude different from experimentally measured rates, but the derivation captured the general features of particle formation.⁸⁸ By adopting homogeneous primary nucleation kinetics, the rate of block copolymer self-assembly was approximated by using equation 4 and inserting the value for supersaturation, S , defined as the ratio of polymer concentration over CMC. However, most primary nucleation in practice was likely to be heterogeneous nucleation, since supersaturation for homogeneous nucleation was much higher than heterogeneous nucleation. Heterogeneous nucleation could be estimated by using the same equation, but the surface energy of the solid-liquid interface was replaced by the surface energy of the solid-foreign surface interface. There are two proposed mechanisms to explain the effects of supersaturation on size distributions of organic particles protected by block copolymers. In one scenario, nucleation started as homogeneous nucleation of β -carotene, since β -carotene had higher supersaturation rate and therefore higher nucleation rate. Polymers then began to assemble on the surfaces of the particles and finally arrested the particle growth. In another scenario, hydrophobic sites on the polymers could have served as the nucleation seeds. Nucleation then started as heterogeneous nucleation, and particle growth stopped when polymer aggregation was terminated by the combined effects of particle dilution and steric hindrance of the hydrophilic block of the copolymer. With either mechanism, at higher supersaturation, more nucleation sites were generated and nanoparticles were smaller.

In this study, β -carotene and diblock copolymers were dissolved in THF and mixed with DI water as an anti-solvent. Different supersaturation rates were generated by varying the ratio of THF and DI water. In experiments, by varying THF and water ratio from 1:1 v/v to 1:5 v/v, the supersaturation was changed more than 100 times for β -carotene (from 12 to 1489). However, supersaturation rates for PEO-*b*-PS and PEG-*b*-PCL remained at about 20 and 5, respectively. Regardless of Re , nanoparticles of 50 nm to 500 nm could be produced by changing supersaturation rates (Figure 2-4A and 2-4B). Further models and experiments need to be developed to determine whether the dependence of nanoparticle properties on supersaturation rate is through nucleation kinetics of the organic solute or polymer assembly.

The long-term stability of the nanoparticles depended on polymer nature and solvent composition. At the same supersaturation rate of β -carotene, nanoparticles protected by PEO-*b*-PS were smaller than those protected by PEG-*b*-PCL (Figure 2-4A and 2-4B). Extensive studies⁸⁹⁻⁹³ have confirmed that the density of the coverage and the chain length of PEG influence the stability of the nanoparticles. Generally, longer PEG chain provides higher energy barrier to prevent nanoparticles from coagulation and degradation. Recent study also found the hydrophobic core may also affect the long-term stability of the nanoparticles.⁹⁴ Stability of PEO-*b*-PS nanoparticles encapsulating hydrophobic compounds has been discussed and reported in the literature.^{95,96} PCL, which is biocompatible and biodegradable, has many applications in drug delivery.⁹⁷⁻⁹⁹ However, the instability of PEG-*b*-PCL micelles and nanoparticles has been observed. One proposed mechanism was that low T_g PCL chains were sufficiently mobile on the surface and they could rearrange and begin to crystallize.⁹⁴ The lamella morphology of PCL crystal phase would allow aggregation into larger lamella structures. Further studies will be required to unambiguously explain the instability observed in many PEG-*b*-PCL nanoparticle systems.

Solvent composition affected long-term stability of nanoparticle suspensions by Ostwald ripening.^{77,95} The diffusion-controlled growth kinetics was given by,^{77,95}

$$\frac{dr}{dt} = \frac{\gamma v^2 D_{drug} c^\infty}{3RT r^2} \quad (6),$$

where D_{drug} and c^∞ represented the diffusivity and bulk equilibrium solubility of the organic solute in the solution, respectively, and r was the particle radius. Bulk solubility of the organic solute increased exponentially with linear increase of solvent concentration. Therefore, with higher solvent concentration, nanoparticles grew faster to be out of the nano-range. It was suggested that solvent had to be removed from the suspension quickly by flash solvent evaporation¹⁰⁰ or dialysis.

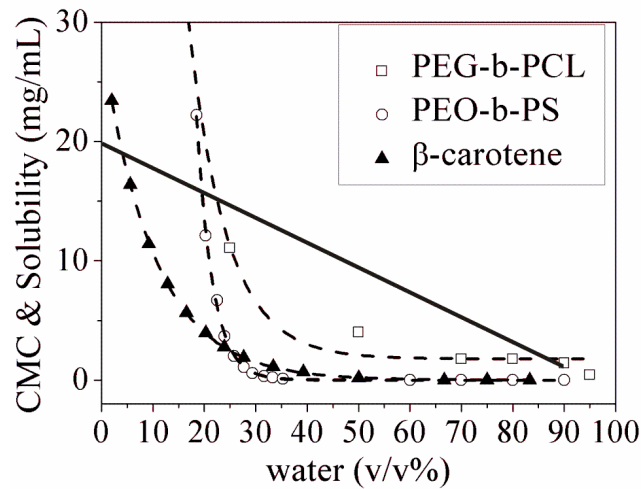


Figure 2-6. Solubility of β -carotene, CMC of PEO-*b*-PS (MW 3000-*b*-1000) (measured by Johnson and Prud'homme) and CMC of PEG-*b*-PCL (MW 5000-*b*-3600). The straight line represents the operating line for adding anti-solvent to a solution initially with 20 mg/mL β -carotene and 20 mg/mL of block copolymers.

2.3.3 Effect of drug loading rates

The dependence of particle size on DLR was measured by using PEG-*b*-PCL nanoparticles encapsulating β -carotene, with results presented in Figure 2-7. It was not surprising to find that nanoparticle diameters increased with higher DLR. At higher DLR, β -carotene nucleation and growth were relatively faster compared to the polymer micellization. Before the polymer arrested the growth of the particles, they had more time to become bigger. Figure 2-7 shows that with no drug encapsulated in the nanoparticles, as indicated by the intersection of the linearly extrapolated curve with y-axis, radius of the nanoparticles was 9 nm, which is consistent with the size of PEG-*b*-PCL micelles (Figure 2-4C). It is more interesting that the dependence of particle size on DLR was linear, which is consistent with our previous study on bifenthrin nanoparticles.¹⁰¹ We are conducting more experiments and simulations to explain the linear relationship of particle size and DLR.

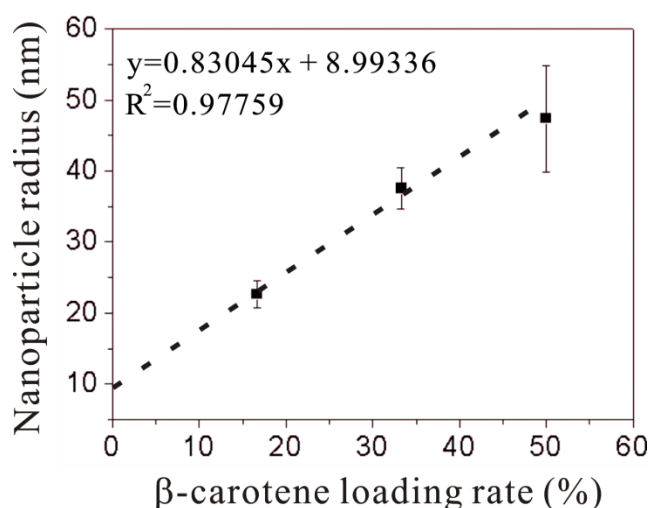


Figure 2-7. The dependence of nanoparticle sizes on drug loading rate. Nanoparticles of β -carotene encapsulated in PEG-*b*-PCL were produced at $Re=3225$. The ratio of THF to water was 1:9 v/v.

2.4 Nanoparticle drug loading

Traditional processes to prepare polymeric nanoparticles encapsulating hydrophobic compounds, such as emulsion and nanoprecipitation, generally have problems of low drug loading, broad size distribution, and difficulty of maintaining the stability of the nanoparticle suspensions. Based on Flory-Huggins theory and *Chi* mismatch, at thermodynamic equilibrium, drug loading driven by entropy change of mixing of the drug with the hydrophobic core of the micelle is disfavored.⁸⁷ FNP is a process of kinetic control instead of thermodynamic equilibrium, which overcomes the drug loading limit.

The polymeric nanoparticles encapsulating SR13668 were prepared using the MIVM at a high Reynolds number (*Re*) over 9000, ensuring that the solvent replacement started homogeneously and micromixing was uncoupled with organic compound nucleation and growth and polymer aggregation.¹⁰² The definition of *Re* was consistent with our previous studies.⁷⁸ In the process of FNP, in order to produce stable nanoparticles, the kinetics of polymer aggregation and drug nucleation and growth have to be comparable each other. Rapid polymer aggregation resulted in the formation of dead micelles without any SR13668 encapsulated inside, while rapid SR13668 nucleation and growth resulted in undesired large particles. The kinetics of polymer aggregation can be manipulated by the molecular weight of each block of the copolymer, the hydrophobic/hydrophilic properties of the polymers, and the initial concentration of the polymers. The nucleation and growth kinetics of the hydrophobic compound, SR13668, depends on the supersaturation rate and the presence of other hydrophobic molecules.

To demonstrate the importance of the kinetic control process, drug loadings of the nanoparticles prepared by FNP and by TNP were compared. The drug loadings of SR13668 in PEG-*b*-PCL at various polymer molecular weights, drug to polymer ratios, and the presence of the co-precipitator are reported in Figure 2-8. The highest drug loading of

SR13668 in PEG-*b*-PCL was about 13% which was achieved by using PEG-*b*-PCL (MW 5000-*b*-6000) at 1:5 wt/wt ratio of the drug to the polymer (Figure 2-8A), which is translated into 78% of the encapsulation efficiency. As a comparison, with the TNP, the highest drug loading rate could not exceed 1.25%. The molecular weight of the PEG block was kept constant at 5000, which was considered the appropriate length to prevent nonspecific protein absorption and therefore to obtain longer blood circulation of the nanoparticles. The molecular weight of the PCL block affected drug loading in three thermodynamic and kinetic aspects: critical micelle concentration (CMC), aggregation number, and micellization kinetics. When increasing the block length of the PCL block, the CMC was decreased (Figure 2-9). With the same solvent replacement, supersaturation rate was higher and the micellization happened faster. Further increase of PCL block length was not tested in this study, because higher ratio of the hydrophobic block to the hydrophilic block might present worm-like micelles rather than spherical ones.¹⁰³

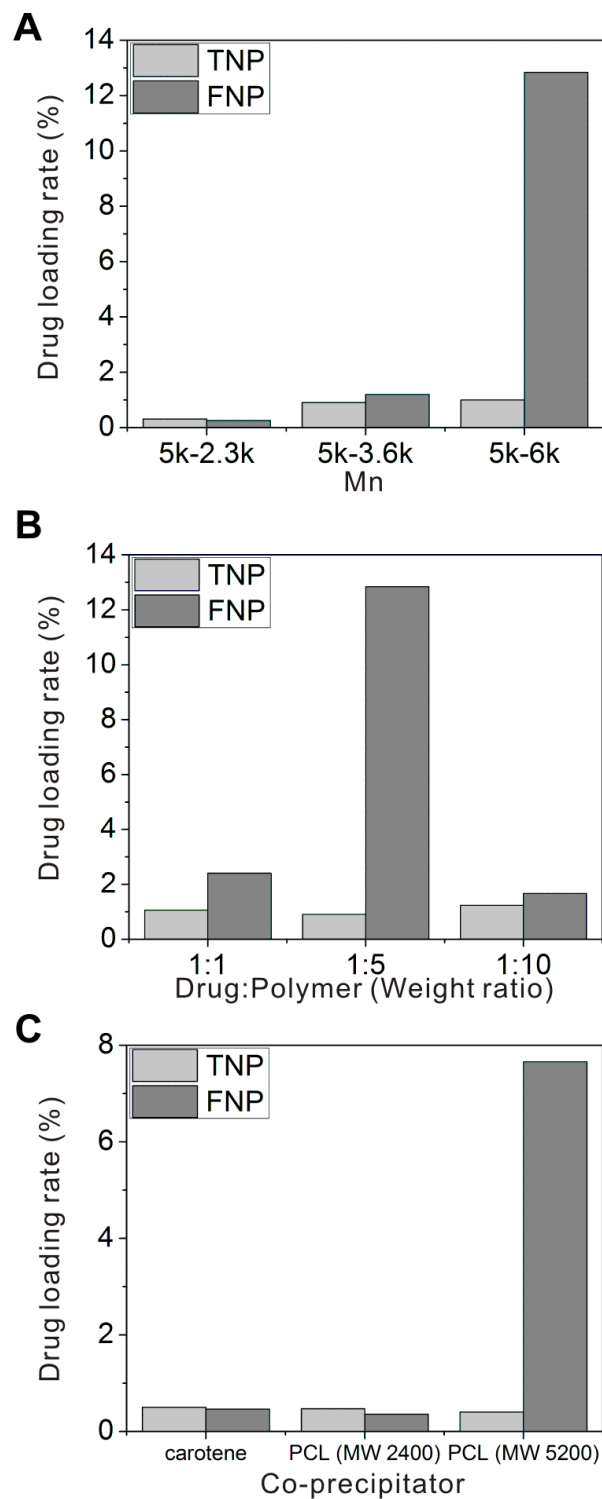


Figure 2-8. Drug loading rates of SR13668 in PEG-*b*-PCL affected by molecular weights of block copolymer, drug to polymer weight ratios, and coprecipitators. (A) Drug loading of SR13668 in PEG-*b*-PCL with the same molecular weight of the hydrophilic block (MW 5000) and three different molecular weights of the hydrophobic block (MW 2300, 3600, and

6000). The drug to polymer weight ratio was 1:5. The starting concentration of the block copolymers was 1 wt%. (B) Drug loading of SR13668 in PEG-*b*-PCL (MW 5000-*b*-6000) at three drug-to-polymer ratios. The starting concentration of the copolymers was kept at 1 wt%, and the drug concentration varied from 0.1 wt% to 1 wt%. (C) The dependence of drug loading of SR13668 in PEG-*b*-PCL (MW 5000-*b*-2300) on the presence of three coprecipitators. The drug-to-polymer ratio was kept 1:10 wt/wt. The β -carotene-to-drug ratio was 1:2 wt/wt. The PCL (MW 5200 and 2400)-to-drug ratio was 1:10 wt/wt. The starting concentration of PEG-*b*-PCL (MW 5000-*b*-2300) was 1 wt%.

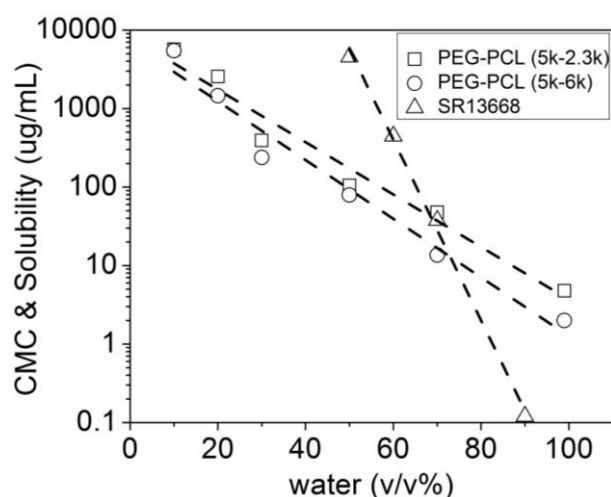


Figure 2-9. Solubility of SR13668 and CMC of PEG-*b*-PCL (MW 5000-*b*-2300 and 5000-*b*-6000) in the mixed solvent of THF and water.

For the system of PEG-*b*-PCL (MW 5000-*b*-6000) encapsulating SR13668, the optimized drug to polymer ratio is 1:5 wt/wt (Figure 2-8B). At higher drug to polymer ratio (such as 1:1 wt/wt), rapid organic solute nucleation and growth resulted in undesired large particles, which were filtered out by using the 0.45 μ m filter before the measurement of drug-loading.

At lower drug to polymer ratios (such as 1:10 wt/wt), in addition to the drug-loading limit (10%), rapid polymer aggregation caused the formation of dead micelles which resulted in larger particles eventually.

For PEG-*b*-PCL with lower molecular weight of the hydrophobic block (such as MW 5000-*b*-2300), drug loading was less than 1%. To improve the drug loading of SR13668 in this diblock copolymer, coprecipitators of other hydrophobic molecules (such as β -carotene, PCL (Mw 2400) and PCL (MW 5200)) were used. Presence of PCL (MW 5200) could greatly increase the drug-loading to 7.7%, but not PCL (MW 2400) and β -carotene.

2.5 Conclusions

This chapter demonstrated the fundamental mechanisms of self-assembly to produce nanoparticles using a multi-inlet vortex mixer (MIVM). It provided a method to better design optimized nanoparticles for biomedical applications such as drug delivery and bioimaging. The MIVM was able to provide rapid micromixing and high supersaturation values to produce nanoparticles with controlled size distribution and high drug loading rate. Nanoparticles of 50 nm to 500 nm were produced using the MIVM described in this paper.

Dependence of nanoparticle sizes on Reynolds number, supersaturation value, nature of polymers, drug loading rate, and type of interaction forces was characterized. High Re homogenous mixing was essential to start the competitive kinetics simultaneously and uniformly, which contributes to the formation of nanoparticles with controlled size distribution and high drug loading rate. Regardless of the definition of Re , there existed a threshold value, over which nanoparticle sizes were independent of Re . Microscopic images showed the transition of mixing patterns in the MIVM with the increase of Re . At high Re over 1400, diffusion across the streamlines was fast enough compared to the striation length so that we could not differentiate the separate streamlines indicated by the red precipitation of $\text{Fe}(\text{SCN})_x^{(3-x)+}$. This result was close to our previous numerical simulation and experimental

results which revealed that adequate micromixing was obtained with Re over 1600.⁷⁸ The transition Re indicated by imaging was slightly smaller than the one indicated by simulation results and other experimental measurements, because determination of homogenous mixing by imaging was limited by microscope resolution. With a larger magnification and shorter exposure time, the transition Re might further agree with the number found in our other studies. Despite the small discrepancy in the transition Re , it was suggested that all the drug loaded polymeric nanoparticles should be prepared at high Re over the threshold value. At low Re , the nanoparticle sizes either decreased or increased with the increase of Re , determined by the interaction forces of the self-assembling process. Further investigation is required to understand the process of nanoparticle formation when the system is composed of multiple compounds.

The solubility curve of the organic compound and the CMC curves of the polymers elucidated that in order to have high DLR, spontaneous mixing to reach high supersaturation rate was necessary. Traditional nanoprecipitation by hand mixing, titration, or dialysis could not achieve high DLR, since anti-solvent was slowly added to the system and a significant amount of organic solute precipitated out of solution before the polymers started to form micelles.

The supersaturation level played a key role in governing the size of nanoparticles encapsulating hydrophobic organic compounds in amphiphilic block copolymers. At higher supersaturation, with higher nucleation rate, more nucleation sites were generated and nanoparticles were smaller.

It was demonstrated that instantaneous mixing ensures the higher drug loading. With the same composition, traditional nanoprecipitation could never reach the same drug loading as achieved by flash nanoprecipitation. For a given drug compound, type of polymer, block length of the polymer, polymer to drug ratio, and presence of coprecipitator would all affect

the size distribution and drug loading. The goal of the design is to match the competitive kinetics of polymer micellization and drug nucleation and growth. At the low supersaturation rate presented in this study, it was more likely that SR13668 had heterogamous nucleation on the hydrophobic block of the copolymer. The polymers were then drawn together to form micelles by hydrophobic interaction.

In this chapter, we demonstrated that the MIVM can be utilized for encapsulation of a wide spectrum of materials spanning from model drugs such as β -carotene, SR13668 to hydrophilic charged polymers such as PEI, at very high encapsulation efficiency. Further studies on encapsulating other therapeutic molecules need to be accomplished to demonstrate the advantages of a MIVM for generating polymeric nanoparticles. The linear relationship of the DLR and nanoparticle size also needs further investigation.

CHAPTER 3. FLASH NANOPRECIPITATION INTEGRATED WITH SPRAY DRYING- DEVELOPMENT OF CONTINUOUS AND SCALABLE PROCESS

3.1 Introduction

Spray drying is a commonly used technique to generate dry powders from liquid solutions.¹⁰⁴⁻¹⁰⁶ It is widely used in food and pharmaceutical industries to increase the long-term stability of the products, to prevent undesired chemical and biological degradation and to reduce transportation and storage costs. Generally speaking, a spray dryer consists of an inlet stream for the liquids, an inlet stream for the hot gas, an atomizer to disperse the liquids, a drying chamber, a cyclone for gas and fine particles separation and a vial for product collection, as shown in Figure 3-1. Spray drying is a continuous process involving a combination of several stages, namely atomization, mixing of droplets with the drying gas, evaporation and product separation.¹⁰⁷

(1) Atomization

Atomization is a critical stage of the spray drying process because it generates droplets with different size and size distribution, which have a big impact on the following stages of the spray drying process. Liquid atomization could be achieved by using pneumatic atomizer, pressure nozzle and spinning disk configurations. In general, higher input energy results in smaller droplet sizes. When the input energy is a constant, higher inlet flow rate results in bigger droplet sizes. The purpose of atomization is to generate well dispersed micro-size droplets with high surface to volume ratio, which leads to the optimization of heat and mass transfer.

(2) Mixing of droplets with the drying gas

Hot gas is the heated drying medium. Air is the most widely used drying gas. However, if the liquid is a flammable solvent such as ethanol or the product is oxygen-sensitive, then an inert gas, usually nitrogen is used. The flowing direction of the drying gas could be co-

current or counter-current. In co-current process, the hot gas flows in the same direction as the sprayed liquid. The sprayed liquid evaporates immediately because of the hot gas (150 °C- 220 °C), while dry powders could be exposed to moderated temperature (50 °C- 80 °C), which limits thermal degradation.¹⁰⁸ In counter-current process, the hot gas flows in the opposite direction as the sprayed liquid. Dry powders are also exposed to high temperature, which limits its application. However, the counter-current process is economic preferred in term of energy consumption.

(3) Evaporation

After the mixing of droplets with the drying gas, heat and mass transfer balances between the gas and liquid phases are established. Heat transfers from the gas phase to the liquid phase because of the temperature gradient, while water transfers from the liquid phase to the gas phase because of the gradient of vapor pressure. Three steps could be classified during the whole evaporation process.¹⁰⁸ First of all, after the mixing of the droplets and the hot gas, heat transfer causes the temperature of the droplets increases to a constant value. The evaporation rate of droplet water increases with the increase of the temperature, and eventually reaches a constant value. After that, the evaporation rate of droplet water remains a constant under constant temperature and water vapor pressure. The diffusion of water from the core of the droplet to the surface is sufficient and equal to the constant evaporation rate. Finally, when the water content of the droplet reaches a critical value, the evaporation rate decreases rapidly and depends on the diffusion of the water from the core of the droplet to the surface. Eventually, drying is finished when the temperature of the dried particles equals to the temperature of the gas.

(4) Product separation

Cyclone is used to separate gas and dried particles. Gas exits through an outlet fan, while dried particles are collected by using a collection vial.

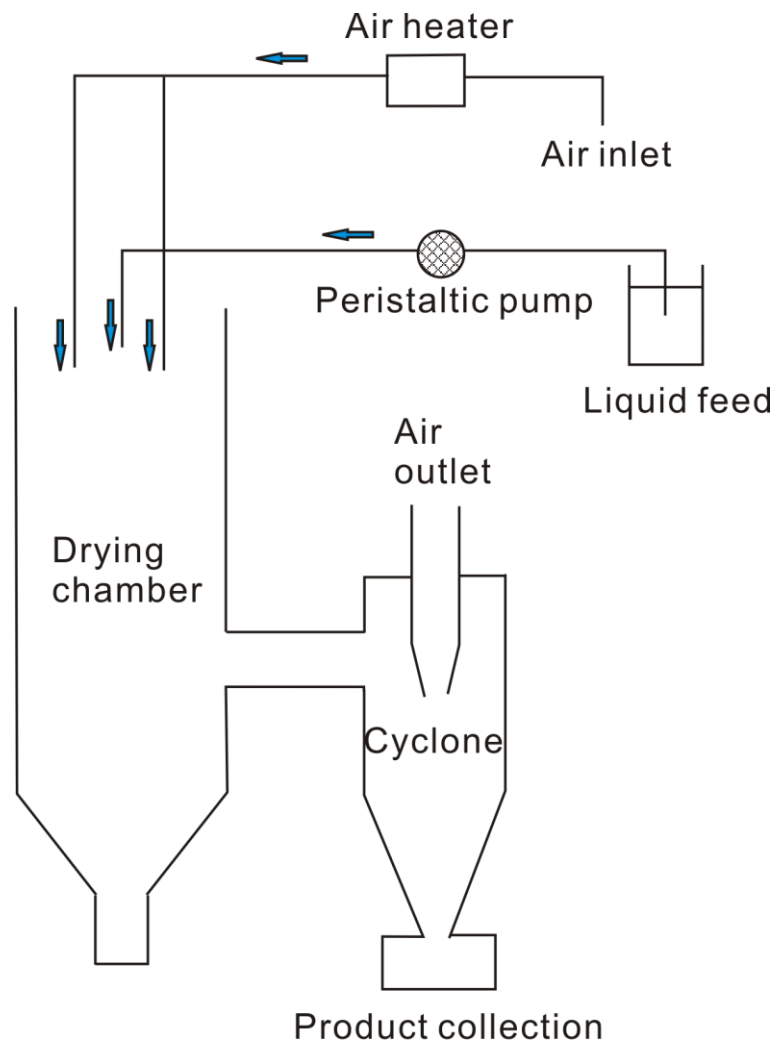


Figure 3-1. Schematic drawing of spray drying equipment.

In our study, we integrated the MIVM with the spray dryer, which is essential for the continuous formation of the stable nanoparticles by avoiding solution mediated particle aggregation and Ostwald ripening. The process is scalable, which can be used to generate milligrams of material for *in vitro* cell experiments or kilograms of material for *in vivo* tests in large materials. The spray dry conditions were optimized to re-suspend the nanoparticles in aqueous buffers. The optimized conditions for the freeze dry were also studied, which is similar to the spray dry conditions.

3.2 Experimental section

3.2.1 Materials

PEG-*b*-PCL of three different molecular weights (Mw 5000-*b*-2300, 5000-*b*-3600, and 5000-*b*-6000) were purchased from Polymer Source (Dorval, Canada). Poly(lactic-co-glycolic acid) (PLGA) (acid terminated, PLA:PGA 50:50, molecular weight (MW) 7000–17,000), THF, DMSO, ethanol, leucine, sucrose, and trehalose were purchased from Sigma-Aldrich (St Louis, MO). SR13668 was provided by National Cancer Institute (NCI) (Germantown, MD). Unless otherwise stated, all chemicals were purchased at standard grades and used as received.

3.2.2 Nanoparticle preparation and characterization

Nanoparticles of SR13668 encapsulated in PEG-*b*-PCL and PLGA were generated by using the MIVM. The detailed procedures to generate PEG-*b*-PCL nanoparticles encapsulating SR13668 were described in chapter 2. The details of the process to generate PLGA nanoparticles encapsulating SR13668 in the MIVM are as follows. Among the four inlet streams, stream 1 was with organic solution (0.2–0.8 wt% PLGA and 0.2 wt% SR13668 dissolved in THF). The other three inlet streams were Millipore (Billerica, MA, USA) water as an antisolvent to precipitate the drug compound (SR13668) and the copolymer (PLGA).

The volumetric flow rate of streams 1 and 2 was 6 mL/min and it was 54mL/min for streams 3 and 4.

Drug loading and encapsulation efficiency of SR13668 in nanoparticles was quantified by UV-Vis spectrophotometer measurements at the absorbance wavelength of 310 nm, after the sequential processes of filtration through a 0.45 μ m PES filter, freeze drying for three days, and being re-dissolved in DMSO at solid concentration of 2 mg/ml. Nanoparticle sizes and size distribution were measured by DLS (Agilent, 7030 Nicomp DLS/ZLS-size and zeta, Santa Clara, CA).

3.2.3 Freeze drying and spray drying of the nanoparticle suspensions

To maintain the long-term stability of the nanoparticles and to conveniently generate suspensions at various nanoparticle concentrations, freeze drying and spray drying, as the post processes after the particles were made, have been applied and optimized. To prevent the nanoparticles from aggregation, various amounts of excipients such as sucrose, trehalose, and leucine were added to the nanoparticle suspensions.

Before freeze drying, nanoparticle suspensions were dialyzed, dispensed in 20 ml amber vials, and then frozen in an ultra-low temperature freezer (Sanyo, MDF-U52VAT, Moriguchi, Japan) for 2 hours at -80 °C. The freeze-drying process lasted 3 days in a freeze dryer (Labconco, FreeZone 4.5 Liter Console Freeze Dry Systems, Kansas City, MO) at a vacuum pressure and -45 °C.

Spray drying of the nanoparticle suspensions was carried out by integrating the MIVM with a spray dryer (LabPlant, SD-05 Spray Dryer, North Yorkshire, UK). 60 v/v% ethanol was added in order to lower the inlet temperature of the spray dryer. The inlet temperature was set between 70 °C and 150 °C. The feed rate of the solutions was 10 mL/min. Spray-dried powders were collected in a glass container at the outlet of the spray dryer.

Re-suspension of the dried powders was done in Millipore water at 0.75 mg/mL at vigorous stirring for 10 minutes.

3.2.4 Measurements of particle growth kinetics

The growth kinetics of SR13668, PLGA, SR13668 with PLGA, and SR13668 with coprecipitators was measured in situ by using a DLS (NanoDLS; Brookhaven, Holtsville, NY) at the batch mode. Precipitations of SR13668, PLGA, SR13668 with PLGA, and SR13668 with coprecipitators were generated by using the MIVM. One of the four inlet streams was SR13668, PLGA, SR13668 with PLGA, and SR13668 with coprecipitators dissolved in THF. The other three inlet streams were Millipore water as the anti-solvent. The volumetric flow rate of streams 1 and 2 was 6 ml/min and it was 54 ml/min for streams 3 and 4. The samples were collected in a 100 ml beaker. Before the measurements, nano-suspensions of SR13668 and SR13668 with coprecipitators were diluted 10 times, whereas PLGA and PLGA encapsulating SR13668 were diluted 100 times using Millipore water to maintain the appropriate counting intensity. Water viscosity and refractive index were used for the measurements, which are 0.890 cP and 1.331, respectively.

3.3 Results and discussion

3.3.1 Stability of Nano-suspensions

Stability of the PEG-*b*-PCL-SR13668 nanoparticles was tested at neutral pH for four week and at low pH phosphate buffers for 2 hours, as shown in Figure 3-2. The stability of the nanoparticles at low pH was only tested for two hours because the formulation stays in the stomach for about two hours by oral administration. At neutral pH, over four weeks, the particles size was only slightly increased (Figure 3-2A). Because the hydrophilic block of the polymers should be able to provide enough steric stability and prevent particle aggregation, particle growth was mainly ascribed to Ostwald ripening. Although Ostwald ripening was slow as expected because of the low solubility of SR13668 in aqueous solutions,⁷⁷ the long-

term stability of nano-suspensions is still the concern when they are applied to biological and biomedical systems. Particle size distribution needs to be constantly measured and particle shelf time is limited. In our study, we have freeze dried and spray dried the nano-suspension into dry powder form. More details are presented in the next two sections. At very low pH, particle size decreased a little over the testing period of two hours, which is due to the enhanced degradation of PCL at the reduced pH (Figure 3-2B).

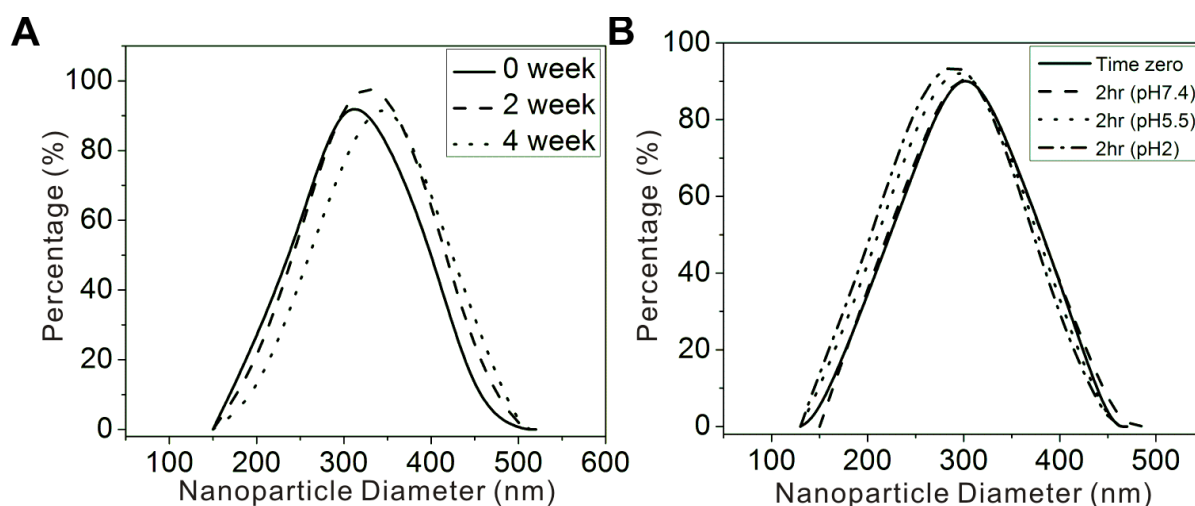


Figure 3-2. Size distribution of PEG-*b*-PCL (MW 5000-*b*-6000) nanoparticles encapsulating SR13668 over time. (A) At neutral pH over 4 weeks. (B) At different pH over two hours.

The growth kinetics of the PLGA-SR13668 nanoparticles (pure SR13668, pure PLGA, and SR13668:PLGA at 1:1, 1:2, 1:3, and 1:4 ratios) was measured for up to 24 h, as shown in Figure 3-3. Growth of SR13668 alone in first 10 min is in a linear fashion with a slope of about 55 nm/min. With the presence of PLGA at 1:1 ratio, the polymer was not enough to provide surface coverage and to prevent aggregation. The growth of the particles behaved similar as the pure SR13668. At higher PLGA to SR13668 ratios, the growth kinetics of the

complex was dominated by polymer aggregation. For the first 3 min, PLGA and PLGA–SR13668 particles grew even faster compared with the particles of pure SR13668 because PLGA has similar aggregation rates but larger radius of gyration. Eventually, the growth of the polymeric particles slowed down due to the surface charge repulsion. The growth kinetics of the polymeric particles in aqueous suspensions (at low SR13668 to PLGA ratios) is in a power-law fashion. Initial fast growth of the particles is mainly caused by aggregation because of the frequent particle collision; whereas slower particle growth in the later time span is predominately contributed by Ostwald ripening,⁷⁷ which cannot be prevented with the presence of solution as the molecular-transport media. To maintain the long-term stability of the particles, the suspensions were then spray dried into the format of solid powders. With the integrated MIVM and the spray drier, the complete process of producing dried nanoparticles took less than 10 min. Therefore, the growth kinetics of first 10 min is more critical to decide the size of the nanoparticles.

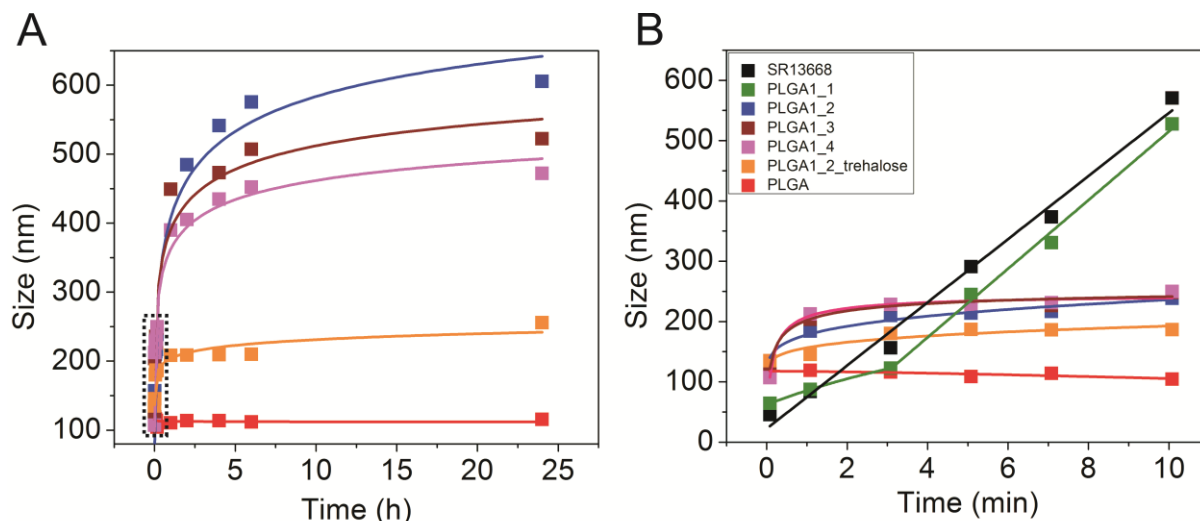


Figure 3-3. Growth kinetics of SR13668, PLGA and SR13668 with PLGA (A) in 24 hours and (B) in first 10 minutes (dashed area in Figure 3-3A). SR13668 (black): SR13668 alone; PLGA1_1 (green): SR13668 to PLGA 1:1 ratio; PLGA1_2 (blue): SR13668 to PLGA 1:2 ratio; PLGA1_3 (wine): SR13668 to PLGA 1:3 ratio; PLGA1_4 (magenta): SR13668 to PLGA 1:4 ratio; PLGA1_2_trehalose (orange): PLGA nanoparticles (SR13668 to PLGA 1:2 ratio) in an aqueous solution with 300 mg/ml trehalose; PLGA (red): PLGA alone.

The growth kinetics of free SR13668 alone and SR13668 with the coprecipitators were measured using DLS (Figure 3-4). The results showed that, with the presence of the coprecipitator, heterogeneous nucleation and growth dominated the process at low supersaturation rate, in which SR13668 attached with PCL to form a complex. Therefore, with the presence of PCL the particle growth was faster at the beginning because of the larger radius of gyration (R_g) of the polymer. Eventually the growth was slowed down and particles were stabilized at a few hundred nanometers because of the relatively slow growth and weak charge repulsion of the polymer. Compared to PCL (MW 2400), PCL (MW 5200) stabilized the growth of the complex at smaller size. Although β -carotene-SR complex also presented slow growth, the affinity of β -carotene to the hydrophobic block of the polymer was not as

high as PCL. Therefore, PCL (MW 5200) presented the optimized case among the three coprecipitators to increase the drug loading of SR13668 in PEG-*b*-PCL (Mw 5000-*b*-2300). Quantitative analysis requires the assistance of numerical simulation.

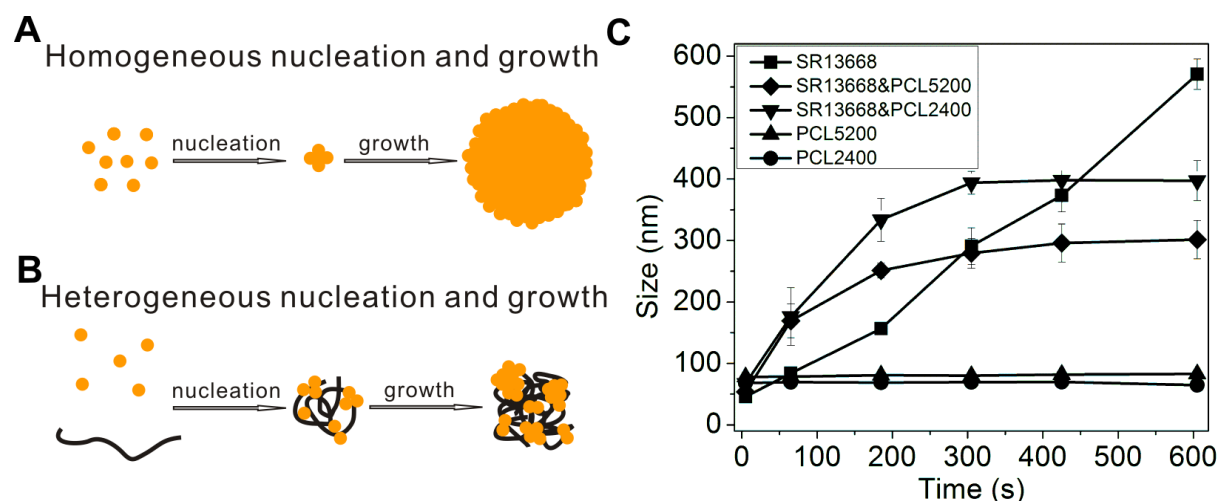


Figure 3-4. The growth kinetics of SR13668 with and without the coprecipitators. (A) Schematic drawing of homogeneous nucleation and growth of SR13668. (B) Schematic drawing of heterogeneous nucleation and growth of SR13668 with PCL. (C) The growth kinetics of the particles of SR13668, PCL, and SR13668 with PCL. The starting concentration of SR13668 was 0.1 wt%. For the particles of SR13668 with PCL, the ratio of PCL (MW 5200) and PCL (MW 2400) to SR13668 was 1:10 wt/wt. For PCL particles, the starting concentration of PCL was 0.1wt%.

In order to keep the long-term stability of the nanoparticles and to conveniently adjust the final concentration of the nanoparticles, nano-suspensions were dried to the form of solid powder by either freeze-drying or spray-drying processes. Although the original size distribution of the particles was not reproduced by the re-suspension probably due to

formation of dimers and/or trimers, all the re-suspended particles were in a submicron size range that may maintain the advantages of small particles.

3.3.2 Reproduction of freeze-dried nanoparticles

Freeze drying has been widely used to improve the long-term stability of nanoparticles.^{109,110} However, various stresses are generated during the freezing and drying process so that the nanoparticles aggregate and cannot be redispersed back to their original size. Cryoprotectives, such as leucine, sucrose and trehalose, are usually used to protect the nanoparticles from aggregation during the freezing and desiccation process. Mainly two mechanisms have been proposed to explain the effects of cryoprotectives: the glass dynamics hypothesis and the water replacement hypothesis. The “glass dynamics hypothesis”¹¹¹ states that the cryoprotectives could form a rigid and inert matrix with a high viscosity to “imprison” the nanoparticles in the matrix, thus reducing the mobility of the nanoparticles and preventing the aggregation. The “water replacement hypothesis”¹¹² considers that the cryoprotectives could form hydrogen bonds at the specific sites on the surface of the nanoparticles and substitute the place of water which is lost during the drying process. To reproduce the nanoparticles, we have tested three sugar-type cryoprotectives, leucine, sucrose and trehalose, and optimized the conditions.

In the freeze-drying process, the concentration of nanoparticles was kept constant and various amounts of cryoprotectives were added to the nanosuspension to reach different ratios. When increasing the amount of leucine, more submicron size particles were obtained (from 0% to 25.7% as the nanoparticle to leucine ratio decreased from 7:3 to 3:7). Although following the trend to further increase the amount of leucine may provide a better re-suspension, it is limited by the solubility of leucine in water at about 20 mg/ml.

Table 3-1. Re-suspension of nanoparticles in Millipore water after being freeze dried with various amounts of leucine. The nanoparticles were PEG-*b*-PCL (MW 5000-*b*-6000) encapsulating SR13668 at a polymer-to-drug ratio of 5:1 wt/wt.

	NP to leucine ratio	Peak 1 (percentage)	Peak 2 (percentage)
leucine_30	7:3	NO	3747nm (100%)
leucine_40	6:4	319nm (13%)	2117nm (87%)
leucine_50	5:5	337nm (17.8%)	2010nm (82.2%)
leucine_60	4:6	600nm (23.5%)	7669nm (75%)
leucine_70	3:7	476nm (25.7%)	2207nm (73%)

More water soluble sugar compounds, such as sucrose and trehalose, were used as the cryoprotectives and the re-suspension of the nanoparticles in Millipore water was reported in Table 3-2. With particle to sucrose ratio at 1:100 and particle to trehalose ratio at 1:50, submicron-size particles could be fully re-dispersed. In the current system, trehalose is a better cryoprotective compared to sucrose, since re-suspension of trehalose_50 could achieve smaller particles compared to sucrose_100, even though the amount of sugar in trehalose_50 formulation was only half of that in sucrose_100. Compared to the original nanoparticle suspension with average particle size about 300 nm, permanent dipoles formed in the re-suspension. The re-suspended nanoparticles of sucrose_100 and trehalose_50 were 630nm and 450nm, respectively. To completely reproduce the original nanosuspension, more cryoprotective is necessary. However, to optimize the formulation, one has to consider the limited amount of sugar that can be dosed to animals and patients.

Table 3-2. Re-suspension of the nanoparticles in Millipore water after being freeze dried with sucrose and trehalose. The nanoparticles were PEG-*b*-PCL (MW 5000-*b*-6000) encapsulating SR13668 at a ratio of 5:1 wt/wt.

	Sugar	NP to Sugar ratio	Observation by naked eyes	Average particle size
sucrose_10	sucrose	1:10	Lots of macroscopic precipitates	>1 μm
sucrose_20	sucrose	1:20	Lots of macroscopic precipitates	>1 μm
sucrose_40	sucrose	1:40	Some macroscopic precipitates	>1 μm
sucrose_100	Sucrose	1:100	Homogeneous suspension	630nm
trehalose_20	trehalose	1:20	Some macroscopic precipitates	>1 μm
trehalose_50	trehalose	1:50	Homogeneous suspension	450nm
trehalose_50 (leucine 2.3)	trehalose & leucine	1:50 & 1:2.3	Homogeneous suspension	660nm

3.3.3 Reproduction of spray-dried nanoparticles

Organic solvents are usually used to dissolve the hydrophobic compounds and the polymers in nanoprecipitation processes, and need to be completely removed before any biomedical application is attempted. Moreover, the bulk solubility of the hydrophobic drug increases exponentially with the presence of the organic solvent. Therefore, the transport-limited process of Ostwald ripening happens faster and particles keep growing bigger.⁷⁷ The most common process to eliminate the organic solvents is dialysis, which is time consuming and not scalable. Because a small amount of low-boiling-point organic solvent (such as THF) can facilitate solvent evaporation during the spray-drying process, dialysis of the nanosuspension is not necessary after we integrated the MIVM with the spray drier, which

not only reduced the preparation time resulting in better stability but also ensured the scalability of the process. To prevent permanent aggregation during spray drying and to be able to re-suspend the nanoparticles, sugar molecules were added as the excipients. Addition of sugar molecules also helped to reduce the collision rate of the particles because of the high viscosity of the solution.¹¹³ Various types of sugar molecules (i.e., leucine, sucrose, trehalose) at various concentrations have been tested. The results were reported in Table 3-3. Leucine was more effective per mass. At 1:5 ratio of nanoparticles to leucine, the PLGA-SR13668 nanoparticles could be re-dispersed to 445 nm. However, because the solubility of leucine in water is limited at 20 mg/mL, solutions at higher concentrations could not be prepared. By using trehalose and leucine together, the nanoparticle size could be further reduced to be 340nm in diameter, whereas a small peak of about 80nm also appeared. Compared with the original size of the particles before spray drying (150 nm), the particles of about 340nm are most likely to be the dimers formed in the re-suspension.

Table 3-3. The sizes of the resuspended nanoparticles (PLGA (MW 7000-17000) encapsulating SR13668 at ratio of 2:1) depend on the type and amount of excipients.

Excipient molecule	NP to sugar mass ratio	Inlet temperature	Particle size (nm) after resuspension
trehalose	1:150	140 °C	529.1
trehalose	1:200	140 °C	406.3
Sucrose	1:200	140 °C	405.2
Leucine	1:5	140 °C	445.5
trehalose & leucine	1:200 & 1:5	140 °C	341.1
trehalose & leucine	1:300 & 1:5	140 °C	339.4(85%) & 79(12%)

Because of the relatively low-glass-transition temperature of the PLGA used (~60 °C), high inlet temperature of the spray drier may induce active chain motion and result the permanent aggregation of the particles. However, relatively high inlet temperature is necessary to sufficiently dry the nanoparticles during the spray drying process. Ethanol is widely used to lower the inlet temperature because of its low boiling point. Because neither PLGA nor SR13668 dissolves in ethanol, addition of ethanol should have minimal (if any) effect on PLGA–SR13668 nanoparticle stability. In our study, 60% ethanol was added to the inlet stream. The inlet temperature was varied from 100 °C to 70 °C to optimize the spray-drying process (Table 3-4). At the inlet temperature of 75 °C, population of the sub-200nm particles reached the peak. The PLGA–SR13668 nanoparticles generated under this condition were used in subsequent *in vitro* and *in vivo* release tests. When inlet temperature was further reduced, the size of the re-suspended nanoparticles became bigger again, which might be the result of insufficient drying.

Table 3-4. The sizes of the re-suspended nanoparticles (PLGA (MW 7000-17000) encapsulating SR13668 at ratio of 2:1) depend on the inlet temperature of the spray drier. 300 times trehalose and 5 times leucine were added as excipients. 60% ethanol was also added to the inlet stream.

Inlet temperature	Size (nm)
100 °C	526(63%) & 112 (37%)
90 °C	505(62%) & 112 (37%)
85 °C	629(41%) & 138 (59%)
80 °C	600(41%) & 130 (59%)
75 °C	622(31%) & 139 (69%)
70 °C	339.4(85%) & 79(12%)

For PEG-b-PCL nanoparticle suspensions, based on the tested freeze-drying conditions, 50 times of trehalose was added to the nanoparticle suspensions when they were spray dried. The sizes of the nanoparticles before and after spray drying were shown in Figure 3-5. The average size of the re-suspended particles was about 450 nm, which is comparable to the size of the nanoparticles after being freeze dried.

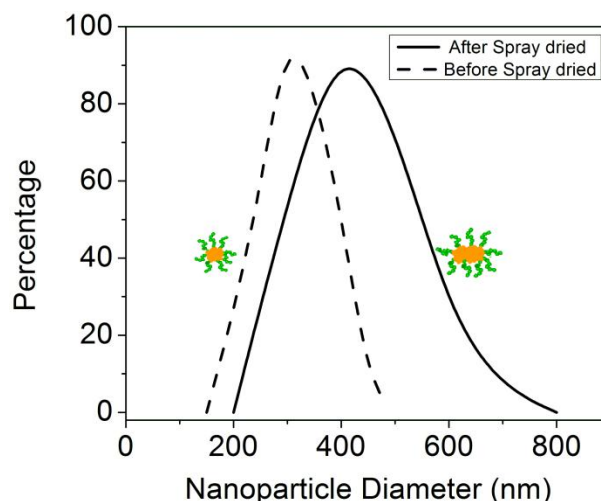


Figure 3-5. The size distribution of PEG-*b*-PCL (MW 5000-*b*-6000) nanoparticles encapsulating SR13668 before and after being spray dried. The drug-to-polymer weight ratio was 1:5. The inlet temperature of the spray dryer was 75 °C. 60% ethanol was added to the inlet stream.

3.4 Conclusions

Polymeric nanoparticles have shown attractive potentials for many biomedical and biological applications. It is important to elucidate the fundamental thermodynamics and kinetics to guide the production of the particles in a repeatable and scalable manner. Making polymeric nanoparticles encapsulating organic, hydrophobic drugs is a complicated process, which involves mixing, nucleation, growth, aggregation, micellization, and fluid dynamic. We have developed a continuous process to generate stable polymeric particles encapsulating the hydrophobic cancer-preventive compound, SR13668, with high DLR. The procedure can be used for encapsulating other hydrophobic compounds with minimal modifications based on the solubility and precipitation kinetics of the drug. It was demonstrated that instantaneous mixing ensures the higher drug loading. With the same composition, traditional

nanoprecipitation could never reach the same drug loading as achieved by flash nanoprecipitation.

The downstream processing of freeze drying and spray drying were also studied. Reproduction of the PEG-*b*-PCL-SR13668 nanoparticles depends on the type and amount of the excipients. Among leucine, sucrose, and trehalose, trehalose at concentration 50 times the nanoparticle concentration produced the smallest nanosuspension after both freeze drying and spray drying. The growth kinetics of the PLGA–SR13668 complex is mainly dominated by PLGA, which significantly decreases the particle growth rate of pure SR13668. At a SR13668 to PLGA ratio lower than 1:2, the size of the nanoparticles could be below 200nm before completely quenching particle growth by spray drying. The optimized spray drying parameters were found on the basis of the type and amount of excipients and the inlet temperatures-trehalose and leucine at concentrations 300 and five times of the nanoparticles and 75 °C inlet temperatures. Spray drying compared to freeze drying presented more advantages. The spray dryer was integrated with the MIVM, which reduced the preparation steps (such as dialysis) and therefore reduced the chance for particles to grow. More important, the continuous process is scalable. Kilograms of nanoparticles were easily generated for large animal tests, which will be reported in the next chapter.

CHAPTER 4. ENHANCED ORAL BIOAVAILABILITY OF A CANCER PREVENTIVE AGENT (SR13668) BY EMPLOYING POLYMERIC NANOPARTICLES WITH HIGH DRUG LOADING

4.1 Introduction

In this chapter, a candidate cancer preventive agent, 2,10-dicarbethoxy-6-methoxy-5,7-dihydro-indolo-(2,3-b)carbazole (SR13668), was encapsulated in PLGA nanoparticles at high DLR and high EE by employing FNP to enhance its oral bioavailability. SR13668 is developed from a natural anti-cancer agent indole-3-carbinol (I3C), which was found in cruciferous vegetables, such as broccoli, cauliflower and cabbage, and had promising anti-cancer activity both *in vitro* and *in vivo* models.¹¹⁴ SR13668 was developed based on the molecular structure of the four active oligomeric products of I3C by using Computer-Aided Rational Drug Design.^{115,116} SR13668 has been proved to act via I3C-like anti-cancer mechanisms which work through the modulation of PI3K/Akt pathway, but SR13668 possessed improved potency and activity compared to the original four I3C oligomers.¹¹⁶ Its anti-cancer activity was demonstrated in several *in vitro* and *in vivo* models of cancer, including breast, lung, prostate, and ovary cancers.^{117,118} It also shows negative results in the genotoxicity battery, and low toxicity in subchronic rat and dog studies.^{115,116,119} In the application of preventive agents, only non-invasive routes of administration (such as oral administration) are acceptable. However, SR13668 showed a very poor oral bioavailability due to its limited aqueous solubility and permeability. Initial attempts of studying the *in vivo* pharmacokinetic profiles of SR13668 show that the maximum oral bioavailability was <1% (compared to intravenous injection of the compound) in whole blood of rats as well as dogs.¹²⁰ Based on the *in vitro* measurements of aqueous solubility, caco-2 permeability, pKa value, and subsequent prediction of human intestinal absorption (Cloe[®] Predict Human Intestinal Absorption), low absorption of SR13668 in human gastrointestinal (GI) tracts

(<2mg) is expected.¹¹⁵ The low bioavailability causes not only a reduction in efficacy of the compound but also impracticality and inefficiency for *in vivo* applications. Chemical modification of the SR13668 molecule to increase its solubility (such as PEGylation) is difficult because the end groups of the molecule are not active for reactions. The strategy for increasing oral bioavailability of SR13668 is to develop a drug-delivery system, which can enhance SR13668 aqueous solubility and meanwhile remain its high permeability through biological membranes.

Two lipid surfactant-based SR13668 formulations, Solutol[®] and Labrasol[®], have been used to increase the compound oral bioavailability.^{115,120} However, one disadvantage of using surfactant-based formulations for sustained drug delivery is that they may not be as stable as polymeric nanoparticles upon large dilution in the blood stream. Also, side effects including emesis were observed when SR13668 was orally dosed in dogs using the surfactant stabilizers.¹¹⁵

Unlike other traditional processes in which DLR depends on the thermodynamic equilibrium of the system, FNP enables rapid mixing to create high supersaturation and therefore rapid nucleation and growth of the drug. Previously, we have developed and characterized a MIVM^{78,81} to facilitate the process of FNP. Particle growth kinetics at various drug-to-polymer ratios has been studied to optimize the size and DLR of the particles. In addition, to increase the long-term stability of nanoparticles by avoiding Ostwald ripening and particle collision and to adjust the concentration of the particles conveniently, nanoparticle suspensions were spray dried to be powder format. By integrating the MIVM with the spray drier, a continuous and scalable process has been achieved to generate and purify a large amount of nanoparticles. Methods to re-disperse the nanoparticles are studied and reported. The nanoparticles were dosed to mice and dogs for *in vivo* studies. The bioavailability of SR13668 in plasma and whole blood were tested by using MS/ high-

performance liquid chromatography (HPLC). A complete pharmacokinetic study was performed using the SR13668-PLGA nanoparticle formulations in eight beagle dogs (Figure 4-1). Pharmacokinetic parameters were analyzed following a single dose treatment and subsequent measurements of SR13668 levels in plasma and whole blood.

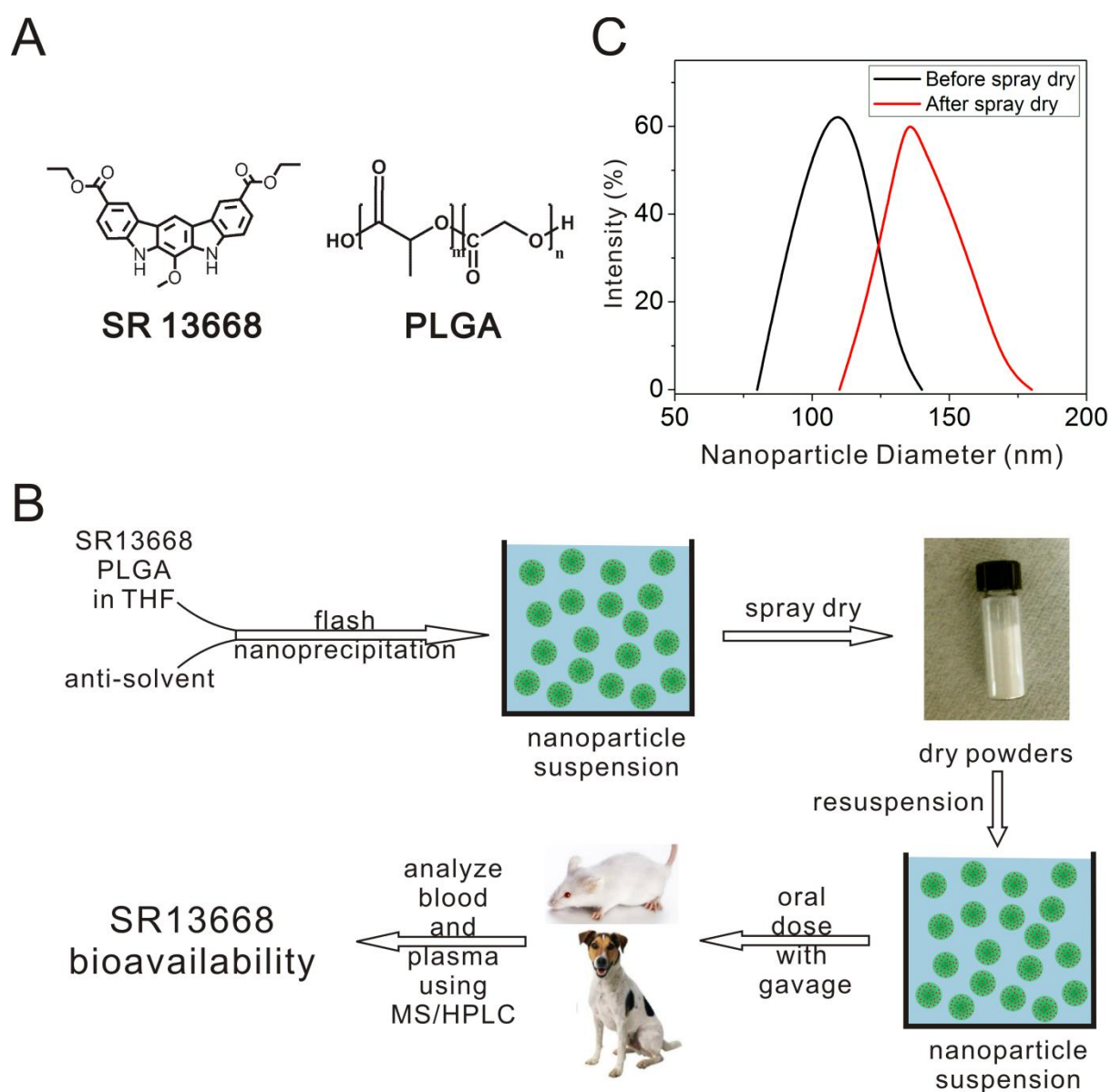


Figure 4-1. (A) Molecular structure of SR13668 and PLGA. (B) Flow chart of experiments. (C) Size distributions of SR13668-PLGA nanoparticle formulations before and after spray dry.

4.2 Experimental

4.2.1 Materials

PLGA (acid terminated, molecular weight (MW) 7000–17,000), THF, DMSO, ethanol, acetonitrile (HPLC grade), ammonium formate, leucine, sucrose, and trehalose were purchased from Sigma–Aldrich (St Louis, MO, USA). MTBE (HPLC grade) was purchased from Fisher Scientific (Pittsburgh, PA, USA). SR13668 was provided by National Cancer Institute (NCI) (Germantown, MD, USA). Labrasol® was purchased from Gattefossé USA (Paramus, NJ, USA). Unless otherwise stated, all chemicals were purchased at standard grades and used as received.

4.2.2 Nanoparticle preparation and size characterization

PLGA nanoparticles encapsulating SR13668 were generated by using the MIVM. The detailed procedures were described in chapter 3. Nanoparticle size distributions were measured by dynamic light scattering (DLS) (Zetasizer Nano ZS90; Malvern, Worcestershire, UK). The particle sizes were reported as the intensity-weighted radius. DLR of SR13668 in PLGA–SR13668 nanoparticles was quantified by ultraviolet–visible (UV–vis) spectroscopic measurements at the absorbance wavelength of 310 nm, after the sequential processes of dialysis, filtration through a 0.45 mm polyethersulfone filter, freeze drying for 3 days, and being re-dissolved in DMSO at solid concentration of 2 mg/mL. The extinction coefficient of SR13668 at 310 nm is $8.8 \times 10^4 \text{ M}^{-1} \text{ cm}^{-1}$.

4.2.3 Spray drying of the nanoparticle suspensions

Spray drying of the nanoparticle suspensions was carried out by integrating the MIVM with a spray dryer (SD-05 Spray Dryer; LabPlant, North Yorkshire, UK). The detailed procedures were described in chapter 3. In brief, to prevent the nanoparticles from aggregating, excipients such as trehalose, and leucine were added to the nanoparticle suspensions during the spray-drying process. 60% (v/v) ethanol was added to lower the inlet

temperature of the spray dryer. The inlet temperature was set to be 75 °C. The feed rate of the solutions was 10mL/min. Spray-dried powders were collected in a glass container at the outlet of the spray dryer.

Nanoparticles were resuspended into sterile Millipore water at SR13668 concentration 0.75mg/mL at vigorous stirring for 10min before dosing animals.

4.2.4 *In vitro* release of SR13668 from PLGA–SR13668 nanoparticle suspensions

The spray-dried PLGA–SR13668 nanoparticles were re-suspended in 0.1M phosphate buffered saline (PBS) at pH 2, 5, and 7.4 at the concentration of 1mg/mL, followed by the addition of MTBE at 4:1 ratio. The solutions were prepared following the sink condition that was previously described¹²¹ to ensure that the measurements of SR13668 release kinetics is not limited by its solubility in PBS buffer. Release of SR13668 from the particles was measured at 20 °C. Five hundred microliter of samples was taken from the extractive solution (MTBE phase) at designed time points (0, 0.5, 1, 2, 4, 6, 24, 48, and 72h) and 500 µL fresh MTBE were added back to the nanosuspensions every time to keep the constant volume.

SR13668 was measured using a liquid chromatography-mass spectrometry (LC-MS) [6430 Triple Quad LC/MS equipped with an ultra HPLC (Agilent 1290 Infinity Binary Pump and Autosampler); Agilent, Santa Clara, CA, USA]. SR13668 was monitored at m/z 429.0 → 414.0 with a collision energy setting of 20. Samples were prepared for injection by transferring a 300 µL aliquot from each time point into the appropriate well of a 2 mL 96-well polypropylene plate. The aliquoted samples were dried down under a heated stream of nitrogen (set at 35 °C) using a Zannetek analytical evaporator (ZipVap 96; Glas-Col, Terra Haute, IN, USA). After drying completely the samples were reconstituted with 100 µL of acetonitrile and mixed well using a Microplate Genie (USA Scientific, Ocala, FL, USA). Samples were then placed into the appropriate autosampler tray position for injection of 20 µL sample and subsequent analysis.

Standard curve samples were analyzed on each day of analysis and injected throughout the injection sequence. Standards were prepared by adding the appropriate volume from a 200 µg/mL stock solution of SR13668 (in DMSO) to MTBE. Standard concentrations used were 37.5, 75, 150, 300, 600, and 1200 ng/mL. Calibrators were processed for analysis following the procedure described above.

The chromatographic column was a Thermo Scientific Aquasil C18, 5 µ, 100× 2.1mm². The column temperature was maintained at 25 °C, and a flow rate of 0.50 mL/min was used. The MP consisted of 50mM ammonium formate pH 6.5 (MP A) and 100% acetonitrile (MP B). The MP gradient was as follows: after injection, initial conditions with MP B at 50% were held for 0.10min, decreased to 5% and held constant for 2.5 min, returning to 50% at 2.51 min for an additional 1.5 min to allow for re-equilibration. The total run time was about 5 min. The limit of quantitation was 37.5 ng/mL.

4.2.5 *In vivo* release and systemic levels of SR13668 in mice

The protocol for the mice study was approved by the UIC Animal Care Committee before initiation. Three groups of CD-1 mice (Charles River Breeding Laboratories, Portage, MI, USA) were used at a weight range of 25–35 g (n = 3/group). Animals were identified by a facility unique (eartag) number and were housed in an Association for Assessment and Accreditation of Laboratory Animal Care International International-accredited facility in microisolator polycarbonate cages with Anderson bed-o’cobs[®] bedding (Heinold, Kankakee, IL, USA) in a temperature (64–79 °F) and humidity (30%–70%) controlled room with a 14 h light/10 h dark cycle. Teklad Certified Rodent Chow No. 7012C (Harlan Inc., Madison, WI, USA), pellet form and autoclaved tap water in water bottles were provided *ad libitum* from arrival until termination. All animals were quarantined for at least 1 week before the initiation of dosing.

The PLGA particle suspensions encapsulating SR13668 (nano and microsize particles) were prepared by re-suspending dried powder in sterile water and vortexing for 10min at high speed. PEG400–Labrasol[®]-based formulation was prepared by mixing PEG400 and Labrasol[®] at 1:1 volume ratio followed by vigorous stirring for about 30min. The appropriate amount of the SR13668 was weighed and added to 75% of required total volume of above PEG400–Labrasol[®], followed by 120 min of stirring and then 5 min of sonication. Then, the remaining 25% volume of PEG400–Labrasol[®] was added to the mixture and stirred for 15min. The final PEG400–Labrasol[®] formulation was stored at 2–8 °C until dosing of the animals.

The mice were dosed via oral gavage at 5.5mg/kg dose of SR13668 based on most recent body weight. Blood samples were subsequently withdrawn at three time points per animal via orbital sinus. Three groups of mice were dosed with PLGA–SR13668 nanoparticles, PEG400–Labrasol[®] formulation of SR13668, and microsize PLGA–SR13668 particles, respectively. SR13668 concentrations from both plasma and whole blood samples were determined using LC–MS method described above.

4.2.6 Dog dosing and clinical observations

Nanoparticle powders were re-suspended in sterile water before dosing the animals. It was vortexed for 10 min at high speed to ensure complete re-suspension of the nanoparticles. For the control group, SR13668 was weighed out and the appropriate amount of 0.5% methylcellulose was added. This was stirred for mixing followed by homogenization to ensure a proper suspension. As a comparison, SR13668 in Labrasol[®] was also prepared based on the protocol published by Kapetanovic.¹¹⁵

The same four male and four female dogs were used for both test articles and control treatments after a suitable washout period of over two weeks. The SR13668-PLGA nanoparticles were dosed at 2.8 mg/kg of SR13668 on day one followed by blood sample

withdrawals. After a washout period of two weeks, the same animals were re-dosed with the SR13668 in 0.5% methylcellulose followed by sampling as before. A single dose of the formulation was administered by gavage to each animal at 10 mL/kg based on the most recent body weight of the animals.

Clinical signs were recorded one to two hours post dosing and once on the non-dosing days (24 hr sampling). Additionally, all animals were observed for moribundity/mortality twice daily whereas body weights were recorded prior to dosing for the dose calculation.

4.2.7 *In vivo* release and systemic levels of SR13668 in dog

Blood samples were collected at 0 (pre-dose), 0.5, 1.0, 1.5, 2.0, 4.0, 6.0, 8.0, 12.0 and 24.0 hr post dosing in EDTA containing tubes which were then stored on wet ice. Whole blood was withdrawn from these tubes and aliquoted into separate tubes on wet ice. The remaining blood samples in the collection tubes were centrifuged at approximately 3000 rpm for 15 min at 4°C to separate plasma. Plasma samples were aliquoted into separate vials and placed on dry ice. Both blood and plasma were stored at approximately -80°C until analysis.

Plasma samples were analyzed by a validated analytical method. Levels of SR13668 in plasma and blood were measured using a tandem mass spectrometer (Agilent 6430 Triple Quad LC/MS) equipped with an ultra HPLC (Agilent 1290 Infinity Binary Pump and Autosampler). Plasma extraction was performed using a salting-out assisted liquid-liquid extraction (SALLE) technique. This method of extraction was optimized by vortexing the samples vigorously for 5 minutes. For extraction of SR13668 from plasma, 25 µL of 5M ammonium acetate was added to 50 µL of the sample and mixed for approximately 1 minute. Acetonitrile (200 µL) was added to each sample and mixed vigorously for 5 minutes. The above mixture was then centrifuged at 3500 rpm for 10 minutes at 4°C in order to achieve adequate separation. Samples were then placed into the appropriate positions of the autosampler tray for 20 µL injection and subsequent analysis.

SR13668 was extracted from whole blood using a protein precipitation method that was preceded by lysing the red blood cells first. To extract SR13668 from whole blood, 50 μ L 70/30 (v/v) methanol:water was added to 50 μ L of the blood sample and mixed well for 10 minutes. Acetonitrile (200 μ L) was then added and mixed vigorously for 5 minutes. The mixture was then centrifuged at 3500 rpm for 10 minutes at 4°C in order to achieve adequate separation and finally placed in the autosampler tray for sample injection and subsequent analysis.

Standards and relevant quality controls (QCs) were analyzed with the samples on each day of the measurements. Standards and QCs were prepared by adding appropriate volume of a stock solution (30 μ g/mL SR13668 in DMSO) into blank dog/monkey blood or plasma. Standard concentrations used were 1.1, 4.5, 18, 45, 150, 375, 750 and 1,500 ng/mL. QC samples were prepared at 4.2, 117, and 1050 ng/mL. Calibrators and QC samples were analyzed following the procedure described above. The limit of quantitation (LOQ) was 1.1 ng/mL for dog plasma and blood.

The chromatographic column used is a Thermo Scientific Aquasil C18, 5 μ , 100 x 2.1 mm. The column temperature was maintained at 25°C, and a flow rate of 0.50 mL/min was used. The mobile phase (MP) consisted of 50 mM ammonium formate pH 6.5 (MP A) and 100% acetonitrile (MP B). The mobile phase gradient was as follows: after injection, initial conditions with MP B at 50% were held for 0.10 min, decreased to 5% and held constant for 2.5 min, returned to 50% at 2.51 min for an additional 1.5 min in order to allow for re-equilibration. The total run time was about 5 min.

4.2.8 Pharmacokinetic evaluation

Concentrations of SR13668 in plasma and whole blood were determined in all collected samples. The data were imported into WinNonlin pharmacokinetic analysis software (Phoenix® WinNonlin, version 6.1, Pharsight Corporation, Mountain View, CA).

Pharmacokinetic parameters were determined by a non-compartmental analysis. The area under the plasma concentration-time curve from time zero to 24 hours (AUC 0-24) was calculated by a linear-up log-down trapezoidal fit. Other pharmacokinetic parameters such as maximum plasma concentration (C_{max}), the time to achieve C_{max} (T_{max}), total body clearance for extravascular administration (CL/F calculated as $Dose/AUC_{INF}$) as well as the half-life ($t_{1/2}$) were also determined by WinNonlin. Subsequently, gender-based mean and standard deviation (SD) were calculated using Excel.

4.3 Results and discussion

4.3.1 Particle fabrication and resuspension

We have used a strategy to use polymeric nanoparticles to encapsulate the hydrophobic chemopreventive agent, SR13668, by employing FNP in the MIVM. FNP has demonstrated many advantages over TNP and emulsification in preparation of various polymeric nanoparticles encapsulating hydrophobic compounds, in terms of scalability, simplicity, and reproducibility.^{78,101} In this process, SR13668 and PLGA were dissolved in THF and precipitated by an antisolvent, during which copolymers aggregate and organic-drug compounds nucleate and grow. We have previously demonstrated the particle size distribution as a function of mixing time.^{101,102} More specifically, fast mixing is essential to achieve high DL of 33.3% as reported in next section. In addition, the scalable feature of FNP enables generation of hundreds of grams of nanoparticles in our laboratory for large animal tests, which could be difficult to prepare by other lab-scale processes.

To maintain the long-term stability of the nanoparticles and to conveniently generate suspensions at various nanoparticle concentrations, spray drying, as the post process after the particles were made, has been applied and optimized. Excipients such as sucrose, trehalose, and leucine were used as “spacers” to prevent permanent aggregation.

4.3.2 *In vitro* release

A phase-separated MTBE–PBS (0.1M) system was setup to monitor the *in vitro* release of SR13668 from the PLGA–SR13668 nanoparticles at pH 2, 5, and 7.4 and at 20 °C, as shown in Figure 4-2. SR13668 released in aqueous phase were thermodynamically extracted into the organic phase. Therefore, the measurements were not limited by the extreme low water solubility of the compounds. The release profile at all three pH conditions were very similar, which indicates that the release kinetics was controlled by diffusion instead of polymer degradation. This is consistent with a previous study.¹²² A burst release was observed in the first half an hour, during which about 20% of SR13668 was released from the PLGA–SR13668 nanoparticles. After that, the PLGA–SR13668 nanoparticles showed sustained release of SR13668. After 72 h, about 85% of the drug was released from the PLGA–SR13668 nanoparticles.

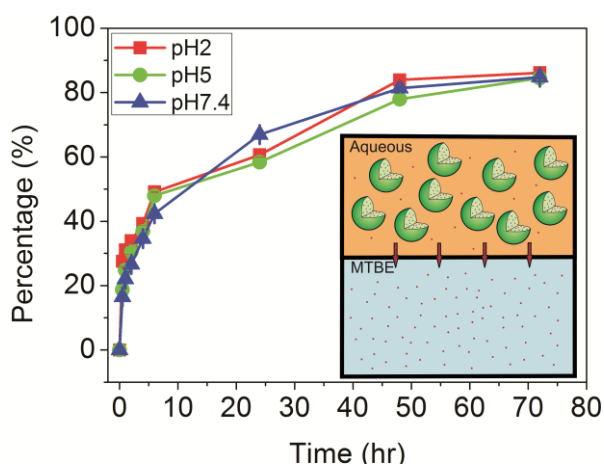


Figure 4-2. *In vitro* release of SR13668 from the PLGA nanoparticles in MTBE-aqueous two phase system.

4.3.3 Pharmacokinetics and bioavailability study in mice

Pharmacokinetics and *in vivo* availability of SR13668 were measured in mice whole blood and plasma after oral administration of different formulations. Oral drug delivery presents more biological barriers before a pharmaceutical molecule reaches the blood circulation:⁶² (1) gastrointestinal (GI) track has wide pH span—from extremely acidic conditions of the stomach (pH 2.5–3.5) to neutral or slightly basic conditions of the small intestine (pH 7–7.4); (2) the enzymes along the lumen of the intestine could degrade the potential pharmaceutical molecules; (3) the tenacious, viscous, elastic, and adhesive mucus layer coating the intestinal epithelium is hard to pass through by diffusion; and (4) the epithelium itself is another barrier to prevent molecules to enter the blood circulation.^{62,123,124} PLGA nanoparticles are promising carriers for oral drug delivery because they have been shown to prevent the degradation of pharmaceutical molecule in the stomach and lumen of the intestine,^{62,125} and also promote mucus penetration and epithelial cell endocytosis by optimization of their size and surface properties. The size of the nanoparticles plays a key role in penetrating the mucus layer and epithelial cells. Nanoparticles between 50 and 200nm show the best cell uptake in general,¹²⁶ because they exhibit efficient interfacial interaction with the cell membrane.^{123,124} In addition to the size of nanoparticles, the nanoparticle surface properties, including surface charges, targeting ligands, and hydrophilicity/hydrophobicity, also affect the GI uptake.^{127,128} The tests on mice demonstrated a significant increase of SR13668 both in whole blood and in plasma upon use of the smaller PLGA–SR13668 nanoparticles, as shown in Figure 4-3. Compared with the Labrasol[®] formulation, the peak concentration of SR13668 was increased more than seven times in whole blood and about three times in plasma by employing nanoparticles with average diameter of 150 nm. In order for nanoparticles to enhance the systemic availability of the hydrophobic SR13668, PLGA–SR13668 particle size has to be well controlled and high DLR has to be achieved. As a

comparison, micron-size PLGA–SR13668 particles presented no help in increasing the oral bioavailability.

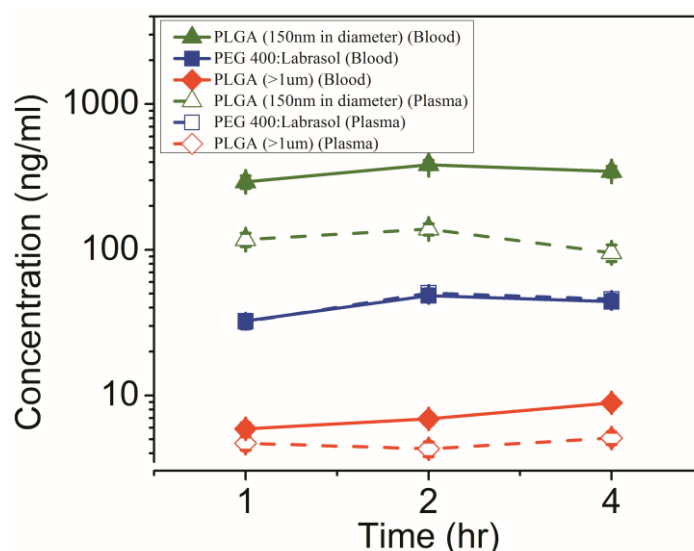


Figure 4-3. Concentration of SR13668 in mice whole blood and plasma after oral administration of the formulations.

4.3.4 Pharmacokinetics and bioavailability study in beagle dogs

There was no mortality observed during the study. Emesis of minor volume was noticed in all animals between 2 and 6 hours of dosing for both sexes. The animals did not show any other discomfort or adverse clinical signs during the study.

The drug levels in dog plasma and whole blood were shown in Figure 4-4. With the SR13668-PLGA nanoparticles, the mean group peak in plasma occurred at 4 hr in both males (29.6 ± 16.8 ng/mL, $n = 4$) and females (27.9 ± 6.8 ng/mL, $n = 4$). In whole blood, the mean group peak occurred at 4 hr in males (51.7 ± 24.6 ng/mL, $n = 4$) and at 6 hr in females (61.9 ± 36.1 ng/mL, $n = 4$). The animals dosed orally with 2.8 mg/kg SR13668 suspended in 0.5%

methylcellulose showed all levels below quantitation limit (BQL =1.1. ng/ml) in both plasma and whole blood. The pharmacokinetic parameters are presented in Table 4-1 and 4-2. Following a single gavage administration of the nanoparticle formulations, measurable amounts were seen in plasma in all males and two females up to 24 hr and in three males and three females in whole blood up to 24 hr. No sample was obtained at 8 and 12 hr in one female. SR13668-PLGA nanoparticle formulation appeared to have a moderate half-life in dogs, with calculated mean $t_{1/2}$ values of 4.4 hr in males and 6.7 hr in females in plasma and 4.9 hr in males and 4.3 hr in females in whole blood. The mean AUC_{0-24} was 371.0 ng-hr/mL and 240.4 ng-hr/mL in male and female plasma respectively and 590.0 ng-hr/mL and 533.0 ng-hr/mL in male and female whole blood respectively. The AUC was also extrapolated to infinity (AUC_{0-inf}) as shown in Table 4-1 and 4-2, using the terminal phase of the plasma concentration profile where appropriate.

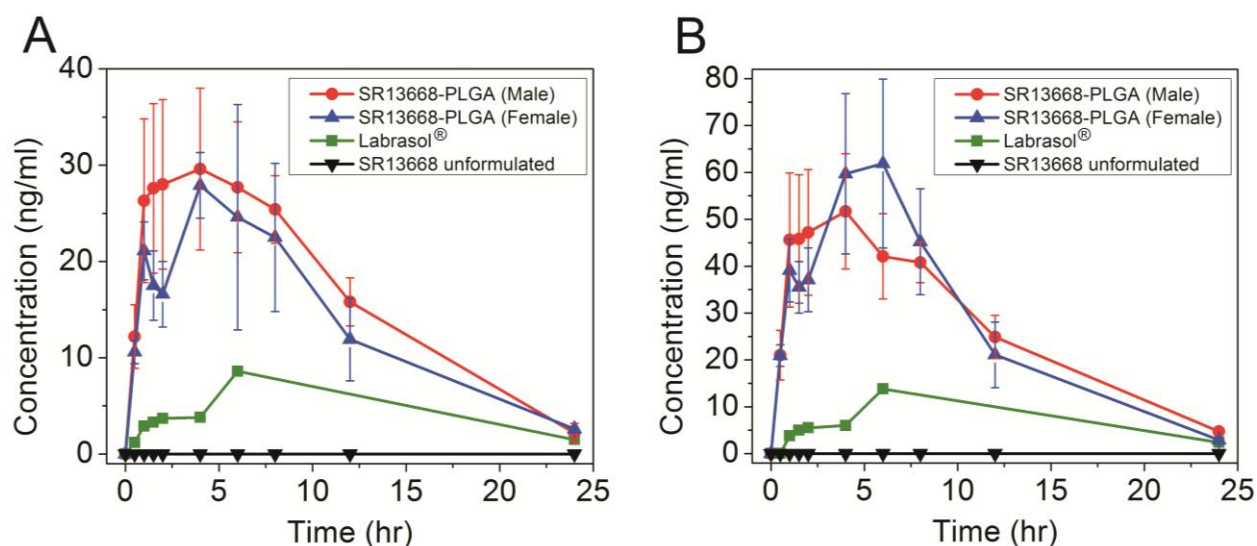


Figure 4-4. Mean drug levels in dog (A) plasma and (B) blood. Dogs were dosed at drug level of 2.8 mg/kg.

Table 4-1. Summary of pharmacokinetic parameters in dog plasma (mean \pm standard deviation)

Group	Sex	AUC _{0-inf} (ng*hr/mL)	AUC ₀₋₂₄ (ng*hr/mL)	C _{max} (ng/mL)	t _{1/2} (hr)	CL/F (mL/hr/kg)
1: 2.8 mg/kg	Male	385.5 \pm 155.5	371.0 \pm 148.4	34.2 \pm 13.0	4.4 \pm 0.4	8427.4 \pm 3961.5
	Female	315.5 \pm 95.1	240.4 \pm 129.2	37.1 \pm 14.6	6.7 \pm 0.4	9295.2 \pm 2800.0

Table 4-2. Summary of pharmacokinetic parameters in dog whole blood (mean \pm standard deviation)

Group	Sex	AUC _{0-inf} (ng*hr/mL)	AUC ₀₋₂₄ (ng*hr/mL)	C _{max} (ng/mL)	t _{1/2} (hr)	CL/F (mL/hr/kg)
1: 2.8 mg/kg	Male	733.6 \pm 162.1	590.0 \pm 253.6	58.2 \pm 19.5	4.9 \pm 0.1	3964.2 \pm 1000.1
	Female	690.9 \pm 89.6	533.0 \pm 287.9	76.2 \pm 36.6	4.3 \pm 1.1	4102.4 \pm 573.1

All the re-suspended particles are in the range of 100-200 nm, which is essential for targeting and sustained drug delivery. Although the smaller particles (<50nm) can pass through the biological barriers easier, but they may go to renal filtration quickly; while the big ones (>500 nm) will have slow transport through GI track to blood stream. For cancer chemotherapy, particles of 100-200 nm were aimed for passive targeting delivery to the tumor sites due to the enhanced-permeability-and-retention (EPR) effect. Moreover, particles below 450 nm can all go through sterile filtration.

Several initial pharmacokinetic studies were designed to assess the optimal batch of material. A low dose of the nanoparticle formulations at a 0.4 mg/kg in a dog showed C_{max} (11.3 ng/mL) at 1 hr with the level gradually decreasing by 4 hr. Conversely, the neat drug (SR13668 in 0.5 % methylcellulose) at a 0.75 mg/kg dose was BQL at all time points. This result indicated that at lower dose, the nanoparticle formulation was much better absorbed compared to the neat drug (unreported pilot data).

At a higher dose to the dogs (2.8 mg/kg), the drug levels in dog plasma and whole blood using the nanoparticles were found to be approximately two times higher than those using Labrasol[®]. The C_{max} and AUCs obtained in dogs using polymeric nanoparticles were several orders higher compared to the neat drug suspended in methylcellulose. These results are consistent with our previous studies in mice, despite the difference between the species. There are two reasons that the nanoparticles help to enhance SR13668 oral bioavailability: (1) high surface-to-volume ratio of the nanoparticles dramatically increase the aqueous solubility of the hydrophobic drug; and (2) the negatively charged PLGA due to the carboxyl end group assists the nanoparticles to adhere to and cross through the mucus layer. To verify the effect of surface charges, we have partially and completely capped the particle with polyethylene glycol (PEG), which is a neutral polymer and can prevent non-specific protein absorption. PEGylation, in this case, adversely affected drug oral availability (data not reported). The hypothesis is that although PEG helps to prolong nanoparticle blood circulation time, it reduces the residence time of the particles in GI track and therefore absorption of the particles and the drug by GI track.

Drug levels observed in whole blood were about 49-59% higher compared to that in plasma, indicating affinity of the test compound towards cellular uptake. C_{max} obtained in the beagle dogs was similar for both sexes in plasma, while in whole blood it was slightly increased in females. Calculated t_{1/2} values, however, were similar in male and female dogs in

whole blood, while females showed higher values in plasma. AUC_{0-24} was similar for both sexes in whole blood but was moderately lower in female plasma. Systemic clearance was calculated to be higher from plasma as compared to whole blood. Clearance seemed slightly faster in females from both plasma and whole blood. Overall, drug absorption following the oral dose administration was fairly rapid and there was a good systemic exposure.

4.4 Conclusions

We have used a continuous and scalable process to generate stable polymeric particles encapsulating the hydrophobic cancer-preventive compound, SR13668, with high DLR of 33.3%. PLGA was used to encapsulate SR13668 because of its similar precipitation kinetics compared with SR13668 and its property of mucoadhesion. At a SR13668 to PLGA ratio lower than 1:2, the size of the nanoparticles could be below 200nm before completely quenching particle growth by spray drying.

PLGA–SR13668 nanoparticles significantly enhanced the oral bioavailability of SR13668 in mice. Compared with the Labrasol[®] formulation, the peak concentration of SR13668 was increased more than seven times in whole blood and about three times in plasma by using PLGA–SR13668 nanoparticles.

Our study is one of the first attempts intended at using polymeric nanoparticle formulations to increase the solubility of a compound for bioavailability enhancement in large animals. Some work has been previously reported using oral administration of pH-dependent microspheres (larger particles) in monkeys to obtain intestinal delivery of the compound or the use of nano-spheres and nano-capsules to attain oral delivery of peptides while protecting them from protease degradation in monkeys and dogs,^{129,130} but no reports were found regarding the use of nanoparticles for increasing solubility of a compound to achieve greater bioavailability in large animals. In spite of the increasing interest in the use of

nano-delivery systems, reviews regarding the use of nanoparticle formulations in drug delivery mainly focus on small animals with the aim for targeted delivery.^{131,132}

Low oral bioavailability and fast clearance of SR13668 as well as other hydrophobic drugs have prevented the drugs from wide applications. With further optimization and tests, the polymeric nanoparticles encapsulating the hydrophobic SR13668 may present a new alternative to reach high drug systemic levels when orally administrated. Although formulation of SR13668 in a self-emulsifying drug delivery system (SEDDS) improved drug solubility and bioavailability, administration of a 38 mg dose (1/50th of the rat NOAEL) required an ingestion of 8 capsules per adult, which could adversely affect compliance with repeated or prolonged administration for a chemopreventive agent, particularly if substantially higher dosing is needed to achieve a pharmacologic response.

Furthermore, the process we have developed to generate stable nanoparticles is continuous and scalable. The amount of material required to tests on eight beagle dogs (~100 grams) can be produced in a few hours. Reproducibility and scalability of the process are essential for clinical applications of nanomedicines.¹³³

CHAPTER 5. ORALLY ADMINISTERED NANO-CURCUMIN TO ATTENUATE MORPHINE TOLERANCE AND DEPENDENCE: COMPARISON BETWEEN NEGATIVELY CHARGED AND PEGYLATED NANOPARTICLES

5.1 Introduction

Opioids, such as morphine, are widely used in the clinical management of acute and chronic pains.¹³⁴⁻¹³⁶ Drug tolerance (a decreased effect of a drug with repeated administration) and dependence (inability to stop using a drug even with strong desire to do so) are two of the major issues associated with opioids, which greatly limit their clinical applications.¹³⁷

Curcuma longa is a yellow-colored traditional herb which has been used for thousands of years in Asia for food flavoring, preservation, coloring material, as well as medicinal use. Curcumin [1,7-bis-(4-hydroxy-3-methoxyphenyl)-1,6-heptadiene-3,5-dione] is the active constituent of *Curcuma longa*.¹³⁸ It was recently found to have a wide spectrum of pharmacological activities, including antioxidant, cancer chemopreventive, anti-inflammatory, neuro-protective and antinociceptive actions.^{138,139} In recent years, a preliminary report suggested that chronic dose of large amount of curcumin (100 mg/kg) might attenuate morphine tolerance.¹⁴⁰ This opens a new window for curcumin be potentially used to alleviate morphine tolerance in patients with chronic pain and on long-term opioid therapy. However, the applications of curcumin has been hindered by its poor aqueous solubility, relatively low bioavailability, high rate of metabolism and rapid elimination and clearance from the body.¹³⁹ Although curcumin has been shown to be safe in many animal and human studies even at relatively high dosages, recent studies indicate that some of the effects (such as inhibition of proteasomal function and potentiation of huntingtin toxicity) of high dose curcumin are clearly toxic and undesirable beyond its use in cancer therapy.^{141,142}

Biphasic effect of curcumin on morphine tolerance and body weight loss on mice study were also observed.¹⁴³

In this chapter, similar process was applied and optimized to produce polymeric nanoparticles encapsulating curcumin, which we call nano-curcumin. High drug loading of 47% was achieved in the formulations. Relatively low dose of nano-curcumin (<20 mg/kg) was orally administrated in mice following subcutaneous injections of morphine. Mice behavioral studies (tail-flick test, and hot-plate tests and naloxone-induced withdrawal jumps) were conducted to demonstrate the effects of nano-curcumin on attenuating morphine tolerance and dependence, as shown in Figure 5-1. Direct comparison was drawn between negatively charged PLGA nanoparticles with partially and completely PEGylated nanoparticles.

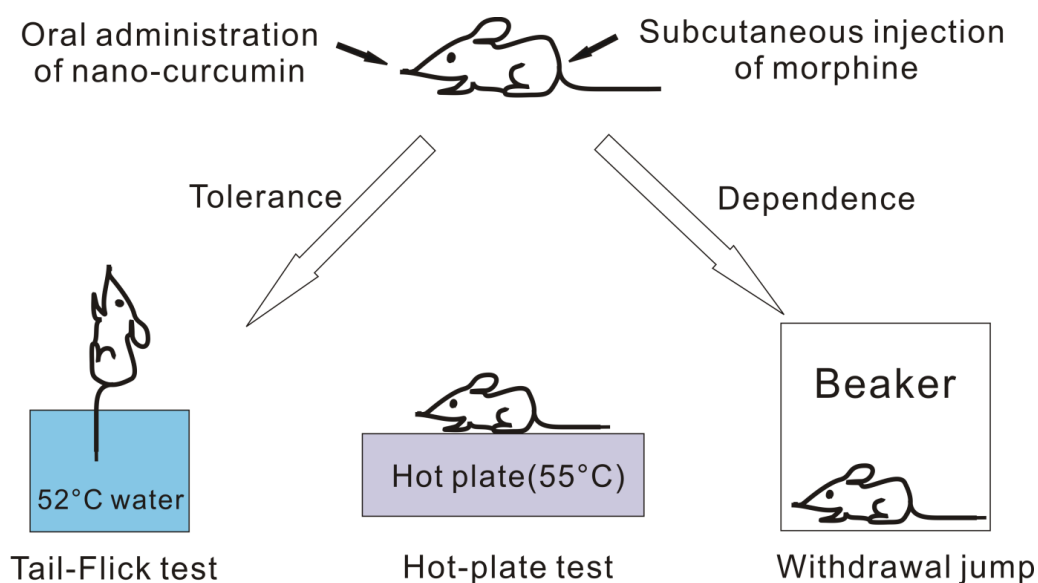


Figure 5-1. Mice behavioral studies, including tail-flick test, and hot-plate tests and naloxone-induced withdrawal jumps.

5.2 Experimental section

5.2.1 Materials

PLGA (acid terminated; PLA:PGA 50:50 w/w; Mw 7000-17000), curcumin, THF, DMSO, ethanol, leucine, trehalose and naloxone were purchased from Sigma-Aldrich (St Louis, MO). MTBE (HPLC grade) was purchased from Fisher Scientific (Pittsburgh, PA). Morphine was purchased from Hospira (Lake Forest, IL). Poly(ethylene glycol)-*b*-poly(lactic acid) (PEG-*b*-PLA) (MW 5000-*b*-6700) was purchased from Polymer Source (Dorval, Canada). Unless otherwise stated, all chemicals were purchased at standard grades and used as received.

5.2.2 Preparation and size characterization of nanoparticle suspensions

PLGA and PEG-*b*-PLA nanoparticles encapsulating curcumin were generated by using a MIVM. Among the four inlet streams, stream 1 was 0.2 wt% polymer and 0.2 wt% curcumin dissolved in THF. The other three inlet streams were Millipore water as an anti-solvent to precipitate the drug compound and polymers. The volumetric flow rate of streams 1 and 2 was 6 mL/min and it was 54 mL/min for streams 3 and 4.

Nanoparticle size distributions were measured by DLS (Malvern, Zetasizer Nano ZS90, Worcestershire, UK). The particle sizes were reported as the intensity-weighted radius. Viscosity and refractive index of the solvent were set to be 0.933 cP and 1.333, respectively.

The definition of DLR and EE were the same as previously reported.¹⁴⁴ Drug loading of curcumin in nanoparticles was quantified by UV-Vis spectrophotometer measurements at the absorbance wavelength of 435 nm, after the samples were spray dried and then redissolved in DMSO at a solid concentration of 2 mg/mL.

Zeta potentials of the formulations were measured by zeta sizer (Agilent, 7030 Nicomp DLS/ZLS-size and zeta, Santa Clara, CA) at 23 °C. Dielectric constant was 78.5.

5.2.3 Spray drying of the nanoparticle suspensions

Spray drying of the nanoparticle suspensions was carried out by integrating the MIVM with a spray dryer (LabPlant, SD-05 Spray Dryer, North Yorkshire, UK). We have previously optimized the spray-dry conditions for the nanoparticles to be re-suspended in aqueous solutions.¹⁴⁴ To prevent the nanoparticles from permanent agglomeration, trehalose (300:1 ratio to the nanoparticles) and leucine (5:1 ratio to the nanoparticles) were added to the nanoparticle suspensions as the excipients during the spray-dry process. Ethanol (60 v/v%) was added in order to lower the inlet temperature of the spray dryer, which was set as 75 °C, to compensate the relatively low melting temperature of the polymers. The feed rate of the solutions was 10 mL/min. Spray-dried powders were collected in a glass container at the outlet of the spray dryer.

Nanoparticles were resuspended into sterile Millipore water at vigorous stirring for 10 minutes before dosing animals.

5.2.4 Measurements of curcumin *in vitro* release from the nanoparticles

The spray dried PLGA, PEG-b-PLA, and hybrid nanoparticles were resuspended in 0.1 M PBS buffers at pH 2, pH5 and pH7.4 at the concentration of 10 mg/ml for the measurements of curcumin *in vitro* release. A two-phase system (Figure 5-3A) was designed to overcome the solubility limits of curcumin in aqueous solutions. MTBE was added to the aqueous buffers at 1:2 v/v ratio, which could extract the over saturated curcumin from the aqueous solutions. Solutions (500 µL) were taken from the organic MTBE phase at designed time points (0.5, 1, 2, 4, 6, 24 hours and 2, 3, 5, 7, 14, 21 days) and same amount (500 µL) fresh MTBE were added back to maintain the constant volume of the system. Curcumin in MTBE were quantified using fluorescence plate reader under excitation of 395nm and emission of 475nm, respectively.

5.2.5 Animals

Male ICR mice (20-25g, Charles River Laboratories, Wilmington, MA) were maintained on a 14/10h light/dark cycle with access to food and water ad libitum before experimental procedures. All experimental procedures were performed after approval by the Animal Care and Use Committee of the University of Illinois at Chicago and in accordance with the policies and recommendations of the National Institutes of Health guidelines for the handling and use of laboratory animals.

5.2.6 Tests for antinociception

Tail-Flick Test.

Basal nociception and morphine-induced antinociception were studied using the 52°C warm-water tail-flick test.^{145,146} In brief, mice were held over the water bath and one third of the distal portion of the tail was immersed into the water. The latency to a quick tail-flick response was recorded as a base-line measurement. Any mouse not responding within 5 sec was excluded from further experiment. To prevent tissue damage, a cut-off time of 12 sec was applied. Morphine-induced antinociception was evaluated 30 min after the injection of a testing dose of morphine (10mg/kg s.c.), and expressed as the percentage of maximal possible effect (%MPE) according to the following formula,¹⁴⁷

$$\%MPE = 100 \times (\text{postdrug latency} - \text{predrug latency}) / (\text{cut off} - \text{predrug latency})$$

Hot-Plate Test.

For assessment of response latencies to thermal stimulus in mice, a Cold/Hot Plate Analgesia Meter (Ugo Basile, Comerio, Italy) was used. In this study, mice were placed on a hot plate that was thermostatically maintained at 55 ± 1 °C. The nociceptive response was evaluated as the latency to the first licking or lifting of the rear paws or escape jumping. Mice were removed from the hot plate immediately after displaying the response and a cut-off time

of 30 sec was set to prevent tissue damage. The anti-nociceptive effect was measured using the same %MPE as above.

5.2.7 Acute opioid tolerance and dependence

To induce acute tolerance and dependence, separate groups of three ICR mice (20-25g) were treated with a large dose of morphine (100mg/kg s.c.). Maximal morphine tolerance and dependence peaked at approximately 4 to 6 h.^{145,148,149} Mice in the control group received an equal volume of saline. Tolerance to opioids was assessed 4.5h later by monitoring the antinociceptive effect produced by a test dose of morphine (10mg/kg, s.c.). The presence of opioid tolerance was signified by a significant reduction of antinociceptive effect. To examine dependence on opioids, mice were challenged with naloxone (10 mg/kg i.p.) 5h after the administration of morphine (100mg/kg s.c.). Mice were immediately placed inside glass cylinders, and naloxone-induced vertical jumps were recorded for 15min. To determine the effect of curcumin on preventing acute morphine tolerance and dependence, curcumin was given 15 min before the induction dose of morphine (100 mg/kg s.c.).

5.3 Results and discussion

5.3.1 Size distribution, drug loading, and encapsulation efficiency of the nanoparticles

Nanoparticle formulations have to meet several requirements to be possibly used for clinical applications – (1) all the materials are FDA approved; (2) the process has to be reproducible and scalable; (3) size distribution and surface properties of the nanoparticles have to be well characterized; (4) drug loading of the nanoparticles has to be high enough to contain sufficient active compound at a patient-compliance dose; and (5) high encapsulation rate for economic reasons. We have previously developed an integrated process of flash nanoprecipitation and freeze dry to satisfy above requirement. The reactor custom-designed for flash nanoprecipitation provides rapid micromixing to generate nanoparticles with narrow size distribution.⁷⁸ In our experiments, all the nanoparticles were generated at high Reynolds

number (> 9000) to ensure the homogeneous and flash precipitation.⁷⁸ PLGA, PEG-*b*-PLA and hybrid (PLGA to PEG-*b*-PLA 1:1 molar ratio) nanoparticles encapsulating curcumin were generated to compare the effect of surface properties on drug oral bioavailability and functionality. These polymers are chosen for the study because they are all degradable, biocompatible, and easy to synthesize. Moreover, PLGA and PLA have similar polymer structure with negative charges and PEG brushes were applied to partially or completely shield the surface charges. PEG can prevent non-specific protein absorption and prolong particle blood circulation time.

The average particle size (before and after spray dry), drug loading, encapsulation efficiency, and zeta potential of the nanoparticles with the three polymeric nanoparticle formulations are reported in Table 5-1. We consider the size of the particles after spray dry more important, since it represents the particles dosed to animals. After spray dry, the average diameters of all three re-suspended nanoparticles are similar (about 150 nm) with a trend of linearly reduced size when increasing the amount of PEG chains on the surface of the particles, but the difference is within 14% (or 21 nm). Highest drug loading and encapsulation efficiency were found in PEG-*b*-PLA particles among the three, but the difference is small compared to the PLGA nanoparticles with the lowest drug loading (< 3.5%). More than 90% of the drug encapsulation efficiency was found for all three formulations, and PEG-*b*-PLA nanoparticles presented the highest encapsulation rate. As we expected that with more PEG chains on the surface, zeta potential of the negatively charged PLGA (or PLA) nanoparticles became closer to be neutral.

Table 5-1. Average particle diameter (before and after spray dry), drug loading, encapsulation efficiency of the three curcumin nanoformulations.

Polymer	Diameter before spray dry (nm)	Diameter after spray dry(nm)	Drug loading (%)	Encapsulation efficiency (%)	Zeta potential (mV)
PLGA	79	165.8	46.2	92.4	-33.1±0.8
PLGA & PEG- <i>b</i> -PLA	—	159.9	47.1	94.2	-24.7±2.9
PEG- <i>b</i> -PLA	120	144.9	47.7	95.4	-2.5±1.8

Due to the relatively low glass transition temperature of the PLGA used (~60 °C), high inlet temperature of the spray drier induced active chain motion and resulted the permanent agglomeration of the particles. The size of PLGA-curcumin nanoparticles increased from 70 nm to about 165 nm (Figure 5-2A). Dimmers and trimmers were formed during the spray drying process. Also the size distribution after spray drying was boarder compared the size distribution before spray drying. Less agglomeration was observed for PEG-*b*-PLA-curcumin nanoparticles which may be due to the repulsion of PEG brushes (Figure 5-2A).

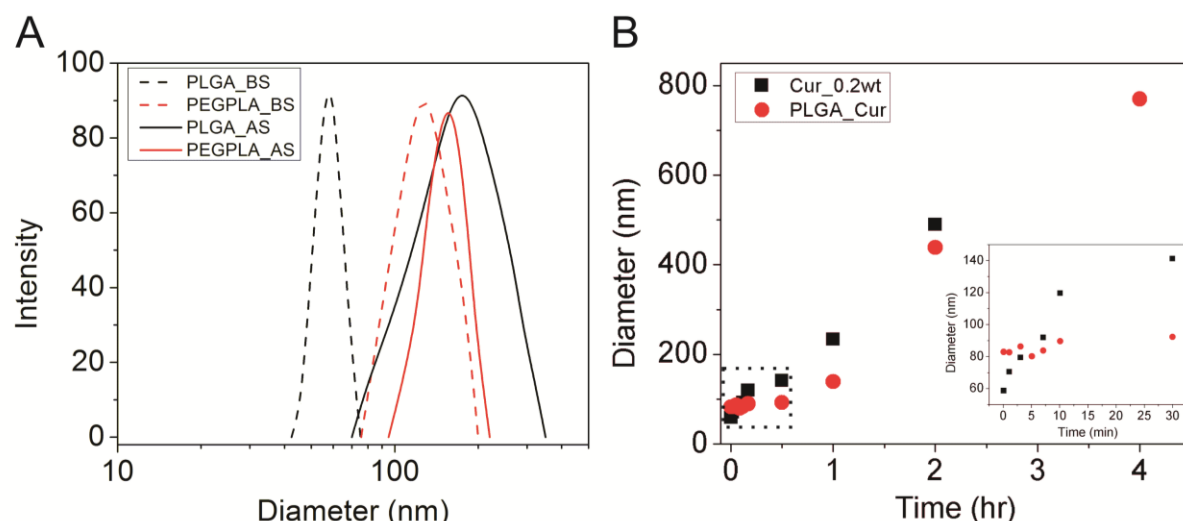


Figure 5-2. (A) Size distributions of PLGA curcumin and PEG-*b*-PLA curcumin nanoparticles before and after spray dry. Trehalose and leucine were added as excipients. Ethanol (60% v/v) was also added to the inlet stream. Dash lines: before spray dry. Solid lines: after spray dry. Black: PLGA curcumin nanoparticles. Red: PEG-*b*-PLA curcumin nanoparticles. (B) Growth kinetics of curcumin and PLGA curcumin (at 1:1 weight ratio). Size change in the first half hour (dash area) is separately plotted in the right corner. Black: curcumin alone; and red: PLGA curcumin (1:1 weight ratio).

The suspension of PEG-*b*-PLA nanoparticles is relatively stable, since the long PEG chains (Mw 5000) form brushes on the surface of the nanoparticles, which provide repulsion and energy barrier to prevent particle aggregation. Ostwald ripening based on the diffusive transport of curcumin, which is a slow process, takes most responsibility for the growth of the PEG-*b*-PLA nanoparticles. Stable suspension of PLGA nanoparticles relied on the charge repulsion, which is much weaker, to reduce particle collision and aggregation. Therefore, the relatively faster growth of the PLGA nanoparticles is our main concern.

The growth kinetics of curcumin alone and PLGA curcumin at 1:1 weight ratio were measured for up to 4 hours, as shown in Figure 5-2B. Growth of curcumin alone followed a linear fashion with a slope about 3.7 nm/min. The initial size of the nanoparticles was about 60 nm. However, after 30 minutes they grew to be 140 nm and after 2 hours about 500 nm. The PLGA-curcumin nanoparticles follow the growth kinetics of the polymer initially and then later curcumin growth kinetics. For the first 30 minutes, PLGA significantly reduced the growth. Eventually, more curcumin is exposed on the surface of the nanoparticles, and particle growth kinetics is dominated by the collision rate which is similar to that of the pure curcumin particles. To maintain the stability of the nanoparticles, flash nanoprecipitation was integrated with the spray dry, which eliminates growth media and produces dry-powder within 10 minutes.

5.3.2 *In vitro* release of curcumin

Slow release of curcumin from the nanoparticles was observed for up to 21 days. Release slightly depends on pH of the buffer solutions. At lower pH, PLGA and PLA degrades at faster rates. However, curcumin solubility reduces from 5.3 ng/mL at pH 7.4 to less than 1 ng/mL at pH 2, which hinder the transport and therefore the release of curcumin. The counter balanced effects of pH are reported in Figure 5-3B to 5-3D. Despite the faster release in the biological system with enzymes and cell uptake, based on the extremely slow *in vitro* release of curcumin from the nanoparticles, we hypothesize that curcumin were still encapsulated in the nanoparticles when it crossed the biological barriers from GI track to blood stream and then to central nerve system. The bioavailability of curcumin is mainly determined by the chemical and physical properties of the nanoparticles.

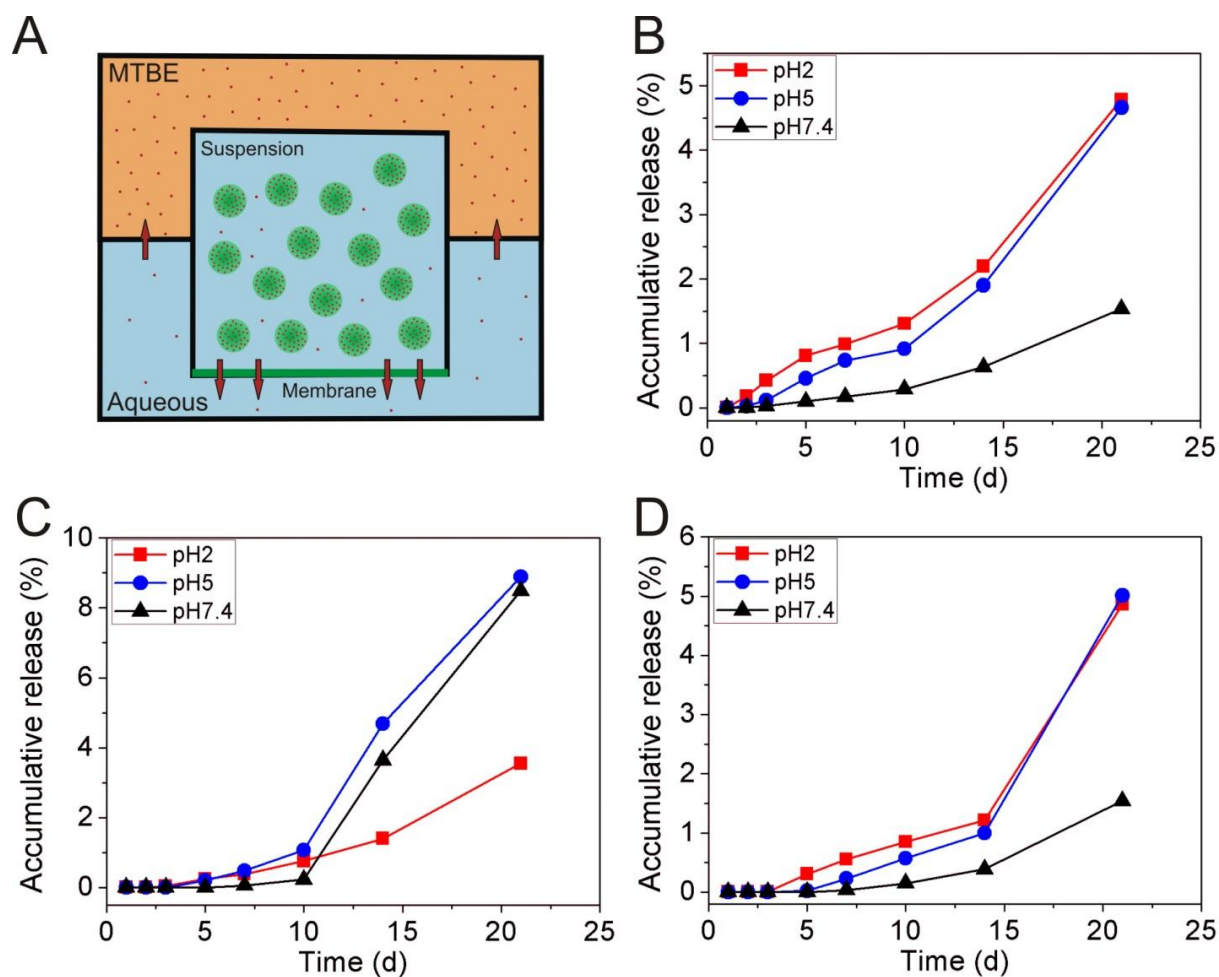


Figure 5-3. *In vitro* release of curcumin from nano-curcumin formulations in MTBE-aqueous two phase system. (A) Schematic drawing of the MTBE-aqueous two phase system. (B) PLGA-curcumin formulation. (C) PEG-PLA-curcumin formulation. (D) Hybrid-curcumin formulation.

5.3.3 Effects of curcumin and curcumin nanoparticles on attenuating morphine tolerance and dependence

An acute mouse model of opioid tolerance and dependence was used to test the effect of curcumin nanoformulations compared to unformulated free curcumin.^{145,148,149} Morphine tolerance was developed 2 to 6 hours after the administration of 100mg/kg morphine

subcutaneous.¹⁴⁹ The development of tolerance was evidenced by significant reduction of morphine antinociception after 4 hours (Figure 5-4, “MS group”). Tail-flick and hot-plate experiments were conducted 30 minutes after the subcutaneous administration of 10mg/kg morphine 4 hours later. Positive control group, dosed with saline initially and 10mg/kg morphine 4 hours later, exhibited significant antinociceptive effect, while the MS groups (as the negative control) showed significantly reduced of antinociception, indicative of the presence of opioid tolerance. All three nanoparticle suspensions of curcumin attenuated morphine tolerance in both tail-flick and hot-plate tests. PLGA-curcumin nanoformulation shows almost 100% analgesia in tail-flick experiment. Even the PEG-*b*-PLA nanoformulation, which showed the least effect, still had more than 50% analgesia. In hot-plate experiments, PLGA and hybrid (1:1 wt/wt ratio of PLGA and PEG-*b*-PCL) nanoparticles showed similar effects. Despite the superior physical and chemical properties of the PEG-*b*-PCL nanoparticle (in terms of particle size distribution, drug loading, and stability, presented in Table 5-1), PLGA-curcumin nanoparticles presented better efficacy. The main reason is that the negative charges of the PLGA facilitate the uptake and transport of the nanoparticles from GI track to blood stream and central nerve system. We have previously demonstrated the significantly enhanced oral bioavailability of hydrophobic drugs carried in PLGA nanoparticles and we expect PLGA-curcumin nanoparticles to be similar.¹⁴⁴

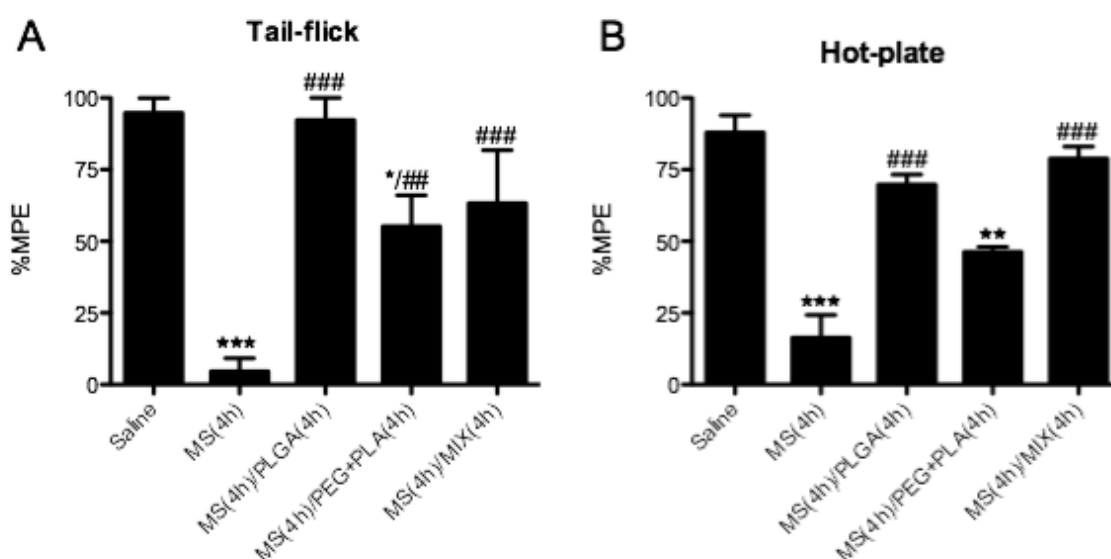


Figure 5-4. Effect of curcumin nanoformulations on morphine tolerance. (A) Tail-flick assay. (B) Hot plate assay. Groups of 3 mice received 500 μ L curcumin nanoformulation (20 mg/kg) or saline (MS and Saline group) orally. After 15 min, 100 mg/kg morphine or saline (Saline group) were dosed subcutaneously. Four hours later, 10 mg/kg were administrated subcutaneously to all the groups. Tail-flick assay and hot-plate assay were performed 30 minutes after that.

Unformulated free curcumin was also dosed to the mice to compare to the nano-curcumin. The results are as shown in Figure 5-5, which presented no analgesia effect at a dose of 20mg/kg compared to the positive control MS group. Low aqueous solubility and poor oral bioavailability take main responsibility for the low efficacy of free curcumin, which limits curcumin biomedical applications. Nanoformulations protect curcumin from the wide range of pH change in the gastrointestinal tract and the enzyme along the lumen of the intestine. Meanwhile the surface and size properties of nanoformulations facilitate the permeation

through biological membranes, which improve curcumin bioavailability and therefore its antinociceptive effect.

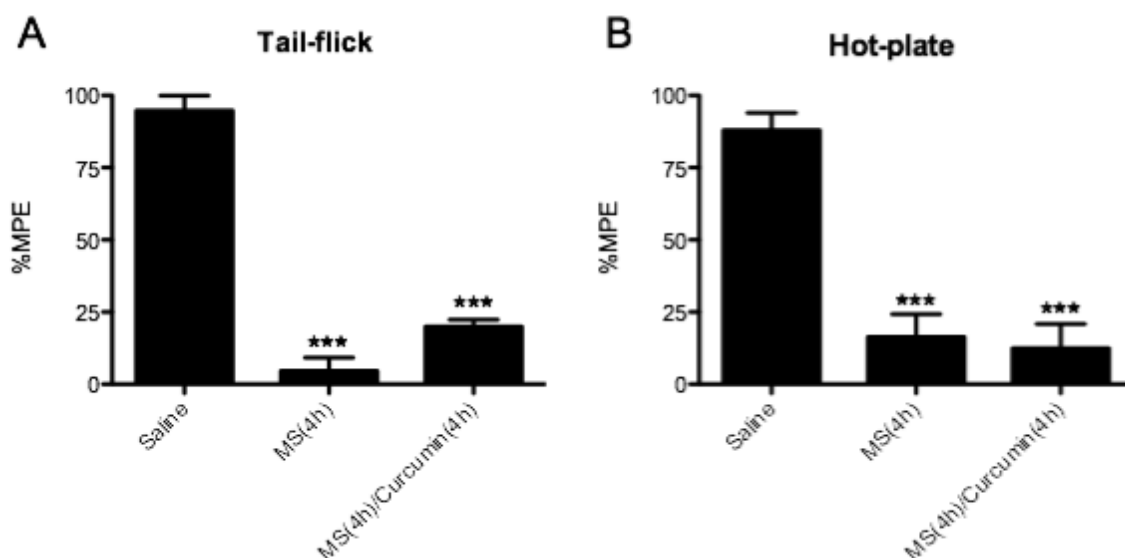


Figure 5-5. Effect of unformulated free curcumin on morphine tolerance. (A) Tail-flick assay. (B) Hot-plate assay. Groups of 3 mice received 500 μ L curcumin (20 mg/kg) or saline (MS and Saline group) orally. After 30 minutes, 100 mg/kg morphine or saline (Saline group) were dosed subcutaneous. 4 hours later, 10 mg/kg were administrated subcutaneous to all the groups. Tail-flick assay and hot-plate assay were performed 30 minutes after that.

Challenging the mice with opiate antagonist naloxone will precipitate withdrawal jumps, which is largely absent in saline control mice, as shown in Figure 5-6. Nano-curcumin was able to reduce the number of withdrawal jumps when comparing to the MS control group, especially the PLGA-curcumin nanoformulation. The mice treated with free curcumin showed no significant attenuation of withdrawal jumps when compared to the MS control group.

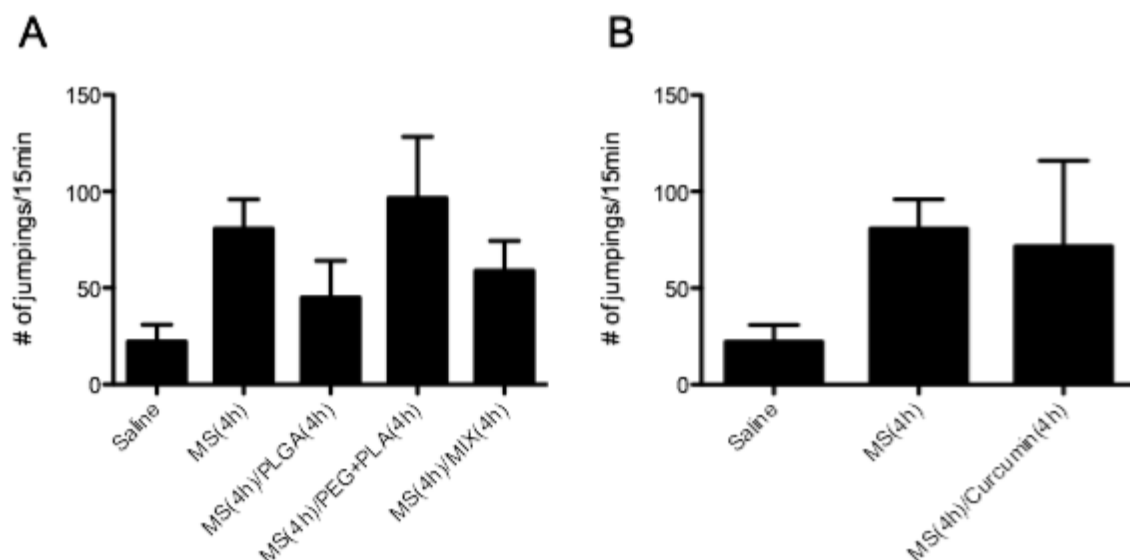


Figure 5-6. Effect of curcumin and curcumin nanoformulations on morphine dependence. Groups of 3 mice were challenged with naloxone (10mg/kg) intraperitoneally 5 hours after the administration of 100mg/kg morphine. The mice were immediately put inside glass cylinders and the number of escape jumps in 15 minutes was recorded.

5.4 Conclusion

We discovered and reported the effect of nano-curcumin on attenuating morphine tolerance and dependence. When nano-curcumin was orally administrated to mice at relatively low dose level following a large subcutaneous dose of morphine, significant analgesia was observed in both tail-flick and hot-plate experiments. In addition, reduced numbers of withdrawal jumps were observed with the similar dosing schedules of morphine and nano-curcumin. Among the three nanoparticle-curcumin formulations (PLGA-curcumin, PEG-b-PLA-curcumin, and hybrid of PLGA- and PEG-b-PCL-curcumin), PLGA-curcumin presented best efficacy. Although PEG chains help to prolong particle blood circulation time, PEGylated nanoparticles, when orally administrated, may be cleared from GI track quickly and have lower chance, compared to the negatively charged PLGA particles, to pass the

multiple biological barriers. At the same dose level, unformulated free curcumin showed minimum effect on morphine tolerance and dependence, because of the hydrophobic nature of the compound and its low bioavailability. Furthermore, it is essential to control the properties of the nanoparticles in order to improve hydrophobic compound oral bioavailability. The integrated process of flash nanoprecipitation and spray dry has been characterized in our previous studies to generate polymeric nanoparticles with high drug loading, narrow size distribution, well-designed surface charges, and long-term stability. The well-characterized and controlled nanoparticles provide the platform for drug delivery and drug discovery.

CHAPTER 6. CONCLUSIONS

In this thesis, we provide a perspective on the design, formation and characterization of polymeric nanoparticles for hydrophobic drug delivery. A continuous and scalable process was developed to generate stable polymeric nanoparticles encapsulating hydrophobic drugs with high drug loading and narrow size distribution. The potential applications were demonstrated by generating SR13668 and curcumin nanoformulations for cancer chemoprevention and pain management.

In Chapter 2, we demonstrated the fundamental mechanisms of self-assembly to produce nanoparticles using a MIVM. MIVM was able to provide rapid micromixing and high supersaturation values to produce nanoparticles with controlled size distribution and high drug loading rate. Dependence of nanoparticle sizes on Reynolds number, supersaturation value, nature of polymers, drug loading rate, and type of interaction forces was characterized. Regardless of the definition of Re , there existed a threshold value, over which nanoparticle sizes were independent of Re . Microscopic images showed the transition of mixing patterns in the MIVM with the increase of Re . At high Re over 1400, diffusion across the streamlines was fast enough and the diffusion length is comparable to the striation length, in which case with the exposure time of the microscope we could not differentiate the separate streamlines indicated by the red precipitation of $\text{Fe}(\text{SCN})_x^{(3-x)+}$. High Re homogenous mixing was essential to start the competitive kinetics simultaneously and uniformly, which contributes to the formation of nanoparticles with controlled size distribution and high DLR. The supersaturation level also played a key role in governing the size of nanoparticles encapsulating hydrophobic organic compounds in amphiphilic block copolymers. At higher supersaturation, with higher nucleation rate, more nucleation sites were generated and nanoparticles were smaller. It was showed that instantaneous mixing ensures the higher drug loading. With the same composition, traditional nanoprecipitation could never reach the same

drug loading as achieved by FNP. For a given drug compound, type of polymer, block length of the polymer, polymer to drug ratio, and presence of coprecipitator would all affect the size distribution and drug loading. The goal of the design is to match the competitive kinetics of polymer micellization and drug nucleation and growth.

In Chapter 3, we describe the downstream processing of freeze drying and spray drying that we have developed to maintain the long-term stability of the nanoparticles. The freeze dry and spray dry conditions were optimized in order to reproduce/resuspend PEG-*b*-PCL and PLGA nanoparticles. For PEG-*b*-PCL nanoparticles, trehalose at concentration 50 times the nanoparticle concentration efficiently prevents nanoparticle aggregation. Nanoparticles of similar sizes before and after both freeze drying and spray drying could be resuspended into aqueous solutions. For PLGA nanoparticles, the optimized spray drying conditions are trehalose and leucine (as the excipients) at concentrations 300 and five times of the nanoparticles respectively and 75 °C inlet temperatures of the spray dryer. Spray drying compared to freeze drying presented more advantages. The spray dryer was integrated with the MIVM, which made the process continuous and scalable. Meanwhile, it reduced the preparation steps (such as dialysis) and time and therefore reduced the chance for particles to grow.

In Chapter 4, a PLGA-SR13668 nanoparticles was generated based on the process developed in Chapter 2 and 3. The PLGA-SR13668 nanoparticles greatly increased the solubility of SR13668 in aqueous solutions and prevented SR13668 from fast clearance. PLGA was used to encapsulate SR13668 because of its similar precipitation kinetics compared with SR13668 and its property of mucoadhesion, which facilitated the nanoparticles to overcome gastrointestinal barriers. High drug loading of 33.3% was achieved. PLGA-SR13668 nanoparticles significantly enhanced the oral bioavailability of SR13668. Compared with the Labrasol[®] formulation, the peak concentration of SR13668 was increased

more than seven times in whole blood and about three times in plasma in beagle dogs by using PLGA–SR13668 nanoparticles. The C_{max} and AUCs obtained in dogs using polymeric nanoparticles were several orders higher compared to the neat drug suspended in methylcellulose. These results are consistent with our previous studies in mice, despite the difference between the species. Furthermore, we presented one of the first attempts intended at using polymeric nanoparticle formulations to increase the solubility of SR13668 for bioavailability enhancement in large animals.

In Chapter 5, we demonstrated our discovery that curcumin could attenuate morphine tolerance and dependence using the nanoparticle as the drug delivery platform. Three curcumin nanoformulations, PLGA, PEG-*b*-PLA and hybrid (PLGA to PEG-*b*-PLA 1:1 molar ratio) were generated with high drug loading (about 47%) and small particles with narrow size distribution. Significant analgesia was observed in both tail-flick and hot plate experiments by using all three formulations, while free curcumin at the same concentration showed minimal effect. PLGA curcumin nanoparticles presented the best efficacy, which may due to easier transport from GI track to blood stream and facilitated uptake of the particles for the negative charges of the surface. Similarly, curcumin nanoformulations were able to reduce the number of withdrawal jumps, especially the PLGA-curcumin nanoformulation, which indicates the attenuated morphine dependence. The mice treated with free curcumin showed no significant attenuation of withdrawal jumps when compared to the MS control group.

REFERENCES

1. Cho K, Wang X, Nie S, Chen Z, Shin DM 2008. Therapeutic nanoparticles for drug delivery in cancer. *Clin Cancer Res* 14(5):1310-1316.
2. Johnson BK, Prud'homme RK 2003. Flash NanoPrecipitation of organic actives and block copolymers using a confined impinging jets mixer. *Aust J Chem* 56(10):1021-1024.
3. Liong M, Lu J, Kovochich M, Xia T, Ruehm SG, Nel AE, Tamanoi F, Zink JJ 2008. Multifunctional inorganic nanoparticles for imaging, targeting, and drug delivery. *ACS Nano* 2(5):889-896.
4. Li S-D, Chen Y-C, Hackett MJ, Huang L 2008. Tumor-targeted delivery of siRNA by self-assembled nanoparticles. *Mol Ther* 16(1):163-169.
5. Ayame H, Morimoto N, Akiyoshi K 2008. Self-assembled cationic nanogels for intracellular protein delivery. *Bioconjugate Chem* 19(4):882-890.
6. Sun T-M, Du J-Z, Yan L-F, Mao H-Q, Wang J 2008. Self-assembled biodegradable micellar nanoparticles of amphiphilic and cationic block copolymer for siRNA delivery. *Biomaterials* 29(32):4348-4355.
7. Hainfeld JF, Slatkin DN, Focella TM, Smilowitz HM 2006. Gold nanoparticles: a new X-ray contrast agent. *Br J Radiol* 79(939):248-253.
8. Xie J, Zheng Y, Ying JY 2009. Protein-Directed Synthesis of Highly Fluorescent Gold Nanoclusters. *J Am Chem Soc* 131(3):888-+.
9. Huang XH, El-Sayed IH, Qian W, El-Sayed MA 2006. Cancer cell imaging and photothermal therapy in the near-infrared region by using gold nanorods. *J Am Chem Soc* 128(6):2115-2120.
10. Farokhzad OC, Langer R 2009. Impact of Nanotechnology on Drug Delivery. *Acs Nano* 3(1):16-20.
11. Allen TM, Cullis PR 2004. Drug delivery systems: Entering the mainstream. *Science* 303(5665):1818-1822.
12. Malmsten M 2006. Soft drug delivery systems. *Soft Matter* 2(9):760-769.
13. Gursoy RN, Benita S 2004. Self-emulsifying drug delivery systems (SEDDS) for improved oral delivery of lipophilic drugs. *Biomed Pharmacother* 58(3):173-182.
14. Cole ET, Cad D, Benameur H 2008. Challenges and opportunities in the encapsulation of liquid and semi-solid formulations into capsules for oral administration. *Adv Drug Delivery Rev* 60(6):747-756.
15. Straub JA, Chickering DE, Lovely JC, Zhang HM, Shah B, Waud WR, Bernstein H 2005. Intravenous hydrophobic drug delivery: A porous particle formulation of paclitaxel (AI-850). *Pharm Res* 22(3):347-355.
16. Spornath A, Aserin A 2006. Microemulsions as carriers for drugs and nutraceuticals. *Adv Colloid Interface Sci* 128:47-64.
17. Narang AS, Delmarre D, Gao D 2007. Stable drug encapsulation in micelles and microemulsions. *Int J Pharm* 345(1-2):9-25.
18. Mullertz A, Ogbonna A, Ren S, Rades T 2010. New perspectives on lipid and surfactant based drug delivery systems for oral delivery of poorly soluble drugs. *J Pharm Pharmacol* 62(11):1622-1636.
19. Griffin W 1949. Classification of surface-active agents by HLB. *J Soc Cosmet Chem* 1:311-326.
20. Griffin W 1954. Calculation of HLB Values of Non-Ionic Surfactants. *J Soc Cosmet Chem* 5:249-258.
21. Small DM 1968. A classification of biologic lipids based upon their interaction in aqueous systems. *J Am Oil Chem Soc* 45(3):108-119.

22. Pouton CW 2000. Lipid formulations for oral administration of drugs: non-emulsifying, self-emulsifying and 'self-microemulsifying' drug delivery systems. *Eur J Pharm Sci* 11:S93-S98.
23. Pouton CW 2006. Formulation of poorly water-soluble drugs for oral administration: Physicochemical and physiological issues and the lipid formulation classification system. *Eur J Pharm Sci* 29(3-4):278-287.
24. Small DM, Penkett SA, Chapman D 1969. Studies on simple and mixed bile salt micelles by nuclear magnetic resonance spectroscopy. *Biochim Biophys Acta* 176(1):178-189.
25. Pouton CW, Porter CJH 2008. Formulation of lipid-based delivery systems for oral administration: Materials, methods and strategies. *Adv Drug Delivery Rev* 60(6):625-637.
26. Constantinides PP 1995. Lipid microemulsions for improving drug dissolution and oral absorption-physical and biopharmaceutical aspects. *Pharm Res* 12(11):1561-1572.
27. Porter CJH, Pouton CW, Cuine JF, Charman WN 2008. Enhancing intestinal drug solubilisation using lipid-based delivery systems. *Adv Drug Delivery Rev* 60(6):673-691.
28. Kang BK, Lee JS, Chon SK, Jeong SY, Yuk SH, Khang G, Lee HB, Cho SH 2004. Development of self-microemulsifying drug delivery systems (SMEDDS) for oral bioavailability enhancement of simvastatin in beagle dogs. *Int J Pharm* 274(1-2):65-73.
29. Wu W, Wang Y, Que L 2006. Enhanced bioavailability of silymarin by self-microemulsifying drug delivery system. *Eur J Pharm Biopharm* 63(3):288-294.
30. Al-Jamal WT, Kostarelos K 2011. Liposomes: From a Clinically Established Drug Delivery System to a Nanoparticle Platform for Theranostic Nanomedicine. *Acc Chem Res* 44(10):1094-1104.
31. Drulis-Kawa Z, Dorotkiewicz-Jach A 2010. Liposomes as delivery systems for antibiotics. *Int J Pharm* 387(1-2):187-198.
32. Immordino ML, Dosio F, Cattel L 2006. Stealth liposomes: review of the basic science, rationale, and clinical applications, existing and potential. *Int J Nanomed* 1(3):297-315.
33. Woodle MC, Papahadjopoulos D 1989. Liposome preparation and size characterization. *Methods Enzymol* 171:193-217.
34. Bangham AD, Standish MM, Watkins JC 1965. Diffusion of univalent ions across the lamellae of swollen phospholipids. *J Mol Biol* 13(1):238-252.
35. Kragh-Hansen U, le Maire M, Moller JV 1998. The mechanism of detergent solubilization of liposomes and protein-containing membranes. *Biophys J* 75(6):2932-2946.
36. Paternostre MT, Roux M, Rigaud JL 1988. Mechanisms of membrane-protein insertion into liposomes during reconstitution procedures involving the use of detergents.1. solubilization of large unilamellar liposomes (prepared by reverse-phase evaporation) by triton X-100, octyl glucoside, and sodium cholate. *Biochemistry* 27(8):2668-2677.
37. Riaz M 1996. Liposomes preparation methods. *Pak J Pharm Sci* 9(1):65-77.
38. Deamer D, Bangham AD 1976. Large volume liposomes by an ether vaporization method. *Biochim Biophys Acta, Biomembr* 443(3):629-634.
39. Szoka F, Papahadjopoulos D 1978. Procedure for preparation of liposomes with large Internal aqueous space and high capture by reverse-phase evaporation. *Proc Natl Acad Sci U S A* 75(9):4194-4198.
40. Handa T, Takeuchi H, Ohokubo Y, Kawashima Y 1987. Lyophilized liposomes prepared by a modified reversed-phase evaporation method. *Chem Pharm Bull* 35(2):748-755.
41. Hamilton RL, Goerke J, Guo LSS, Williams MC, Havel RJ 1980. Unilamellar liposomes made with the French pressure cell-a simple preparative and semi-quantitative technique. *J Lipid Res* 21(8):981-992.

42. Ohsawa T, Miura H, Harada K 1985. Improvement of encapsulation efficiency of water-soluble drugs in liposomes formed by the freeze-thawing method. *Chem Pharm Bull* 33(9):3945-3952.
43. Boas U, Heegaard PMH 2004. Dendrimers in drug research. *Chem Soc Rev* 33(1):43-63.
44. Mintzer MA, Grinstaff MW 2011. Biomedical applications of dendrimers: a tutorial. *Chem Soc Rev* 40(1):173-190.
45. Svenson S 2009. Dendrimers as versatile platform in drug delivery applications. *Eur J Pharm Biopharm* 71(3):445-462.
46. Buhleier E, Wehner W, Vogtle F 1978. Cascade-chain-like and non-skid-chain-like syntheses of molecular cavity topologies. *Synthesis* (2):155-158.
47. Tomalia DA, Baker H, Dewald J, Hall M, Kallos G, Martin S, Roeck J, Ryder J, Smith P 1985. A new class of polymers - starburst-dendritic macromolecules. *Polym J (Tokyo, Jpn)* 17(1):117-132.
48. Hawker CJ, Frechet JMJ 1990. Preparation of polymers with controlled molecular architecture - a new convergent approach to dendritic macromolecules. *J Am Chem Soc* 112(21):7638-7647.
49. Rajamalli P, Prasad E 2012. Non-amphiphilic pyrene cored poly(aryl ether) dendron based gels: tunable morphology, unusual solvent effects on the emission and fluoride ion detection by the self-assembled superstructures. *Soft Matter* 8:8896-8903.
50. Newkome GR, Yao ZQ, Baker GR, Gupta VK 1985. Micelles. 1. Cascade molecules: a new approach to micelles - a [27]-arborol. *J Org Chem* 50(11):2003-2004.
51. Ihre H, Hult A, Soderlind E 1996. Synthesis, characterization, and H-1 NMR self-diffusion studies of dendritic aliphatic polyesters based on 2,2-bis(hydroxymethyl)propionic acid and 1,1,1-tris(hydroxyphenyl)ethane. *J Am Chem Soc* 118(27):6388-6395.
52. Lee CC, MacKay JA, Frechet JMJ, Szoka FC 2005. Designing dendrimers for biological applications. *Nat Biotechnol* 23(12):1517-1526.
53. Newkome GR, Yao ZQ, Baker GR, Gupta VK 1985. Micelles. 1. Cascade molecules - a new approach to micelles - A [27]-arborol. *J Org Chem* 50(11):2003-2004.
54. Bosman AW, Janssen HM, Meijer EW 1999. About dendrimers: Structure, physical properties, and applications. *Chem Rev* 99(7):1665-1688.
55. Jain K, Kesharwani P, Gupta U, Jain NK 2010. Dendrimer toxicity: Let's meet the challenge. *Int J Pharm* 394(1-2):122-142.
56. Pearson RM, Sunoqrot S, Hsu H-J, Bae JW, Hong S 2012. Dendritic nanoparticles: the next generation of nanocarriers? *Ther Delivery* 3(8):941-959.
57. Bae JW, Pearson RM, Patra N, Sunoqrot S, Vukovic L, Kral P, Hong S 2011. Dendron-mediated self-assembly of highly PEGylated block copolymers: a modular nanocarrier platform. *Chem Commun* 47(37):10302-10304.
58. Kedar U, Phutane P, Shidhaye S, Kadam V 2010. Advances in polymeric micelles for drug delivery and tumor targeting. *Nanomed Nanotech Biol Med* 6(6):714-729.
59. Kataoka K, Harada A, Nagasaki Y 2001. Block copolymer micelles for drug delivery: design, characterization and biological significance. *Adv Drug Delivery Rev* 47(1):113-131.
60. Shaw RW, Brill TB, Clifford AA, Eckert CA, Franck EU 1991. Supercritical water - a medium for chemistry. *Chem Eng News* 69(51):26-39.
61. Byrappa K, Ohara S, Adschiri T 2008. Nanoparticles synthesis using supercritical fluid technology - towards biomedical applications. *Adv Drug Delivery Rev* 60(3):299-327.
62. Yamanaka YJ, Leong KW 2008. Engineering strategies to enhance nanoparticle-mediated oral delivery. *J Biomater Sci, Polym Ed* 19(12):1549-1570.
63. Sun YP, Meziani ML, Pathak P, Qu LW 2005. Polymeric nanoparticles from rapid expansion of supercritical fluid solution. *Chem--Eur J* 11(5):1366-1373.

64. Yeo SD, Kiran E 2005. Formation of polymer particles with supercritical fluids: A review. *J Supercrit Fluids* 34(3):287-308.
65. York P 1999. Strategies for particle design using supercritical fluid technologies. *Pharm Sci Technol Today* 2(11):430-440.
66. Vauthier C, Bouchemal K 2009. Methods for the Preparation and Manufacture of Polymeric Nanoparticles. *Pharm Res* 26(5):1025-1058.
67. Ito F, Makino K 2004. Preparation and properties of monodispersed rifampicin-loaded poly(lactide-co-glycolide) microspheres. *Colloids Surf, B* 39(1-2):17-21.
68. Mainardes RM, Evangelista RC 2005. PLGA nanoparticles containing praziquantel: effect of formulation variables on size distribution. *Int J Pharm* 290(1-2):137-144.
69. QuintanarGuerrero D, Allemann E, Doelker E, Fessi H 1997. A mechanistic study of the formation of polymer nanoparticles by the emulsification-diffusion technique. *Colloid Polym Sci* 275(7):640-647.
70. Kumar V, Prud'Homme RK 2008. Thermodynamic Limits on Drug Loading in Nanoparticle Cores. *J Pharm Sci* 97(11):4904-4914.
71. Kim SY, Lee YM 2001. Taxol-loaded block copolymer nanospheres composed of methoxy poly(ethylene glycol) and poly(epsilon-caprolactone) as novel anticancer drug carriers. *Biomaterials* 22(13):1697-1704.
72. Allen C, Eisenberg A, Mrcic J, Maysinger D 2000. PCL-b-PEO micelles as a delivery vehicle for FK506: Assessment of a functional recovery of crushed peripheral nerve. *Drug Delivery* 7(3):139-145.
73. Fessi H, Puisieux F, Devissaguet JP, Ammoury N, Benita S 1989. Nanocapsule formation by interfacial polymer deposition following solvent displacement. *Int J Pharm* 55(1):R1-R4.
74. Schubert S, Delaney JT, Jr., Schubert US 2011. Nanoprecipitation and nanoformulation of polymers: from history to powerful possibilities beyond poly(lactic acid). *Soft Matter* 7(5):1581-1588.
75. Horn D, Rieger J 2001. Organic nanoparticles in the aqueous phase - theory, experiment, and use. *Angew Chem, Int Ed* 40(23):4331-4361.
76. Johnson BK, Prud'homme RK 2003. Chemical processing and micromixing in confined impinging jets. *AIChE J* 49(9):2264-2282.
77. Liu Y, Kathan K, Saad W, Prud'homme RK 2007. Ostwald ripening of beta-carotene nanoparticles. *Phys Rev Lett* 98(3):036102.
78. Liu Y, Cheng C, Prud'homme RK, Fox RO 2008. Mixing in a multi-inlet vortex mixer (MIVM) for flash nano-precipitation. *Chem Eng Sci* 63(11):2829-2842.
79. Hoang TKN, Deriemaeker L, La VB, Finsy R 2004. Monitoring the simultaneous Ostwald ripening and solubilization of emulsions. *Langmuir* 20(21):8966-8969.
80. Lifshitz I, Slyozov V 1961. The kinetics of precipitation from supersaturated solid solutions. *J Phys Chem Solids* 19(1-2):35-50.
81. Russ B, Liu Y, Prud'homme RK 2010. Optimized descriptive model for micromixing in a vortex mixer. *Chem Eng Commun* 197(8):1068-1075.
82. Cheng JC, Olsen MG, Fox RO 2009. A microscale multi-inlet vortex nanoprecipitation reactor: Turbulence measurement and simulation. *Appl Phys Lett* 94(20).
83. Tice JD, Song H, Lyon AD, Ismagilov RF 2003. Formation of droplets and mixing in multiphase microfluidics at low values of the Reynolds and the capillary numbers. *Langmuir* 19(22):9127-9133.
84. Lavasanifar A, Samuel J, Kwon GS 2001. Micelles self-assembled from poly(ethylene oxide)-block-poly(N-hexyl stearate L-aspartamide) by a solvent evaporation method: effect on the solubilization and haemolytic activity of amphotericin B. *J Controlled Release* 77(1-2):155-160.

85. Baleux B 1972. Colorimetric determination of silver of nonionic polyoxyethylene surface using iodo-iodated solution. *C R Seances Acad Sci, Ser C* 274(19):1617-1620.
86. Johnson BK. 2003. Flash nanoprecipitation of organic actives via confined micromixing and block copolymer stabilization. ed., Princeton: Princeton University.
87. Ugelstad J, Berge A, Ellingsen T, Schmid R, Nilsen TN, Mork PC, Stenstad P, Hornes E, Olsvik O 1992. Preparation and application of new monosized polymer particles. *Prog Polym Sci* 17(1):87-161.
88. Dirksen JA, Ring TA 1991. Fundamentals of Crystallization - Kinetic Effects on Particle-Size Distributions and Morphology. *Chem Eng Sci* 46(10):2389-2427.
89. Mao SR, Neu M, Germershaus O, Merkel O, Sitterberg J, Bakowsky U, Kissel T 2006. Influence of polyethylene glycol chain length on the physicochemical and biological properties of poly(ethylene imine)-graft-poly(ethylene glycol) block copolymer/SiRNA polyplexes. *Bioconjugate Chem* 17(5):1209-1218.
90. Kwon GS 2003. Polymeric micelles for delivery of poorly water-soluble compounds. *Crit Rev Ther Drug Carrier Syst* 20(5):357-403.
91. Lin WJ, Juang LW, Lin CC 2003. Stability and release performance of a series of pegylated copolymeric micelles. *Pharm Res* 20(4):668-673.
92. Photos PJ, Bacakova L, Discher B, Bates FS, Discher DE 2003. Polymer vesicles in vivo: correlations with PEG molecular weight. *J Controlled Release* 90(3):323-334.
93. Mosqueira VCF, Legrand P, Morgat JL, Vert M, Mysiakine E, Gref R, Devissaguet JP, Barratt G 2001. Biodistribution of long-circulating PEG-grafted nanocapsules in mice: Effects of PEG chain length and density. *Pharm Res* 18(10):1411-1419.
94. Monkenbusch M, Schneiders D, Richter D, Willner L, Leube W, Fetters LJ, Huang JS, Lin M 2000. Aggregation behaviour of PE-PEP copolymers and the winterization of diesel fuel. *Physica B: Condensed Matter* 276:941-943.
95. Mullin JW. 1993. Crystallization. 3rd ed., Oxford, UK: Butterworth Heinemann. p 176.
96. Liu Y, Kathan K, Saad W, Prud'homme RK 2007. Ostwald ripening of beta-carotene nanoparticles. *Phys Rev Lett* 98(3).
97. Geng Y, Discher DE 2005. Hydrolytic degradation of poly(ethylene oxide)-block-polycaprolactone worm micelles. *J Am Chem Soc* 127(37):12780-12781.
98. Shuai XT, Ai H, Nasongkla N, Kim S, Gao JM 2004. Micellar carriers based on block copolymers of poly(ϵ -caprolactone) and poly(ethylene glycol) for doxorubicin delivery. *J Controlled Release* 98(3):415-426.
99. Shuai XT, Merdan T, Schaper AK, Xi F, Kissel T 2004. Core-cross-linked polymeric micelles as paclitaxel carriers. *Bioconjugate Chem* 15(3):441-448.
100. Kumar V, Prud'homme RK 2009. Nanoparticle stability: Processing pathways for solvent removal. *Chem Eng Sci* 64(6):1358-1361.
101. Liu Y, Tong Z, Prud'homme RK 2008. Stabilized polymeric nanoparticles for controlled and efficient release of bifenthrin. *Pest Manage Sci* 64(8):808-812.
102. Shen H, Hong S, Prud'homme RK, Liu Y 2011. Self-assembling process of flash nanoprecipitation in a multi-inlet vortex mixer to produce drug-loaded polymeric nanoparticles. *J Nanopart Res* 13(9):4109-4120.
103. Zhang LF, Eisenberg A 1996. Multiple morphologies and characteristics of "crew-cut" micelle-like aggregates of polystyrene-*b*-poly(acrylic acid) diblock copolymers in aqueous solutions. *J Am Chem Soc* 118(13):3168-3181.
104. Mehnert W, Mader K 2001. Solid lipid nanoparticles - Production, characterization and applications. *Adv Drug Deliv Rev* 47(2-3):165-196.
105. Okuyama K, Abdullah M, Lenggono IW, Iskandar F 2006. Preparation of functional nanostructured particles by spray drying. *Adv Powder Technol* 17(6):587-611.

106. Sollohub K, Cal K 2010. Spray Drying Technique: II. Current Applications in Pharmaceutical Technology. *J Pharm Sci* 99(2):587-597.
107. Re MI 2006. Formulating drug delivery systems by spray drying. *Drying Technol* 24(4):433-446.
108. Gharsallaoui A, Roudaut G, Chambin O, Voilley A, Saurel R 2007. Applications of spray-drying in microencapsulation of food ingredients: An overview. *Food Res Int* 40(9):1107-1121.
109. Konan YN, Gurny R, Allemann E 2002. Preparation and characterization of sterile and freeze-dried sub-200 nm nanoparticles. *Int J Pharm* 233(1-2):239-252.
110. Lemoine D, Francois C, Kedzierewicz F, Preat W, Hoffman M, Maincent P 1996. Stability study of nanoparticles of poly(epsilon-caprolactone), poly(D,L-lactide) and poly(D,L-lactide-co-glycolide). *Biomaterials* 17(22):2191-2197.
111. Franks F, Hatley RHM, Mathias SF 1991. Materials science and the production of shelf-stable biologicals. *Biopharm-Technol Bus* 4(9):38.
112. Chang LQ, Shepherd D, Sun J, Ouellette D, Grant KL, Tang XL, Pikal MJ 2005. Mechanism of protein stabilization by sugars during freeze-drying and storage: Native structure preservation, specific interaction, and/or immobilization in a glassy matrix? *J Pharm Sci* 94(7):1427-1444.
113. Galmarini MV, Baeza R, Sanchez V, Zamora MC, Chirife J 2011. Comparison of the viscosity of trehalose and sucrose solutions at various temperatures: Effect of guar gum addition. *LWT--Food Sci Technol* 44(1):186-190.
114. Aggarwal BB, Ichikawa H 2005. Molecular targets and anticancer potential of indole-3-carbinol and its derivatives. *Cell Cycle* 4(9):1201-1215.
115. Kapetanovic IM, Muzzio M, Hu SC, Crowell JA, Rajewski RA, Haslam JL, Jong L, McCormick DL 2010. Pharmacokinetics and enhanced bioavailability of candidate cancer preventative agent, SR13668 in dogs and monkeys. *Cancer Chemother Pharmacol* 65(6):1109-1116.
116. Chao WR, Yean D, Amin K, Green C, Jong L 2007. Computer-aided rational drug design: A novel agent (SR13668) designed to mimic the unique anticancer mechanisms of dietary indole-3-carbinol to block akt signaling. *J Med Chem* 50(15):3412-3415.
117. Jong L, Chao W-R, Amin K, Laderoute K, Orduna J, Sato B, Rice G 2004. SR13668: A novel indole derived inhibitor of phospho-Akt potently suppresses tumor growth in various murine xenograft models. *AACR Meeting Abstracts* 2004(1):849-d-850.
118. Jong L, Chao W-R, Amin K, Yean D 2005. SR13668: An orally active inhibitor of phospho-Akt potently suppresses tumor growth and synergizes with chemotherapeutics both in vitro and in vivo. *AACR Meeting Abstracts* 2005(1):401-a.
119. Doppalapudi RS, Riccio ES, Rausch LL, Shimon JA, Lee PS, Mortelmans KE, Kapetanovic IM, Crowell JA, Mirsalis JC 2007. Evaluation of chemopreventive agents for genotoxic activity. *Mutat Res, Genet Toxicol Environ Mutagen* 629(2):148-160.
120. Green CE, Swezey R, Bakke J, Shinn W, Furimsky A, Bejugam N, Shankar GN, Jong L, Kapetanovic IM 2011. Improved oral bioavailability in rats of SR13668, a novel anti-cancer agent. *Cancer Chemother Pharmacol* 67(5):995-1006.
121. Gibaldi M, Feldman S 1967. Establishment of sink conditions in dissolution rate determinations. Theoretical considerations and application to nondisintegrating dosage forms. *J Pharm Sci* 56(10):1238-1242.
122. Zolnik BS, Leary PE, Burgess DJ 2006. Elevated temperature accelerated release testing of PLGA microspheres. *J Controlled Release* 112(3):293-300.
123. Qaddoumi MG, Ueda H, Yang J, Davda J, Labhasetwar V, Lee VHL 2004. The characteristics and mechanisms of uptake of PLGA nanoparticles in rabbit conjunctival epithelial cell layers. *Pharm Res* 21(4):641-648.

124. Desai MP, Labhasetwar V, Walter E, Levy RJ, Amidon GL 1997. The mechanism of uptake of biodegradable microparticles in Caco-2 cells is size dependent. *Pharm Res* 14(11):1568-1573.
125. Sakuma S, Hayashi M, Akashi M 2001. Design of nanoparticles composed of graft copolymers for oral peptide delivery. *Adv Drug Delivery Rev* 47(1):21-37.
126. Win KY, Feng SS 2005. Effects of particle size and surface coating on cellular uptake of polymeric nanoparticles for oral delivery of anticancer drugs. *Biomaterials* 26(15):2713-2722.
127. Behrens I, Pena AIV, Alonso MJ, Kissel T 2002. Comparative uptake studies of bioadhesive and non-bioadhesive nanoparticles in human intestinal cell lines and rats: The effect of mucus on particle adsorption and transport. *Pharm Res* 19(8):1185-1193.
128. Shakweh M, Besnard M, Nicolas V, Fattal E 2005. Poly (lactide-co-glycolide) particles of different physicochemical properties and their uptake by Peyer's patches in mice. *Eur J Pharm Biopharm* 61(1-2):1-13.
129. Allemann E, Leroux JC, Gurny R 1998. Polymeric nano- and microparticles for the oral delivery of peptides and peptidomimetics. *Adv Drug Delivery Rev* 34(2-3):171-189.
130. Leroux JC, Cozens RM, Roesel JL, Galli B, Doelker E, Gurny R 1996. pH-sensitive nanoparticles: An effective means to improve the oral delivery of HIV-1 protease inhibitors in dogs. *Pharm Res* 13(3):485-487.
131. Kesisoglou F, Panmai S, Wu Y 2007. Nanosizing - Oral formulation development and biopharmaceutical evaluation. *Adv Drug Delivery Rev* 59(7):631-644.
132. Surendiran A, Sandhiya S, Pradhan SC, Adithan C 2009. Novel applications of nanotechnology in medicine. *Indian J Med Res* 130(6):689-701.
133. Reid JM, Walden CA, Qin R, Ziegler KLA, Haslam JL, Rajewski RA, Warndahl R, Fitting CL, Boring D, Szabo E, Crowell J, Perloff M, Jong L, Bauer BA, Mandrekar SJ, Ames MM, Limburg PJ, Canc Prevention N 2011. Phase 0 Clinical Chemoprevention Trial of the Akt Inhibitor SR13668. *Cancer Prev Res* 4(3):347-353.
134. McQuay H 1999. Opioids in pain management. *Lancet* 353(9171):2229-2232.
135. Przewlocki R, Przewlocka B 2001. Opioids in chronic pain. *Eur J Pharmacol* 429(1-3):79-91.
136. Rowbotham MC, Twilling L, Davies PS, Reisner L, Taylor K, Mohr D 2003. Oral opioid therapy for chronic peripheral and central neuropathic pain. *N Engl J Med* 348(13):1223-1232.
137. Trujillo KA, Akil H 1991. Inhibition of morphine-tolerance and dependence by the NMDA receptor antagonist MK-801. *Science* 251(4989):85-87.
138. Sharma RA, Gescher AJ, Steward WP 2005. Curcumin: The story so far. *Eur J Cancer* 41(13):1955-1968.
139. Anand P, Kunnumakkara AB, Newman RA, Aggarwal BB 2007. Bioavailability of curcumin: Problems and promises. *Mol Pharmaceutics* 4(6):807-818.
140. Matsushita Y, Ueda H 2009. Curcumin blocks chronic morphine analgesic tolerance and brain-derived neurotrophic factor upregulation. *Neuroreport* 20(1):63-68.
141. Cole GM, Teter B, Frautschy SA. 2007. Neuroprotective effects of curcumin. ed. p 197-212.
142. Dikshit P, Goswami A, Mishra A, Nukina N, Jana NR 2006. Curcumin enhances the polyglutamine-expanded truncated N-terminal huntingtin-induced cell death by promoting proteasomal malfunction. *Biochem Biophys Res Commun* 342(4):1323-1328.
143. Lin J-A, Chen J-H, Lee Y-W, Lin C-S, Hsieh M-H, Chang C-C, Wong C-S, Chen JJ-Y, Yeh G-C, Lin F-Y, Chen T-L 2011. Biphasic Effect of Curcumin on Morphine Tolerance: A Preliminary Evidence from Cytokine/Chemokine Protein Array Analysis. *J Evidence-Based Complementary Altern Med*:1-11.

144. Shen H, Banerjee AA, Mlynarska P, Hautman M, Hong S, Kapetanovic IM, Lyubimov AV, Liu Y 2012. Enhanced oral bioavailability of a cancer preventive agent (SR13668) by employing polymeric nanoparticles with high drug loading. *J Pharm Sci* 101(10):3877-3885.
145. Tang L, Shukla PK, Wang LX, Wang ZJ 2006. Reversal of morphine antinociceptive tolerance and dependence by the acute supraspinal inhibition of Ca²⁺/calmodulin-dependent protein kinase II. *J Pharmacol Exp Ther* 317(2):901-909.
146. He Y, Yang C, Kirkmire CM, Wang ZJ 2010. Regulation of Opioid Tolerance by let-7 Family MicroRNA Targeting the mu Opioid Receptor. *J Neurosci* 30(30):10251-10258.
147. Wang ZJ, Gardell LR, Ossipov MH, Vanderah TW, Brennan MB, Hochgeschwender U, Hruby VJ, Malan TP, Lai J, Porreca F 2001. Pronociceptive actions of dynorphin maintain chronic neuropathic pain. *J Neurosci* 21(5):1779-1786.
148. Bilsky EJ, Bernstein RN, Wang ZJ, Sadee W, Porreca F 1996. Effects of naloxone and D-Phe-Cys-Tyr-D-Trp-Arg-Thr-Pen-Thr-NH₂ and the protein kinase inhibitors H7 and H8 on acute morphine dependence and antinociceptive tolerance in mice. *J Pharmacol Exp Ther* 277(1):484-490.
149. Tang L, Shukla PK, Wang ZJ 2007. Disruption of acute opioid dependence by antisense oligodeoxynucleotides targeting neurogranin. *Brain Res* 1143:78-82.
150. Bilsky EJ, Bernstein RN, Wang Z, Sadee W, Porreca F 1996. Effects of naloxone and D-Phe-Cys-Tyr-D-Trp-Arg-Thr-Pen-Thr-NH₂ and the protein kinase inhibitors H7 and H8 on acute morphine dependence and antinociceptive tolerance in mice. *J Pharmacol Exp Ther* 277(1):484-490.
151. Tang L, Shukla PK, Wang LX, Wang ZJ 2006. Reversal of Morphine Antinociceptive Tolerance and Dependence by the Acute Supraspinal Inhibition of Ca²⁺/Calmodulin-Dependent Protein Kinase II. *J Pharmacol Exp Ther* 317(2):901-909.
152. Tang L, Shukla PK, Wang ZJ 2007. Disruption of acute opioid dependence by antisense oligodeoxynucleotides targeting neurogranin. *Brain Res* 1143:78-82.

VITA

NAME: Hao Shen

EDUCATION:

B.S., Polymer Science and Engineering, South China University of Technology, Guangzhou, China, 2008

Ph.D., Chemical Engineering, University of Illinois at Chicago, Chicago, USA, 2013

PUBLICATIONS:

1. **Hao Shen**, Aryamitra A. Banerjee, Paulina Mlynarska, Mathew Hautman, Seungpyo Hong, Izet M. Kapetanovic, Alexander V. Lyubimov, and Ying Liu, Enhanced oral bioavailability of a cancer preventive agent (SR13668) by employing polymeric nanoparticles with high drug loading, *Journal of Pharmaceutical Sciences*, 101 (10) 3877-3885, 2012.
2. Vishal Sharma, Magdalena Szymusiak, **Hao Shen**, Ludwig C. Nitsche, and Ying Liu, Formation of Polymeric Toroidal-Spiral Particles, *Langmuir*, 28(1), 729–735, 2012.
3. **Hao Shen**, Seungpyo Hong, Robert K. Prud'homme, and Ying Liu, Self-assembling process of flash nanoprecipitation in a multi-inlet vortex mixer to produce drug-loaded polymeric nanoparticles, *Journal of Nanoparticle Research*, 13(9), 4109-4120, 2011.
4. Aryamitra A. Banerjee*, **Hao Shen***, Mathew Hautman, Jaseem Anwer, Seungpyo Hong, Izet M. Kapetanovic, Ying Liu, and Alexander V Lyubimov, Enhance oral bioavailability of the hydrophobic chemopreventive agent (SR13668) in beagle dogs, *Current Pharmaceutical Biotechnology*, 14, 2013. (*Equivalent first authors).
5. **Hao Shen**, Xiaoyu Hu, Zaijie Wang, Ying Liu, Orally administrated nano-curcumin to attenuate morphine tolerance and dependence: comparison between negatively charged and PEGylated Nanoparticles, *in preparation*.